Summer 1998

Development and realization of a single-mode optical fiber ferrule mold insert with twelve channels

Hsiharng William Yang
Louisiana Tech University

INFORMATION TO USERS

This manuscript has been reproduced from the microfilm master. UMI films the text directly from the original or copy submitted. Thus, some thesis and dissertation copies are in typewriter face, while others may be from any type of computer printer.

The quality of this reproduction is dependent upon the quality of the copy submitted. Broken or indistinct print, colored or poor quality illustrations and photographs, print bleedthrough, substandard margins, and improper alignment can adversely affect reproduction.

In the unlikely event that the author did not send UMI a complete manuscript and there are missing pages, these will be noted. Also, if unauthorized copyright material had to be removed, a note will indicate the deletion.

Oversize materials (e.g., maps, drawings, charts) are reproduced by sectioning the original, beginning at the upper left-hand corner and continuing from left to right in equal sections with small overlaps. Each original is also photographed in one exposure and is included in reduced form at the back of the book.

Photographs included in the original manuscript have been reproduced xerographically in this copy. Higher quality 6" x 9" black and white photographic prints are available for any photographs or illustrations appearing in this copy for an additional charge. Contact UMI directly to order.

UMI

A Bell & Howell Information Company
300 North Zeeb Road, Ann Arbor MI 48106-1346 USA
313/761-4700 800/521-0600

DEVELOPMENT AND REALIZATION OF A SINGLE-MODE OPTICAL FIBER FERRULE MOLD INSERT WITH TWELVE CHANNELS

by

Hsiharng William Yang, M.S.

A Dissertation Presented in Partial Fulfillment
of the Requirements for the Degree
Doctor of Engineering

College of Engineering and Science
LOUISIANA TECH UNIVERSITY

May, 1998

LOUISIANA TECH UNIVERSITY

THE GRADUATE SCHOOL

05 - 22 - 98
Date

We hereby recommend that the thesis prepared under our supervision by Hsiharng William Yang

entitled Development and Realization of A Single-Mode Optical Fiber Ferrule Mold Insert with Twelve Channels

be accepted in partial fulfillment of the requirements for the Degree of Doctor of Engineering

Supervisor of Thesis Research

Head of Department
Mechanical Engineering
Department

Recommendation concurred in:

Advisory Committee

Approved:
Director of Graduate Studies

Approved:
Director of the Graduate School

Dean of the College

GS Form 13
2/97

ABSTRACT

A manufacturing process for an optical fiber ferrule mold insert with twelve channels has been established. This research project presents mask design, mask fabrication, deep X-ray lithography exposure, resist developing, nickel electroforming, as well as surface finishing to attain the final result. Deep X-ray mask fabrication methods are explored, including mechanically machined masks, micro-EDM masks, and E-beam written masks. The exposures to pattern resists and electroforming to fabricate nickel molds up to 500 μm thickness are reported in this study. Nickel structures for the optical fiber ferrule insert with twelve channels made by electroforming are the final products. A practical method to finish the microstructure surface is presented. Channels with precision -0.0/+0.5 micron and pitch alignment with 0.25 micron are accomplished to satisfy the requirements of the research sponsor for inserting standard optical fibers (125 μm in diameter).

APPROVAL FOR SCHOLARLY DISSEMINATION

The author grants to the Prescott Memorial Library of Louisiana Tech University the right to reproduce, by appropriate methods, upon request, any or all portions of this Thesis. It is understood that "proper request" consists of the agreement, on the part of the requesting party, that said reproduction is for his personal use and that subsequent reproduction will not occur without written approval of the author of this Thesis. Further, any portions of the Thesis used in books, papers, and other works must be appropriately referenced to this Thesis.

Finally, the author of this Thesis reserves the right to publish freely, in the literature, at any time, any or all portions of this Thesis.

Author H. William Yang

Date 05-22-98

GS Form 14
2/97

TABLE OF CONTENTS

Page

LIST OF FIGURES

LIST OF TABLES

ACKNOWLEDGEMENTS

To complete this project, the following people for various contributions are acknowledged. I would like to thank Dr. Michael Vasile for his guidance, assistance, patience, and, most important of all, for his support in this project. His knowledge of microfabrication provided many suggestions needed to complete this effort. Sincere appreciation is expressed to Dr. Jung-Ing Ker for his consultation on metrology. Many thanks are also extended to Dr. Norman Witriol and Dr. David Hall for serving on the research committee.

The LIGA personnel at the IfM, Mr. Phillip Coane and Mr. Robert Giasolli are acknowledged. Special thanks go to Dr. Jost Goettert for his guidance and suggestions for each step needed to accomplish this research project. The technical assistance of Ji Fang, Richard Miles, Joseph Blakeslee, Scott Williams, and Jeanette Futrell is greatly acknowledged.

Last but not least, my deep appreciation are due to my wife (Tsai-Ching), my parents, and my sisters for their encouragement and support. Their constant financial and spiritual help were enormously helpful in completing this work.

CHAPTER 1

INTRODUCTION

1.1 The Optical Fiber Ferrule

Information transfer and inquiry at a high rate is a necessary component of a modern society. Many system-oriented VLSI chips have been built in response to the enormous market demand for sophisticated electronic systems to handle the growing complexities of the Information Age. The Information Age means that high-capacity transmission lines have to be used for data transmission. An example of a high-capacity transmission line is the optical fiber cable designed, manufactured, and installed by General Cable for the U.S. Air Force's Arnold Engineering Development Center, working at data transmission rates up to 150 megabits per second (Mbps)[1].

The reasons for use of optical fibers are obvious: optical fibers are extremely light and small. They are virtually immune to electrical interference and can directly pass high voltage areas. Neither do they radiate outward the signal they carry, nor are they susceptible to induced signals. Optical fibers can carry light impulses from modulated light sources. The modulated light is launched into a length of fiber, where it reflects from wall to wall through the fiber core and then to a receiver. At the receiver, the light energy is converted back to electrical impulse to perform its original task[1]. An optical fiber

consists of a core (inner cylinder) and its cladding (outer cylinder) as shown in Figure 1. The core and the cladding have different indices of refraction.

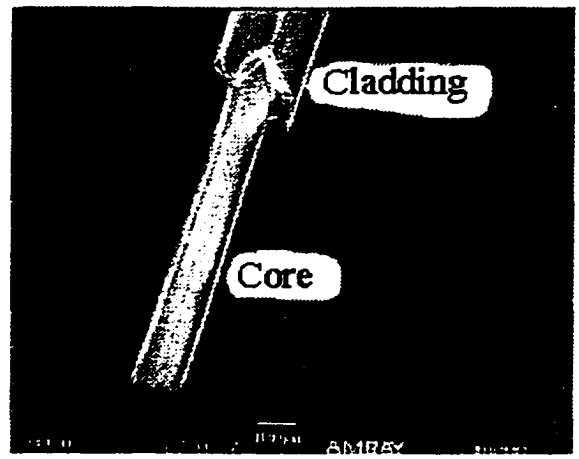

Figure 1. An optical fiber: a core and its cladding.

When a beam of light is propagated on a surface that separates two media such as air and water, part of the light beam is reflected back into the medium from which it came and part of the light is transmitted into the second medium according to Snell's law, which is illustrated in Figure 2. The angle made between the direction of incidence of the light beam and the normal is the angle of incidence. The angle between the normal and the direction of reflection is the angle of reflection. The ratio of the sine of the angle to the sine of the angle of refraction is equal to the index of refraction (n). When the angle of incidence changes, the refraction changes to retain the ratio. The equation is shown in Equation 1.1.

$$n_1 \sin\theta_1 = n_2 \sin\theta_2 \qquad (1.1)$$

if $n_1 = 1$ (air)

then $\sin\theta_1 = n_2 \sin\theta_2$ (1.2)

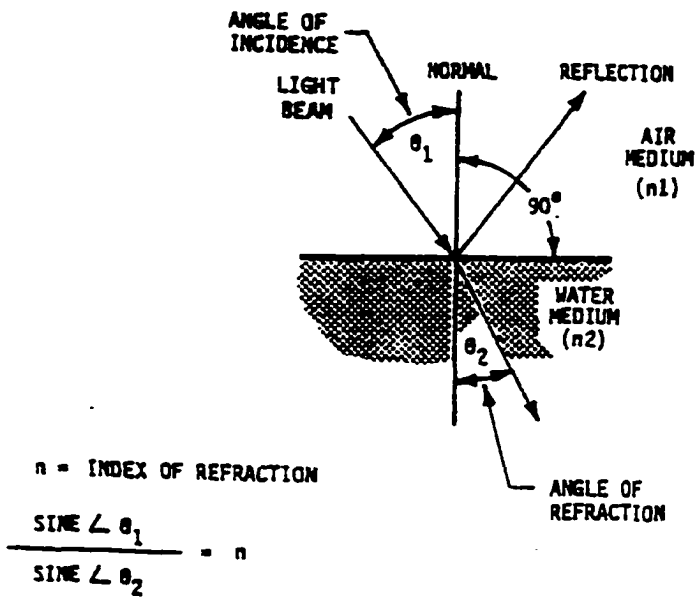

Figure 2. Refractive indexes and angles[1].

For the condition of total internal reflection, it is necessary that $\theta_2 = 90°$ [2]. Hence,

$$n_1 \sin\theta_1 = n_2 \quad (1.3)$$

When light is launched or coupled into the optical fiber and satisfies the condition of total internal reflection, it is transmitted from one end of the fiber to the other through a series of internal reflections. The amount of light emerging is almost the same as at entering. Optical fibers are built so that the light wave is propagated in a fiber by a series of reflections from an optical cladding of low refractive index. Thus the light is transported from a light source to a light detector. This operational function is shown in Figure 3.

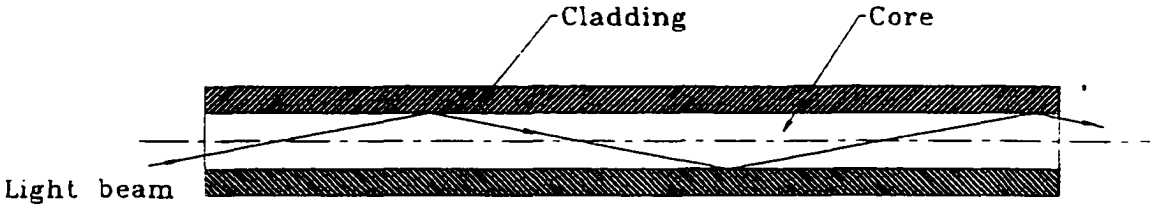

Figure 3. Light transport in an optical fiber.

Fibers are constructed to fill the need of a particular requirement. Two operating classes of fibers are single-mode and multimode. The two main differences between single-mode and multimode fibers are their bandwidth and attenuation. Single-mode fibers have bandwidth greater than 10 GHz while multimode fibers have a bandwidth of only 400 MHz. Power losses (attenuation) in the fiber optics are rated in decibels (dB). The attenuation of a single-mode fiber is 0.4 dB/km compared with a multimode with 3 dB/km. The above data show that single-mode fibers have 25 times greater bandwidth and 7.5 times less attenuation in performance than multimode fibers. In practice, single-mode links have been established with capacities of 560 Mbit/s and repeaters every 40 km while multimode links have capacities of 144 Mbit/s and repeaters every 20 km. The technology of single-mode optical fibers is much more difficult to implement with respect to installation, debugging, transmitting and receiving components as well in connection [2].

Two major forms of fiber misalignment related to connectors cause coupling loss in the optical fiber connections. Lateral misalignment is the displacement between

centerlines of the cores in the two mating fibers as shown in Figure 4. Power loss in decibels is plotted as an L/D ratio[1], where L is the lateral displacement, D is the core diameter, and C.D. is the channel diameter of connector.

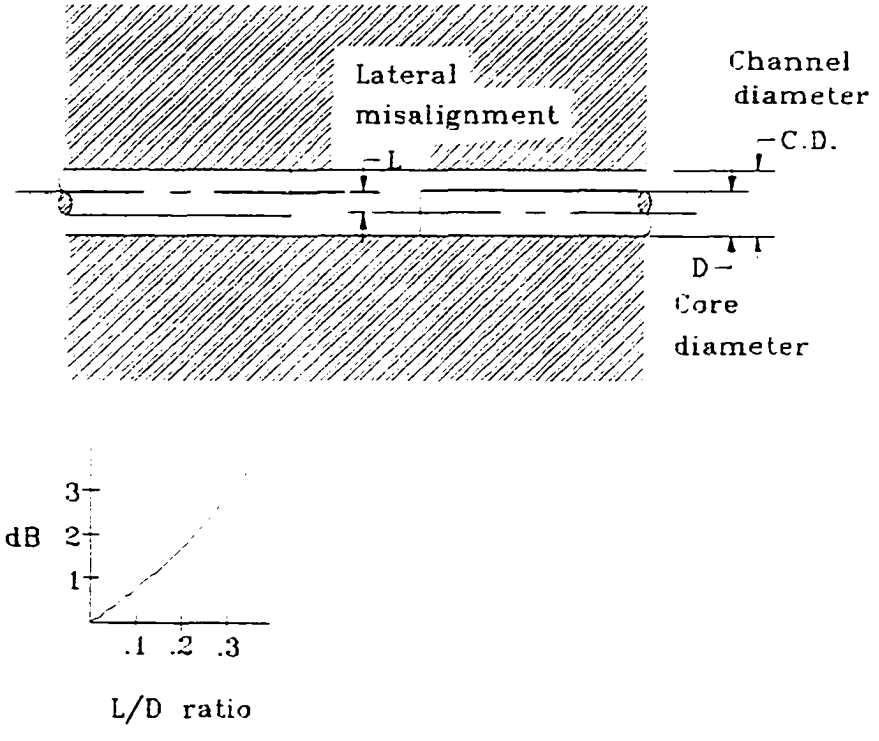

Figure 4. Lateral misalignment of fiber cores in a channel.

Angular loss is caused by two mating fibers whose channels form an angle as shown in Figure 5 or by cutting the fiber ends at an angle or by preparing the faces of the fibers so that they are not symmetric. Again, the power loss is expressed in decibels. Angular losses are plotted as decibels versus angle in degrees, where the angle is measured between the two mirror fiber end faces. A typical allowed angle is less than 0.25°.

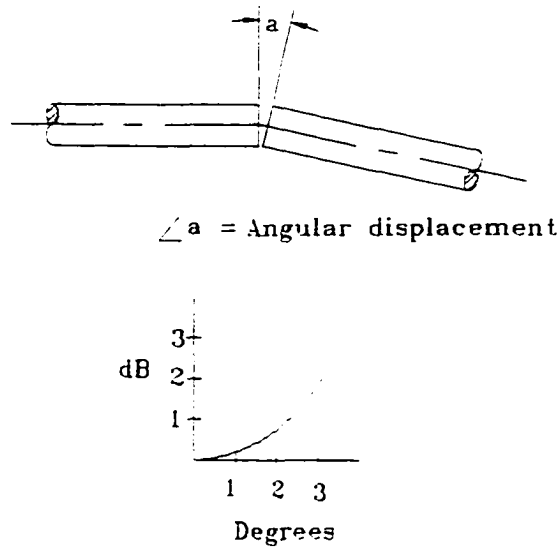

Figure 5. Angular loss between two fibers.

1.2 Objective

The objective of this research is to develop the basic steps to fabricate a single-mode optical fiber ferrule mold insert with twelve channels. This research project is the result of a research contract with the Siecor Co.. An ideal fiber-to-fiber ferrule will align the center of the cores to minimize the signal losses, These loses should be within 0.25-1.0 dB. In order to satisfy the desired alignment tolerance for each fiber, high-precision and low-tolerance inserts with micro-scale feature sizes are required. The required feature size accuracy for a single-mode fiber core is 126 μm in diameter with up to 0.5 μm tolerance; spacing accuracy from center to center is 251 μm with +/- 0.25 μm tolerance as shown in Figure 6. The final goal is to implement the LIGA technique in the Institute for Micromanufacturing (IfM) at Louisiana Tech University to produce a metallic injection mold with 1 mm thickness and with the above stated precision.

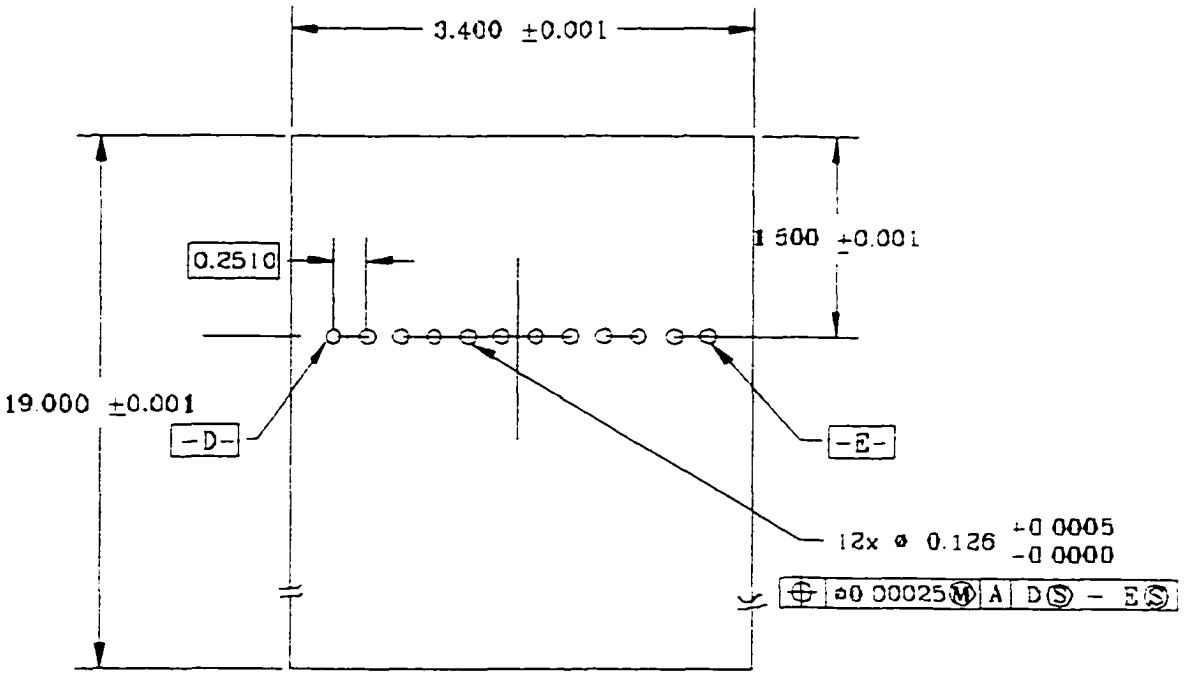

Notes:

1. All dim. in mm
2. Thickness : 1.0 mm

Figure 6. Schematic of a single-mode optical fiber ferrule, showing dimensional tolerances: units are marked.

CHAPTER 2

LITERATURE REVIEW

The large demand for low-weight and small-volume devices has proved the worth of micromanufacturing. Microfabrication with deep X-ray lithography (DXRL), also known as LIGA (German acronym for **LI**thografie, **G**alvanoformung, **A**bformung), is a sequence of X-ray lithography, electroforming, and injection molding steps [3] for fabricating microstructures with high aspect ratios. In contrast to other processes, LIGA is superior in the mass production of microstructures of extremely high aspect ratio and vertically structured walls, and allows fabrication with a variety of materials [3,4,5]. Figure 7 is a diagram of the LIGA process to fabricate a metallic mold.

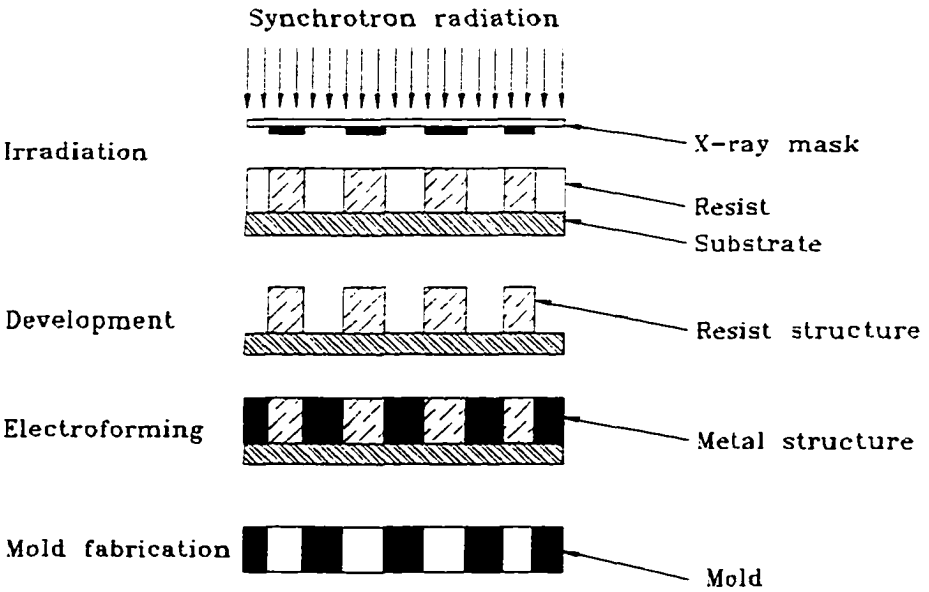

Figure 7. The LIGA process to fabricate a metallic mold.

A mask is the initial component in the fabrication of microstructures with DXRL. The mask is used to transfer a desired pattern into a photoresist by selectively blocking and transmitting X-ray photons. It consists of a thin membrane of low atomic number material largely transparent to X-rays and a patterned absorber of high atomic number material [3,6].

The thin membrane is the mask blank that supports the absorber pattern. The mask blank materials have to meet these requirements: high X-ray transparency, high thermal conductivity, very low thermal expansion coefficient, and high Young's modulus. Diamond, boron nitride, titanium, silicon carbide, silicon nitride, silicon, and polyimide are commonly used as mask membranes. Research on these and other materials was done at Fraunhofer-Institute for Mikrostrukturtechnik (IMT) [7,8]. Polysilicon and silicon nitride were studied at the University of Wisconsin, Madison [9,10]. Other metallic mask membranes, such as titanium and beryllium, were studied at Forschungzentrum Karlsruhe (KfK) in cooperation with Degussa [6]. These studies indicated titanium and beryllium can serve as mask membranes as shown in Figure 8. The transmission of mask materials is a function of the membrane thickness, and titanium and beryllium are highest transprancy metals.

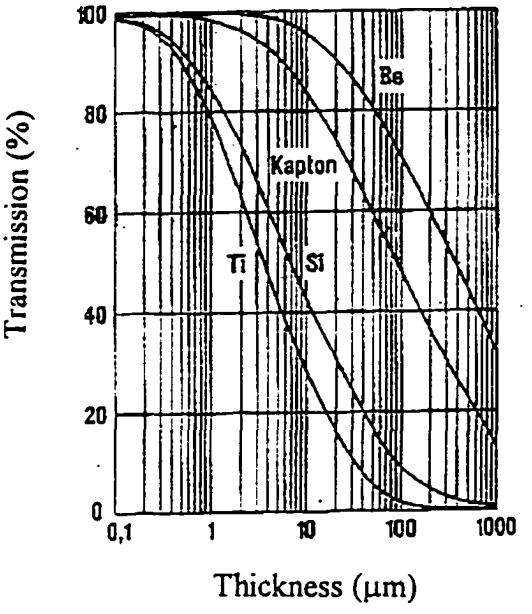

Figure 8. X-ray transmission at characteristic wavelength, λc = 0.25 nm[11].

High atomic number materials such as gold and tungsten are suitable materials for the absorbers. Figure 9 illustrates the relationship between gold absorber thickness and the resist height to achieve complete exposure.

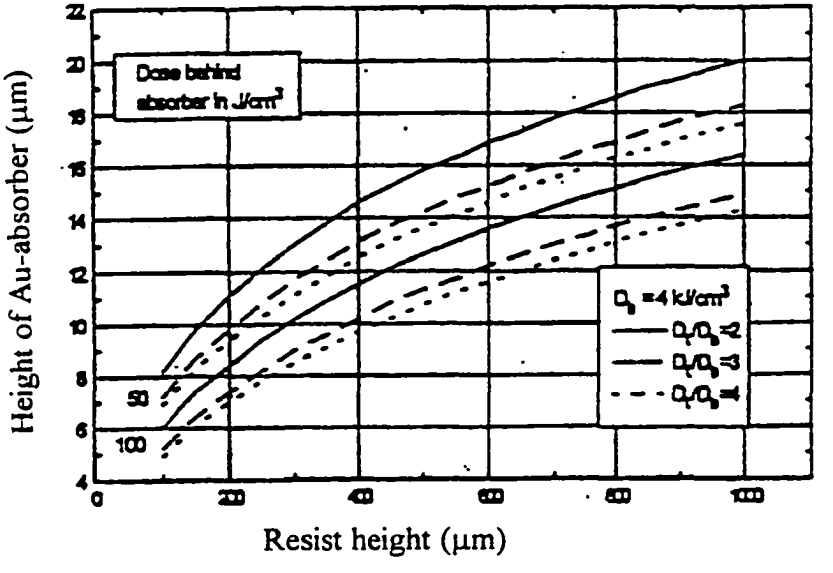

Figure 9. Height of the gold absorber as a function of the resist height[12].

The fundamental steps in the fabrication of deep X-ray masks by KfK are as follows: (1) The surface of a metal plate (beryllium foil) is polished to a roughness of Ra < 0.1 μm. (2) From the rear side of the plate, a window is made with a residual thickness of 1 mm. (3) The material for the mask membrane is applied by a physical vapor deposition (PVD) process followed by a starting and adhesion-promoting layer (such as copper) for the absorber patterns. (4) After deposition of a metal plating base, a 20 μm thick polymethyl methacrylate (PMMA) resist foil is laminated with cyanacrylate on the substrate. (5) The window is then etched into the metal frame by a selective etchant. This process leads to mask blanks consisting of a metal frame supporting the stretched metallic membrane with the resist in place. (6) The absorber pattern is transferred by printing an X-ray mask or by using a 100 KeV electron beam (E-beam) to write on the PMMA resist [11,13]. After developing the PMMA resist, the gold is electrodeposited onto the structure. After stripping the resist and the cyanacrylate, the working mask is ready for use. The study of deep X-ray mask fabrication at KfK provides a classical mask-making method.

Synchrotron radiation is an intense and highly collimated electromagnetic X-ray radiation with short wavelength used to irradiate PMMA resist in the LIGA process. Three-dimensional microstructures are obtained by projecting the two-dimensional absorber patterns of the mask into the polymer, leaving a latent image in the exposed part, which is developed after irradiation. A dose of at least 4 KJ/cm^3 is chosen at the PMMA-substrate interface. On the surface of the resist a maximum dose of 20 KJ/cm^3 should not be exceeded. Higher doses result in the formation of cracks and bubbles. According to IMM's research, for doses smaller than 100 J/cm^3 below the mask absorber, no dissolution of PMMA is observed [12].

PMMA is the accepted standard resist material, which can be patterned at thickness of several hundred microns (up to 1 mm) in the LIGA process. Resist films are obtained using a casting process. The casting solution contains poly(methyl methacrylate), a cross-linking agent (polyfunctional methylmethacrylate), a reaction accelerator, an adhesion promotor, and methylmethacrylate. The addition of benzoylperoxide starts the polymerization. PMMA offers a high resolution and affords no swelling of the structures during the developing process. The structures exhibit smooth side walls which are necessary for the molding process, and they are stable in the electroplating step[14].

A version of electroplating called electroforming is used. Electroforming makes a metallic object by performing the electroplating process to fill the voids (created in the X-ray exposure and development) with metal[15]. Nickel is a common material for electroforming because it provides greater strength, hardness, and corrosive resistance when compared to other metals, such as copper and iron[16]. Many microstructures have been made by nickel electroforming[3,4,5,17,18,19]. Among various nickel baths, the nickel sulfamate bath produces a high deposition rate and the least tensile stress[20]. Therefore, high aspect ratio microstructures can be implemented in metal.

The LIGA technique surpasses the possibilities of conventional precision machining, especially in mass production and precision of replication. The general conventional processes for machining metals can be described as follows. A sharp-edge tool of hard material is moved through a softer workpiece. The harder and sharper the cutting tool, the smaller the force required to make the cut. But other factors must be considered, such as lubrication and cutting edge. The tool point has to be strong enough to withstand the forces to which it is subjected, and the material of the tool must be resistant to abrasion as a result of rubbing

across the workpiece. The work done against friction and plastically deforming the workpiece causes the temperature of the tool point and workpiece to rise. The increased temperature usually helps in plastic deforming the workpiece, and also tends to increase the deformation and wear of the tool[21]. These deformations and tool wear result in low precision of products.

In micromanufacturing, the goal is to produce mini/micro systems with components with sufficient tolerances to achieve functionality and repeatability. The desired development in optical fiber connector production is the realization of tolerances in a range of +/- 0.5 μm. Conventional precision tools might have the capability to machine soft materials (such as PMMA and copper) to the accuracy of several microns, but they cannot machine hard materials (such as nickel and ceramics) due to tool wear and material machinability. It may, however be possible to use conventional micromachining techniques to rapidly produce a LIGA mask. It may also be possible to fabricate a high-precision optical fiber ferrule mold with the LIGA technique. Weber used the LIGA technique to fabricate a precision ferrule as the main part of a push-pull connector for 12 single-mode fibers[22]. The technique was used to achieve a very accurate ferrule for insertion losses less than 1 dB.

Small-size push-on optical fiber connectors were constructed by Nagasawa et al[23] as shown in Figure 10. The push-on type single-fiber and 5-fiber ribbon connectors are for 50 to 125 μm graded-index (multimode) fibers. The plug contains a plastic ferrule which is accurately molded using a multi-V-groove molding method. The results are entirely satisfactory for practical use since these connectors have insertion losses of less than 0.1 dB.

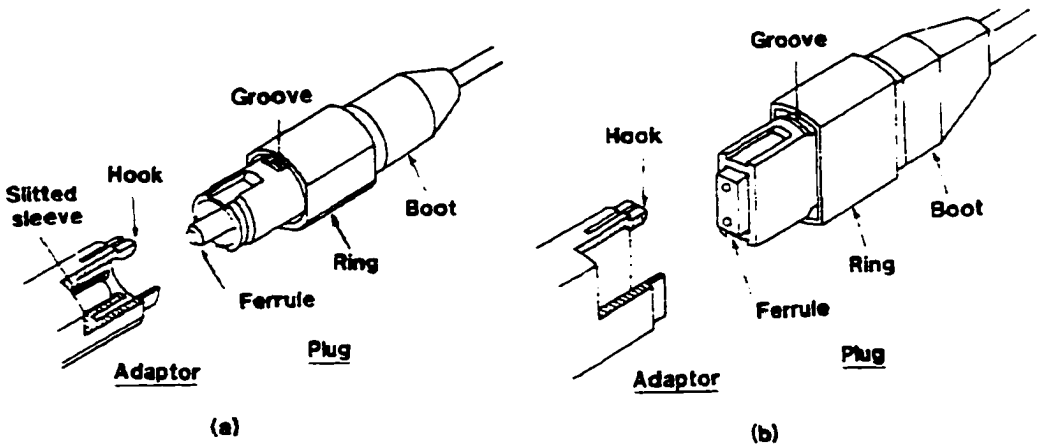

Figure 10. Schematic of push-on type connectors[23].
(a) Single-fiber connector.
(b) 5-fiber-ribbon connector.

CHAPTER 3

FABRICATION PROCESS DESIGN

The development and realization of a single-mode optical fiber ferrule mold insert with twelve channels is the objective of this study. A nickel mold is the final product for this project. Dimensional accuracy control is the main problem for this fabrication process. The LIGA process has the highest possibility of accomplishing the final result as discussed earlier. A flowchart to achieve this goal is shown in Figure 11. Experimental methods are used to investigate the feasibility of ferrule mold making from the design processes.

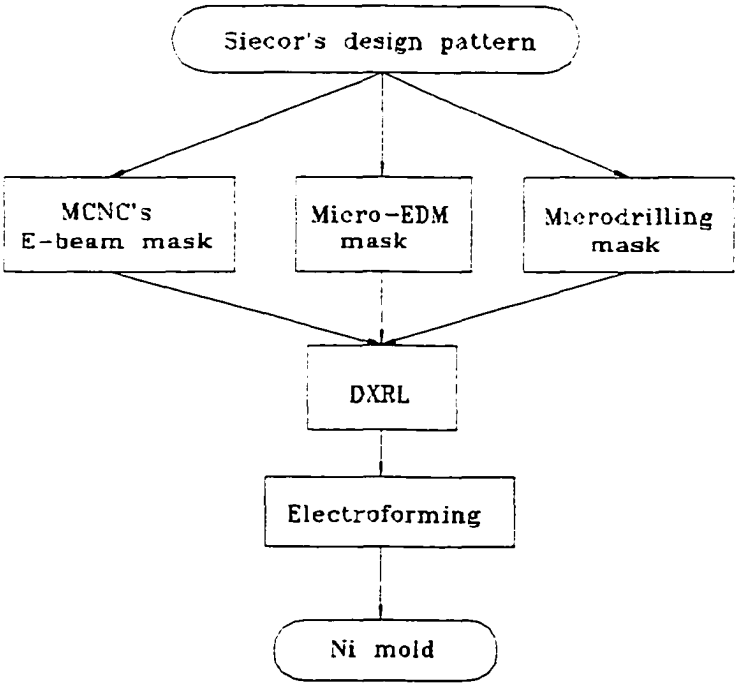

Figure 11. A flowchart for the fabrication of the optical fiber ferrule mold.

Optical fiber ferrule patterns came from the Siecor Company. Single-mode optical fiber cores (125 μm in diameter) are the fibers for insertion into ferrule channels. Each of the channels is separated by 251 μm from center to center of channels. Three methods are attempted for making X-ray masks: an E-beam written mask, a micro-EDM machined mask, and a mechanically microdrilled/micromilling mask. The E-beam written mask was made by Microelectronic Center of North Carolina (MCNC), except for AutoCAD drawing designs and GDSII translation which were done at the IfM. The micro-EDM machined mask was made in cooperation with National Yunlin Sicenece & Technology University in Taiwan. The mechanical machined mask was made on IfM's precision microdrill/micromilling machine. Precision and economic efficiency are the main objects for using different X-ray mask production methods. The results of this comparison of mask production methods provide their accuracy limits and economy, indicating the best method for future use.

The deep X-ray lithography process includes seed layer deposition, PMMA bonding, irradiation process, and development after exposure as described in the LIGA process. The LIGA process is based on a combination of deep X-ray lithography (synchrotron radiation) and replication processes and allows generation of three-dimensional microstructures from metals, polymers, glasses and ceramic materials. The desired goal is to control each key parameter in dimensional accuracy and meet the product requirement in the fabrication process. Three main accuracy-control steps are mask fabrication, deep X-ray lithography exposure, and electroforming. Precision of the mask is still a challenging issue. As illustrated in Figure 12, three mask-making methods are proposed in this research. Deep X-ray lithography exposure accuracy is a function of

X-ray beam divergence, scanner alignment, and exposure conditions. Nickel electroforming accuracy is associated with the effect of bath temperature on the resist structure dimension. In sum, ferrule mold dimensions have to meet the requirement of the design accuracy by controlling the processes in the fabrication chain.

CHAPTER 4

X-RAY MASK FABRICATION

4.1 Introduction to E-beam Written Mask Fabrication

X-ray masks used in the LIGA process can be classified as intermediate or working masks. The intermediate and working masks have similar materials which include a membrane and absorber structures. The intermediate mask typically has thinner absorber structures than the working mask, and is not thick enough to produce high aspect ratio resist patterns. On the other hand, the working mask has sufficiently thick absorber structures to produce resist patterns with desired thickness. The intermediate mask has an opposite tone to the working mask since the replication process to the working mask generates an opposite tone. When a researcher is designing a mask, the first step is to decide if the mask is an intermediate mask or a working mask.

Several methods can be used to fabricate intermediate and working masks. Standard ultraviolet (UV) lithography and direct writing by E-beam lithography are commonly used to prepare intermediate masks, while the working mask is made by printing from the intermediate mask. The standard UV lithography method uses a chromium (Cr) mask like in the semiconductor industry and a 1:1 mask alignment. UV lithography is used to expose about 2.5 μm thick photoresist, and the resist patterns are then formed on a mask blank. After electroplating gold and removing the resist, this

intermediate mask can be used to expose around 20-30 μm thick PMMA by using soft X-rays. UV lithography can expose high resist thickness, but the dimensional accuracy of this process is about 1-2 μm[24], which is insufficient for this project. However, mask-making can be achieved by an E-beam writing process for high accuracy required by optical fiber ferrule molds

E-beam lithography has been one method for defining masks since the late 1970s. An E-beam writer with energy 50 KeV suitable for writing X-ray masks with critical dimension down to 0.35 μm was reported by Groves et al[25]. The E-beam system provides the needed resolution, throughput, and automated pattern data processing capability. With the above advantages, E-beam writing of masks is the better method than optical lithography. An E-beam writer with energy 100 KeV can directly write 10 μm thick resist with accuracy of the resist patterns in the submicron range. After plating gold and removing the resist, this mask can be an intermediate mask allowing exposure of 20-30 μm thick PMMA by using soft X-rays for making a working mask. A 10 μm thick gold absorber may also be a working mask to expose up to 500 μm thick PMMA resist patterns. Using an E-beam writer to define the mask of an optical fiber connector is an essential and beginning part of this research. The details are described in the following section.

4.2 GDSII Translation and Mask Design

4.2.1 Drawing rules for the mask design

GDSII translation software (ASM 3500) is developed by the Artwork Conversion Software Co. It allows bidirectional translation between AutoCAD's DXF and GDSII files. Although the ASM 3500 bidirectional translator has a general design guideline for mask design, some practical details and procedures still need to be described here. Six drawing rules are introduced here to promise good AutoCAD drawings which will translate into GDSII files for the required optical fiber connector patterns.

1. Determining the final structure.

An E-beam mask fabrication process used by MCNC is shown in Figure 12. The E-beam writes directly on a positive resist and the chrome is etched the exposed portion. The Cr mask serves an intermediate mask which is in reverse tone. An X-ray mask membrane (2 μm thick Si) is coated with 10 μm thick negative resist from JSR (Japanese Synthetic Rubber). The Cr mask is transferred to the X-ray mask via 1x projection lithography (SVGL scanner) with an UV source centered around 400 nm. After the development of negative resist, the gold absorber is plated onto the X-ray mask membrane. This process shown in Figure 12 indicates that the E-beam written area corresponds to electroformed area on the final structures.

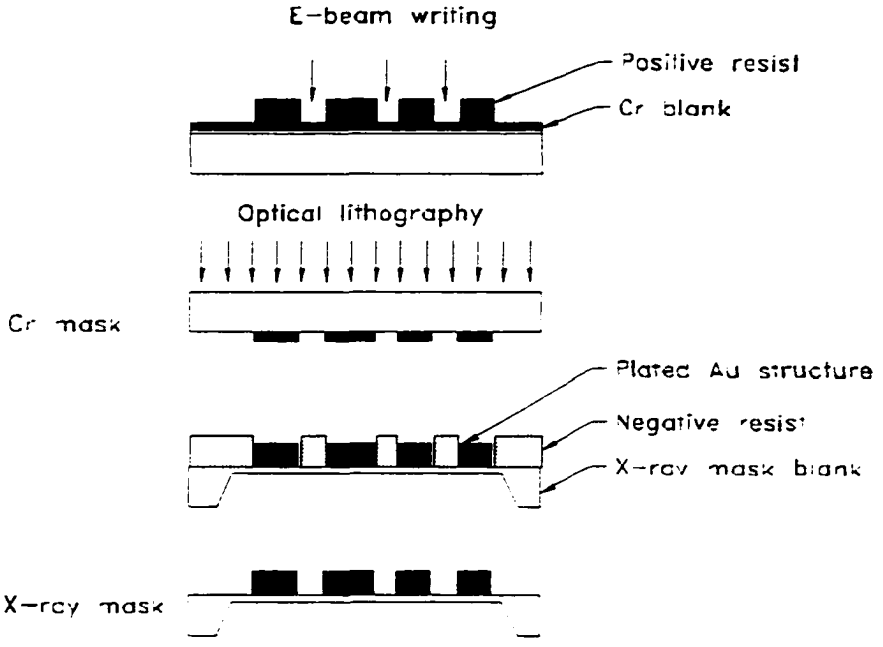

Figure 12. Fabrication process of E-beam written masks.

Two tones used in this study for the optical fiber ferrule are designed as illustrated in Figure 13. The dark area is an E-beam written portion that is a clear tone on the Cr mask. The exposed portion is etched away and shows "clear". In the intermediate mask design, the twelve isolated columns and frame are open areas. In the working mask design, the twelve isolated columns and frame are gold absorber.

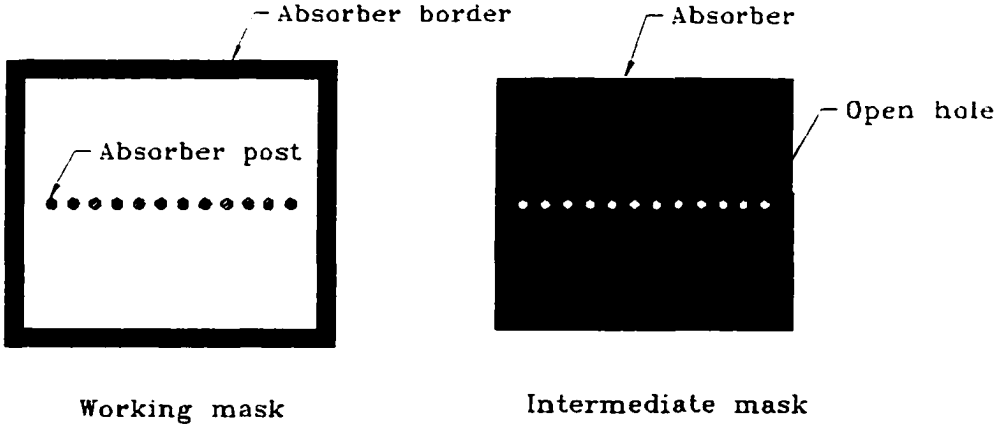

Figure 13. Absorber tones of intermediate and working masks.

2. Placing similar structures on a neighboring area

The consideration of similar structures placed on a neighboring area is based on minimizing exposure area. The field of a mask usually contains several designs, but it is not necessary to expose the whole field each time. The numerical aperture of the scanner can be adjusted to expose only a certain portion of mask; therefore, it is possible to minimize exposure time and area.

3. Effective layout

Mask design is always subject to space limitations. Thus, an effective layout means that all design patterns should be laid out on the minimum field size, compatible with development of the exposed resist.

4. Closed boundaries

All segment parts of design patterns should be in a closed boundary. Interior and exterior should be completely separated by the figure boundary. An open boundary will not be read by an E-beam writer.

5. Arcs and circles

ACAD2GDS converts DXF arcs/circles into linear segments, and GDSII has no arc/circle entities. One must select the number of degrees substituted by the chord in ARCRES of the GDS.CFG menu. The method to determine a proper arc without affecting accuracy of the approximation of an arc to a circle is shown in Figure 14. The difference can be calculated from Eq. (4.1).

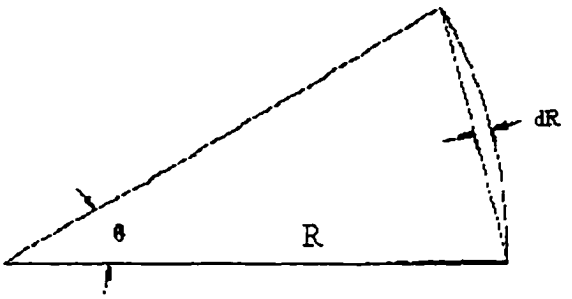

Figure 14. Geometric variation between the arc and the chord approximation to the arc.

$$1-\cos(\frac{\theta}{2})=\frac{dR}{R} \tag{4.1}$$

Where θ is the angle of the arc, R is the radius of the circle, and dR is the difference in radius between the arc and chord.

Table 1 lists the effect on radius dimension accuracy for an optical fiber channel with nominal diameter 126 μm as a function of the angle θ in the design. The precision of the hole diameter is within 0.5 μm; therefore, the arc should be less than 10 degrees to minimize the difference between nominal design and the required tolerance. In practice, the arc was designed as 8 degrees for the optical fiber ferrule molds. Since there is a vertex limitation of a closed boundary within the translator program, the arc degree number cannot be infinitely small to minimize bias from nominal design. The vertex limitation will be explained in the following section.

Table 1. The effect of arc size on the radius dimension according to theoretical calculations.

Arc degrees	Radius difference	Bias from nominal size
2	0.0095	125.981
4	0.038	125.938
6	0.086	125.828
8	0.153	125.694
10	0.239	125.522
12	0.345	125.310

6. Vertex limitation

In the conversion of GDSII files, the number of vertices are limited no less than 3 vertices and up to 4096 vertices per boundary are allowed. If a design pattern includes more than 200 semicircles or 100 circles in a closed boundary, it will cause the program to be over the vertex limitation. If a pattern is over the vertex limit, the closed boundary must be divided into two segments to satisfy the design rules.

4.2.2 E-beam mask design

The X-ray mask used in this work is four inches (interior) in diameter with a supporting frame. Two fields have been designed on this mask as shown in Figure 15. Field 1 is an intermediate mask (Figure 17) and field 2 is a working mask (Figure 18). Each field has dimensions of 25mm by 40 mm. Since this X-ray mask costs about $4,000 to make, other designs also exist in both fields. They are for microchannels, optical components, and test patterns.

To accomplish a precise dimensional achievement on optical fiber ferrule molds, dimensional variation from the nominal size are designed on the mask. Hole diameters have a 0.5 μm variation from the nominal 126.0 μm and pitch distances have 0.1 and 0.2 μm variation from the nominal 251.0 μm. The designed dimensions of two masks are shown in Figure 18 and 19.

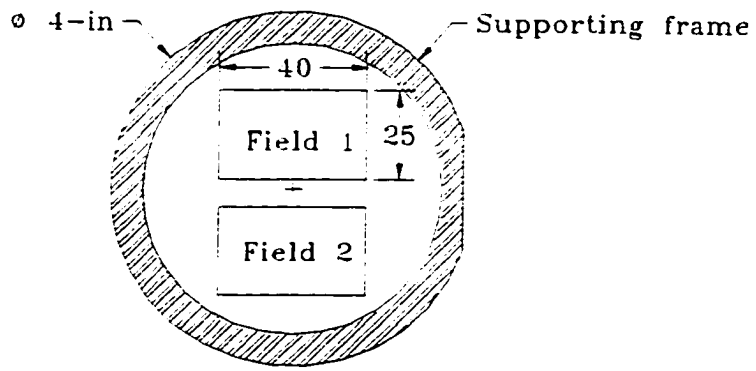

Figure 15. Field sizes on the X -ray mask.

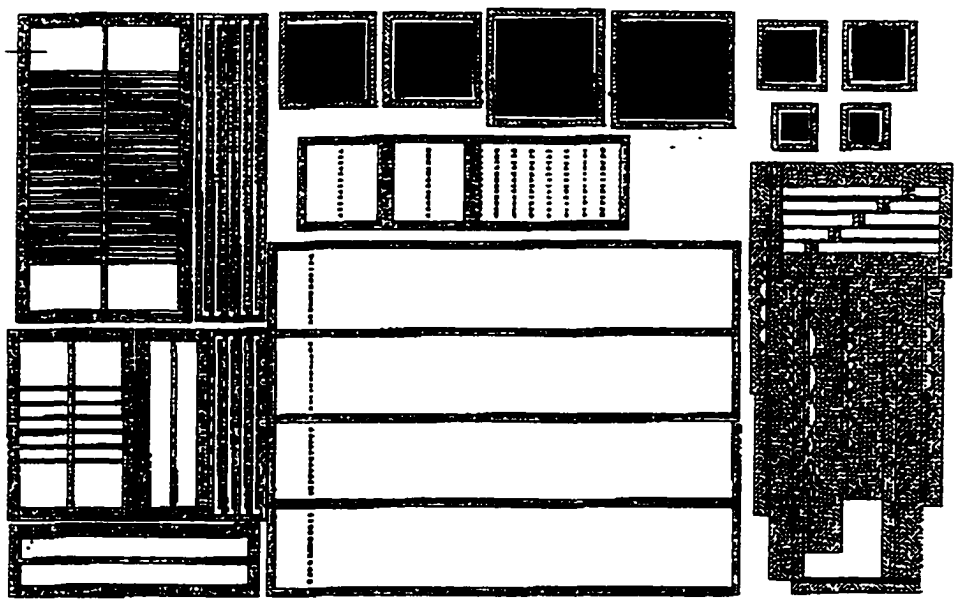

Figure 16. Design patterns on Field 1.

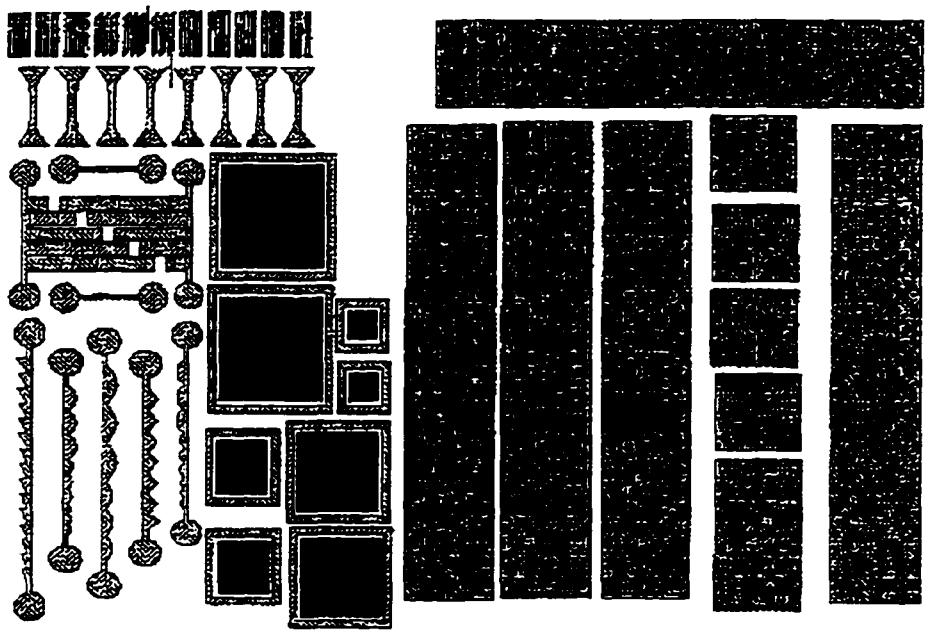

Figure 17. Design patterns on Field 2.

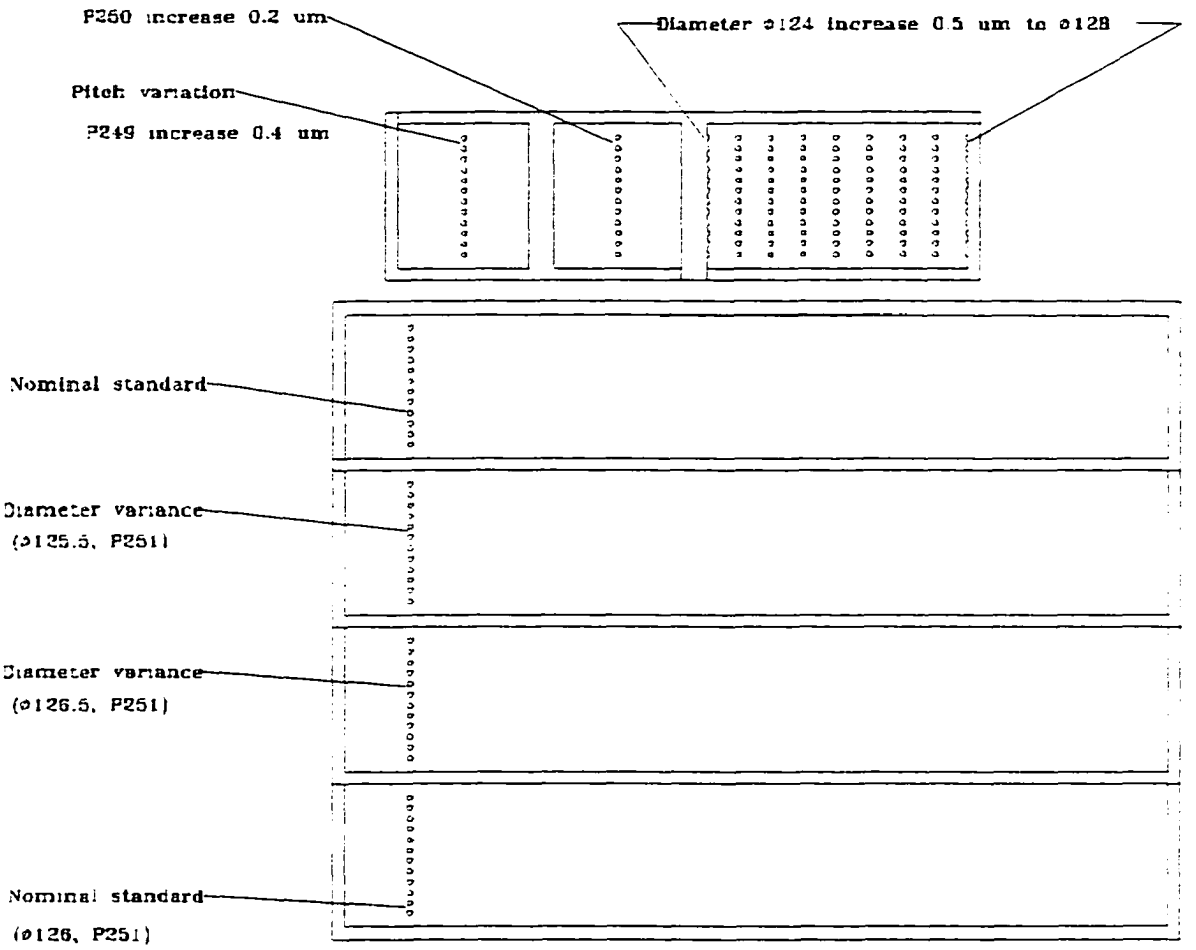

Figure 18. Dimensional variations in Field 1 (the intermediate mask tone for the optical fiber ferrule mold insert), P251 means the pitch distance is 251 μm.

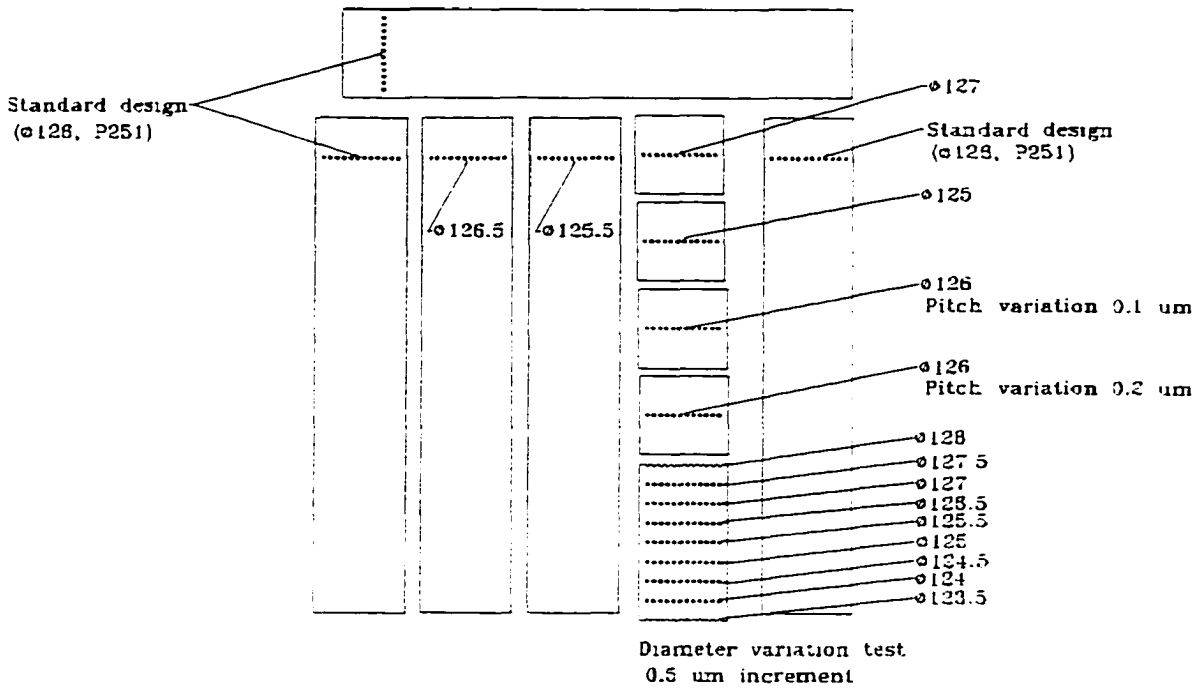

Figure 19. Dimensional variations in Field 2 (the working mask tone for the optical fiber ferrule mold insert), P251 means the pitch distance is 251 μm.

4.3 Mechanically Machined Masks

Mechanical machining methods were attempted to fabricate an intermediate mask for an optical fiber ferrule. The IfM has an ultra-high-precision micromilling/microdrilling/micro-EDM (Electrical Discharging Machining) machine shown in Figure 20. All axes have air bearings for added stability and smoothness of travel. The x and y motions of the work table use a laser interferometric position control with a commanded resolution of 1.25 nm. The work table is driven by linear DC brushless servo motors with overall travel distance 150 mm. The z motion is controlled by a linear encoder positional controller with a commanded resolution of 20 nm. A DC brushless servomotor drives a high precision leadscrew with vertical travel distance 150 mm. The micromilling head uses a vee-block bearing arrangement which has upper and lower pair of convex diamond bearing pads (Figure 21). Each pair of surfaces create contact points which are 90° apart and the two pairs of surfaces are separated by a vertical distance of 38 mm, forming a stable, four-point support system for the milling tool mandrel. The milling tool is driven by a pulley and flexible silicone rubber belt and controlled to 20,000 rotations per minute (RPM).

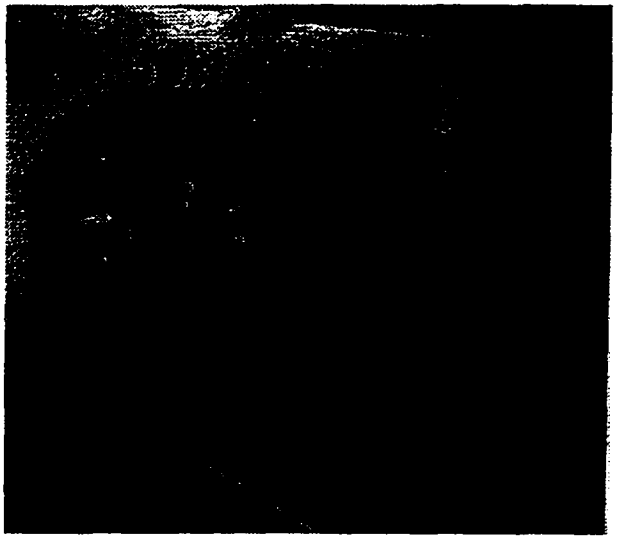

Figure 20. High-precision micromilling/microdrilling/micro-EDM machine.

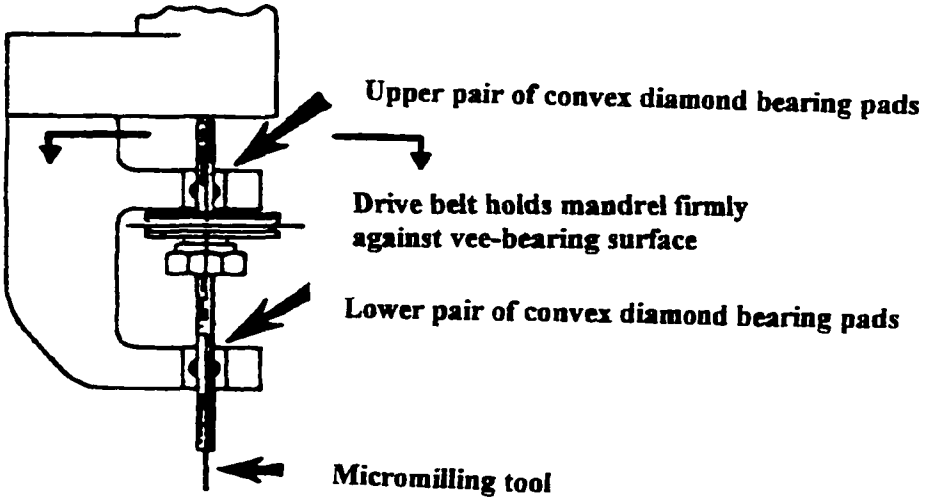

Figure 21. Vee-block arrangement for holding milling tools with extreme concentricity (Courtesy National Jet Company).

The trial work used a 150 μm diameter micromilling tool to directly cut the absorber layer to form microstructure patterns on a mask. The mask membrane material was a 125 μm thick graphite film with 8 μm thick sputtered gold absorber film. The exposure results are shown in Figure 22, which is an exposed and developed pattern in

250 μm thick PMMA. The resist pattern is the same tone as the optical fiber ferrule mold, but without required dimensional accuracy. Hole diameters are about 160 μm with variance +/- 2 μm. Table 2 is a summary of the results of hole diameter measurements on the exposed PMMA pattern as shown in Figure 22. Each data represents the mean of five measurements. Since optical fiber ferrule molds require hole diameters at 126 μm - 0.0/+0.5, this result is obviously not acceptable.

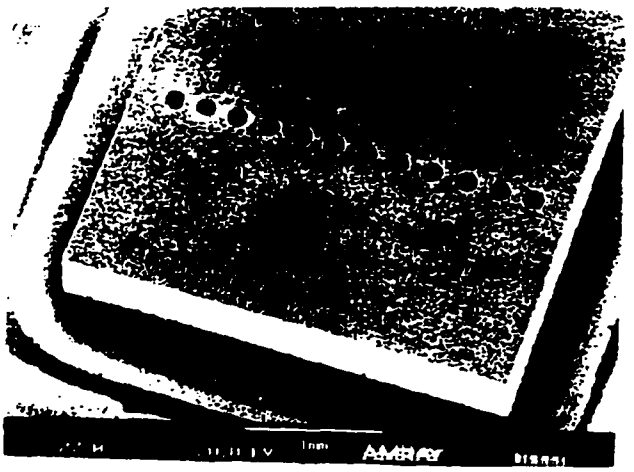

Figure 22. Exposed and developed resist pattern from a mechanically machined mask for an optical fiber ferrule, scale bar = 1 mm.

Table 2. Hole measurements for a mechanically machined mask exposure in 250 μm thick PMMA.

Hole	1	2	3	5	6	7	8	9
Mean	161.5	161.48	162.0	161.34	161.52	160.96	161.76	162.36

Though this method provides rapid mask making, it has limits on dimensional resolution and structure geometry. A milling process cannot machine rectangular edges required for the optical fiber mold. Furthermore, only the intermediate mask can be made by this method. The micromilling drill can make twelve holes and machine the

surroundings of the rectangle. But this working mask requires machining the inside of the rectangle, which cannot be machined by a milling tool because machining a corner with a milling tool naturally gives a round edge. A working mask of the optical fiber ferrule mold cannot be directly made by the technique of mechanical machining because of such geometric limitations. Lithographic methods, on the other hand, have no such geometric limitation on design patterns.

Figure 23 shows a nickel column electroformed from the resist mold after stripping the resist. The resist mold came from the exposure of the mechanical machined mask. Mechanically machined masks have burrs on the edges of holes. These burrs on the mask caused stripes on the edges of the resist after exposure as well as on the nickel posts after nickel electroforming. The side wall surface of the nickel post is not smooth, and the roughness will cause problems when inserting optical fibers. Figure 24 shows the side wall surface of a Ni column, the roughness (Rt) is larger than 5 μm. This result also cannot meet the requirements of the optical fiber ferrule.

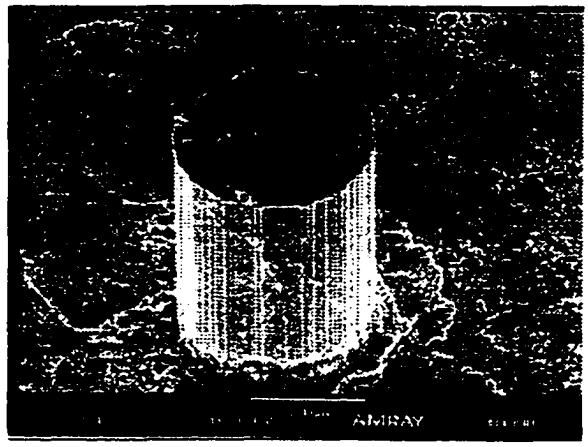

Figure 23. Nickel column after stripping resist mold, scale bar = 100 μm.

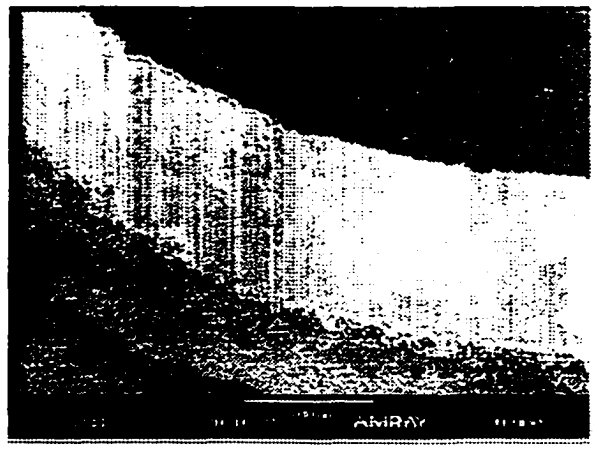

Figure 24. Side wall surface of a nickel column, scale bar = 10 μm.

4.4 Micro-EDM Masks

4.4.1 Micro-EDM machining

Electrical discharge machining (EDM) is one of the most reliable methods for micro-hole drilling. It is an important machining process in conventional manufacturing, especially for hard materials. High-speed steel, high-carbon steel, tungsten, and titanium are frequently machined by EDM.

The mask materials used are the same as those of regular X-ray masks which include membrane and absorber. The absorber is bonded to the membrane before patterning. EDM will pattern the absorber and can be used to form either an intermediate mask or a working mask. Simple geometric patterns like small holes can be made by micro-EDM. Masuzawa et al[26] modified a conventional EDM system to fabricate electrodes on the micron scale. The electrodes are made on the same EDM machine by WEDG (Wire Electrical Discharge Grinding) with reverse polarity. That precaution prevented some degree of error from occurring through the clamp, since electrodes are usually less than 1 mm in diameter and not easy to handle. With the WEDG to shape the

dimensions and keeping the same rotational center of electrode, straightness and rotational center of the electrodes can be maintained. The results showed the deviation of the machined diameter to be less than +/- 1 μm from the mean diameter. The micro-EDM technique, with its high accuracy, can be a useful tool to machine absorber patterns on X-ray masks.

The EDM system (Figure 25) consists of a shaped tool (electrode) and the workpiece, placed in a dielectric fluid[27] and connected to a DC power supply. Material removal is based on erosion of metal by spark discharges. When the potential difference between the electrode and the workpiece is sufficiently high, a transient spark discharges through the fluid, removing a very small amount of metal from the workpiece surface. A rectangular electrode can be machined by a flat electrode to make one side, then rotated 90° to the flat electrode to machine the other side. Thus, the right-angle inside corners of the ferrule pattern can be machined by a rectangular electrode of the EDM system.

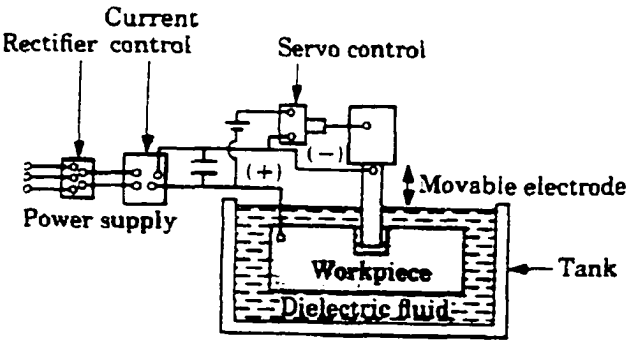

Figure 25. Schematic illustration of a conventional EDM system[27].

Two mask materials were attempted for the optical fiber ferrule insert mask, a tantalum (Ta) mask and a tungsten (W) mask. Both masks used graphite (250 μm thick)

as a mask membrane when exposure. Tungsten foil (25 μm thick) was used as an absorber bonded to graphite by using colloidal graphite. Figure 26 is the intermediate mask of the optical fiber ferrule machined by micro-EDM machining. This intermediate mask (tungsten with 25 μm thick) has 12 holes of nominal 126 μm diameter with boundary 3.4 x 19.0 mm.

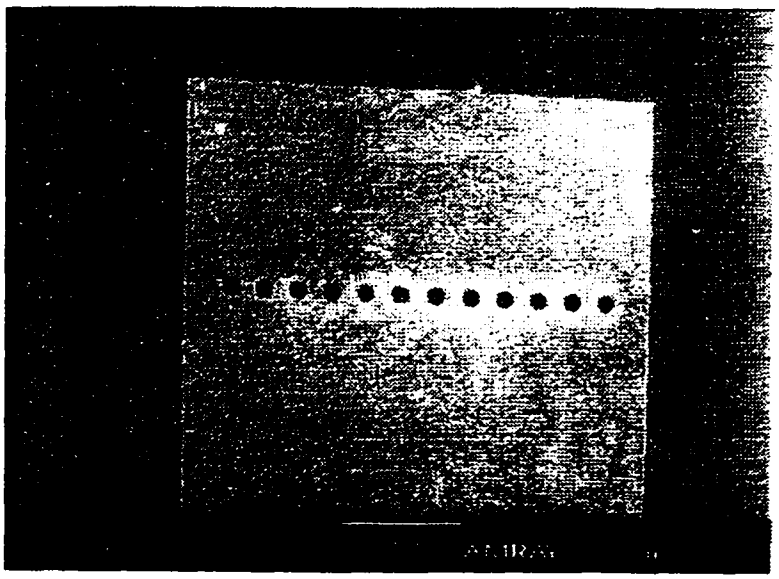

Figure 26. An illustration of a micro-EDM machined intermediate mask; 25 μm thick tungsten, scale bar = 1 mm.

The open holes and square box boundary were machined by the micro-EDM machine. The tungsten mask was machined while it was free from the graphite since heat expansion during electrical discharge caused the colloidal graphite to lose its effect on bonding the tungsten foil. This work was done in cooperation with National Yunlin Science & Technology University in Taiwan.

Figure 27 shows a vertical type micro-EDM machine[29]. The micro-EDM machine is used for machining workpieces and shaping electrodes; the machining process

and the electrode shaping process have reverse polarity. Polarity is changed by a double-pole double-throw switch. The micro-EDM working mechanism is similar to Masuzawa's which includes a WEDG mechanism to machine electrodes. A PC control is used to run operational parameters, such as axis motion, feedrate, and discharge current. Four sections are needed here to describe this micro-EDM machine: spindle head mechanism, RC circuit, WEDG mechanism, and cooling system.

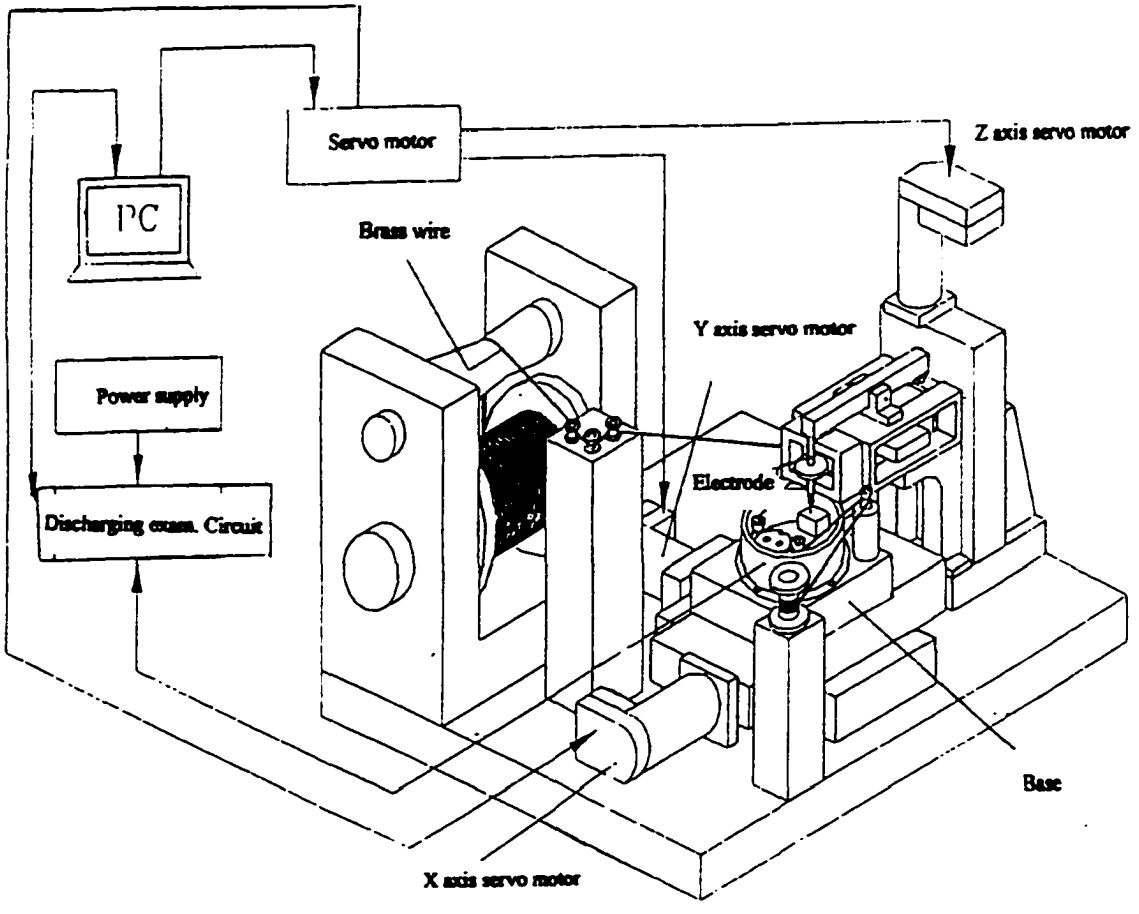

Figure 27. A vertical type micro-EDM machine in the National Yunlin Science & Technology University[29].

(1) Spindle head mechanism

Figure 28 shows the detail of the spindle head mechanism. The motion control of the spindle head mechanism is controlled by the Z axis servo motor. A precise vee-block slider is designed to provide vertical movement and concentric spindle rotation. The tilt belt is designed to raise the electrode spindle when rotating, the top end of the electrode spindle can be confined by the balance lever. Spindle rotation is driven by an O-ring pulley from the spindle motor; the O-ring also helps to confine the spindle head on the vee-block. Thus, the electrode is fixed in a very precise position. The spindle can rotate up to 11,975 rpm, but it normally works at 1,600 - 2,000 rpm.

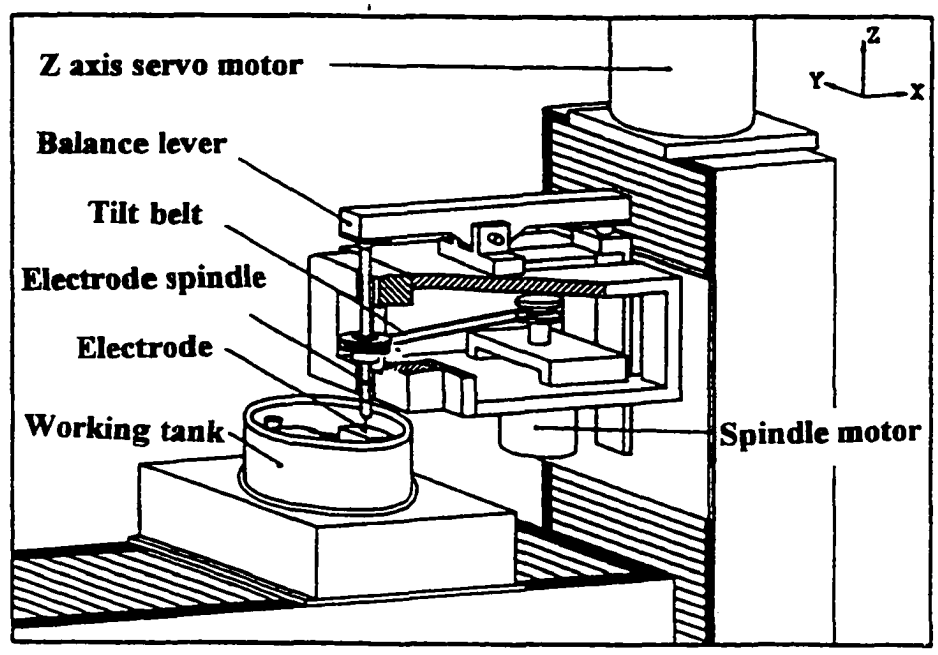

Figure 28. The spindle head mechanism[29].

(2) RC circuit

The RC circuit for the micro-EDM machine is simpler than the conventional EDM machine. Figure 29 shows a typical circuit for the micro-EDM machine. The double-pole

double-throw switch is used to change polarities for either machining workpieces or shaping the electrodes. The RC circuit uses a constant resistance (200Ω) and two adjustable capacitors (one for coarse work C =1,000 - 3,000 PF and the other one for fine work C= 0 - 200 PF). The RC circuit provides high pulse current (Ip), short duration periodic discharge current, and high current density. It is suitable for small area machining, such as hole machining or small-tool making. Electrical discharges start at a voltage (E) larger than 70 V and must have a discharge gap existing between the electrode and the workpiece. The discharge gap is measured by applying a real-time voltage in the EDM work; this real-time voltage is essential to keep a constant distance for stable discharging of the micro-EDM machine. The real-time voltage (V_R) is always kept smaller than 4.0 V. If the gap is too small (less than 1-2 μm) it is close to a "short," and the discharge current then exhibits instabilities.

A servo stage control is used to prevent instability, i.e., to keep the appropriate gap and to result in a stable discharge for the EDM work. A personal computer (PC) has a compared voltage (Vc), and when V_R is larger than Vc, the PC either stops the feedrate of the electrode or returns the electrode to the initial position. By using the PC servo control, the discharge gap can be kept constant, and the discharge current can be kept stable.

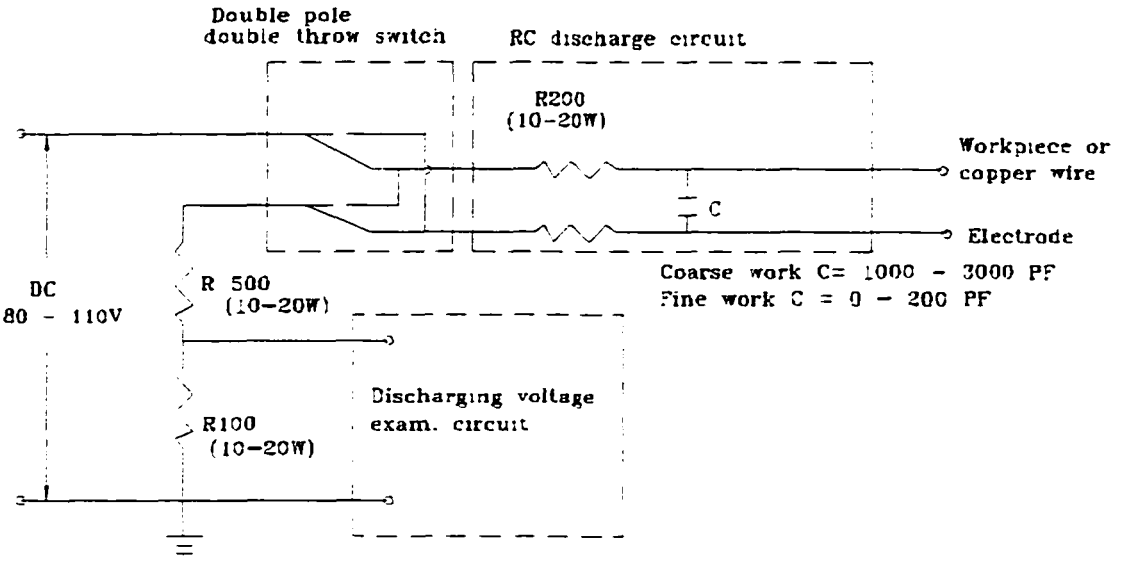

Figure 29. RC circuit diagram of the micro-EDM machine.

(3) WEDG mechanism

WEDG (Wire Electrical Discharge Grinding) has to be a part of a micro-EDM system. WEDG can shape electrodes to accurate dimensions without changing the rotational center of the electrode. Figure 30 shows the WEDG mechanism. The spindle with the electrode has to be fixed before starting the machining. The spindle is setting in a vee-block slider and driven by an O ring pulley. The electrical circuit of the WEDG is the same as the micro-EDM except for reverse polarity. The electrode is connected positive, and the travelling brass wire is negative. The properties of brass wire (Cu63/Zn37) are typically: tensile strength 25-30 Kg/mm^2, electrical conductivity rate 100%, and elongation 20-40%. The brass wire is released by a wire-release mechanism and controlled by a wire guide and is then fed to a receiving mechanism. Two DC motors control both release and receiving mechanisms. The brass wire is kept at constant tensile strength resulting in a stable discharge. According to experimental results, when the receiving motor is run

slowly (about 1 RPM) the result is a high accuracy of wire movement. The linear speed of the brass wire is about 0-60 mm/min; it can be varied with discharge energy. A constant wire feedrate also keeps a stable discharge current. The continuous wire feed provides a new surface and the same diameter during the discharge. Both electrode and brass wire are worn in the WEDG process, and a new surface and constant diameter contributes to a high accuracy in the dimensions of the workpiece, which itself is an electrode for further EDM machining.

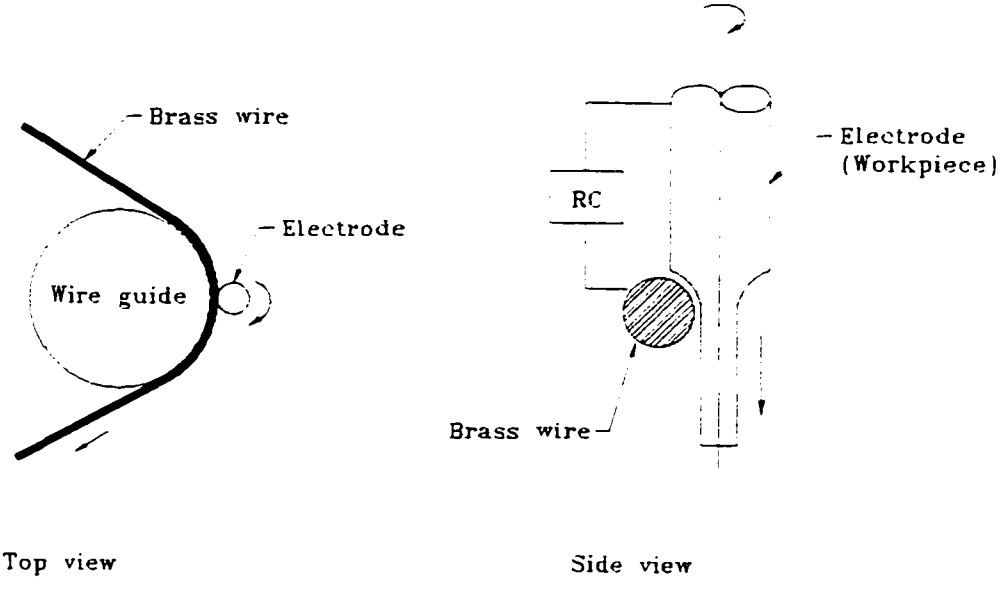

Figure 30. The WEDG mechanism.

(4) Cooling system

The cooling system is a simple mechanism to decrease surface temperature of the workpiece and electrode. The local surface temperature at the arc can be up to 7000 - 9000 °C in EDM. Two types of fluids commonly used are DI water and dielectric fluid. Both fluids have their advantages and depend on work materials. For example, using DI

water on stainless steel results in a more stable discharge than using a dielectric fluid. On the other hand, machining Ta requires a dielectric fluid to get a stable discharge.

4.4.2 Machining methods

The technique for making a series of holes with the same dimensions is illustrated in Figure 31. Different feed depths were used for different holes. The increased depth on successive holes compensated for electrode wear. The electrode (Tungsten Carbide) was ground to 115 μm diameter by the WEDG mechanism. Two steps included were coarse machining and fine finish. Coarse machining used the tip of the electrode as a leading tool to make a rough hole profile. The fine finish used a continuous feed of electrode as a new machining surface. Thus, twelve consecutive holes could be controlled to the same dimension.

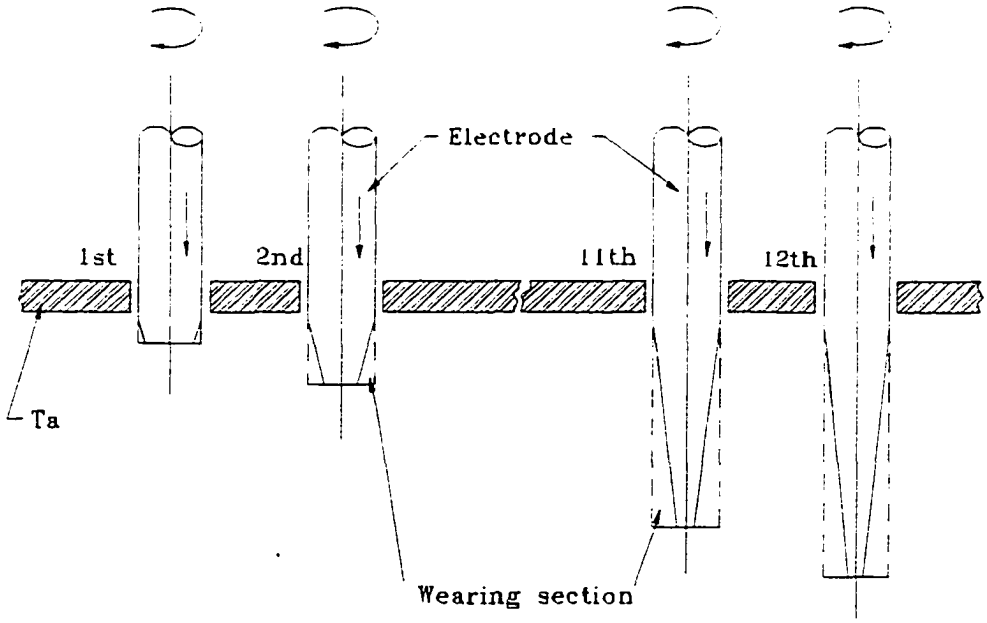

Figure 31. The increased depth on successive holes compensates for electrode wear to make the same diameter hole on a Ta foil.

4.4.3 Results from EDM masks

Figure 32 shows SEM micrographs of a Ta mask (30 μm thick) machined by the micro-EDM machine; Fig.32(a) shows a series of holes on Ta mask and Fig.32(b) is an individual hole profile. The Ta mask was the first trial by the micro-EDM machine. There were only twelve holes on the Ta mask without any surrounding frame. The W mask as illustrated in Figure 26 was the final result (the pattern is same as the optical fiber ferrule mold) from the micro-EDM work. The dimensions of holes are close to the design as determined by the Optimas microscopy measurement. The results of hole dimensions for both Ta and W masks are shown in Table 3. The data shown in Table 3 were using area equivalent diameter method to calculate the hole diameters. The measuring technique will be discussed in Chapter 8.

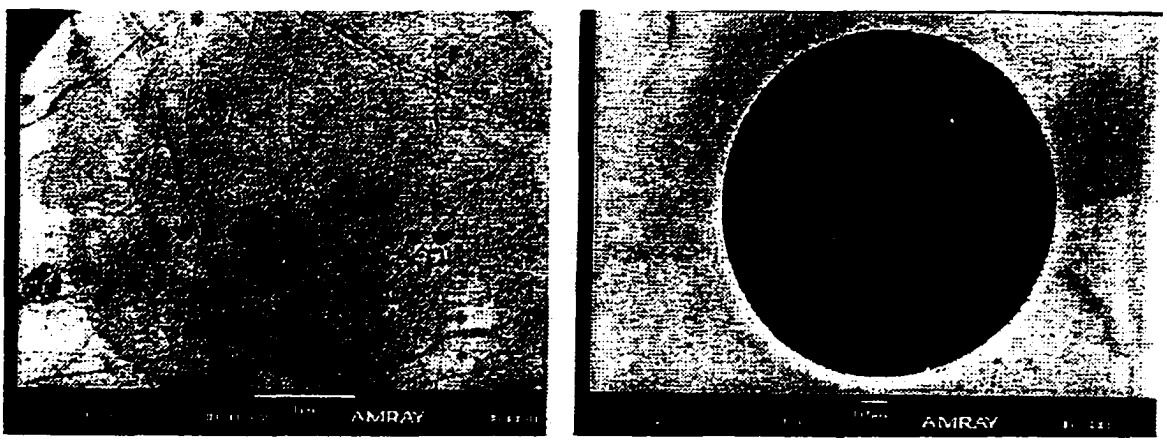

(a) (b)

Figure 32. Micro-EDM machined Ta X-ray mask: (a) a series of holes on a Ta mask, scale bar = 1 mm, (b) a single hole profile, scale bar = 10 μm.

Table 3. The results of hole measurement for Ta and W masks.

Hole	1	3	6	9	12
Ta mask	124.66	124.81	125.25	125.28	125.52
W mask	130.3	129.1	129.5	131.5	131.8

Pitch distance between two holes are varied about +/- 1 μm for the Ta mask and +/- 2 μm for the W mask. The EDM results could therefore not produce the high accuracy requirement on hole diameter and pitch distance required for this project. Two reasons explain why the micro-EDM could not accomplish the task. One is the stage control accuracy of the micro-EDM machine: the stage control accuracy is about 2 μm although it has 0.5 μm resolution. The second reason is the machining accuracy from the EDM work. Figure 33 shows the wall surface of the Ta mask. The side view on the wall surface shows the burrs and grains after the EDM machining. These irregularities in the mask walls are about 2 μm as shown in the SEM micrograph. So far, there is no research reported about the accuracy of the EDM machining in submicron range. No further information of the accuracy of the EDM machining can be provided.

Figure 33. Side view on the wall surface of the Ta mask.

4.5 Conclusion

Three mask-making methods generally can be used for the LIGA process to produce a working mask. The mechanically machined mask method is the simplest and fastest among three methods, but it has geometry limitations, material hardness restrictions, and dimensional bias. The micro-EDM machining mask method has the possibility to achieve the accuracy requirement for this project. If the stage control can be improved and the machining accuracy can be enhanced, this technique is more convenient and cheaper than using an E-beam to write a mask. The E-beam written mask is the best method now available to accomplish the dimensional requirements of the optical fiber ferrule mask. The results of Cr mask written by the E-beam machine shows that the dimensional bias of hole diameters are less than 0.5 μm as determined by the Optimas microscopy.

The stringency of the optical fiber ferrule mold really limits the mask-making method to using the E-beam written mask. There are still many opportunities to use micro-EDM machining and mechanically machined mask methods for products and components if they do not have such rigid specifications. They can be used as inexpensive alternatives to E-beam masks.

CHAPTER 5

DEEP X-RAY LITHOGRAPHY

5.1 Overview

Once the working mask is complete, the next step is to pattern high aspect ratio resist structures. Figure 34 shows a schematic of DXRL to pattern resist structures. Four tasks are involved: seed layer deposition, resist preparation, exposure, and development.

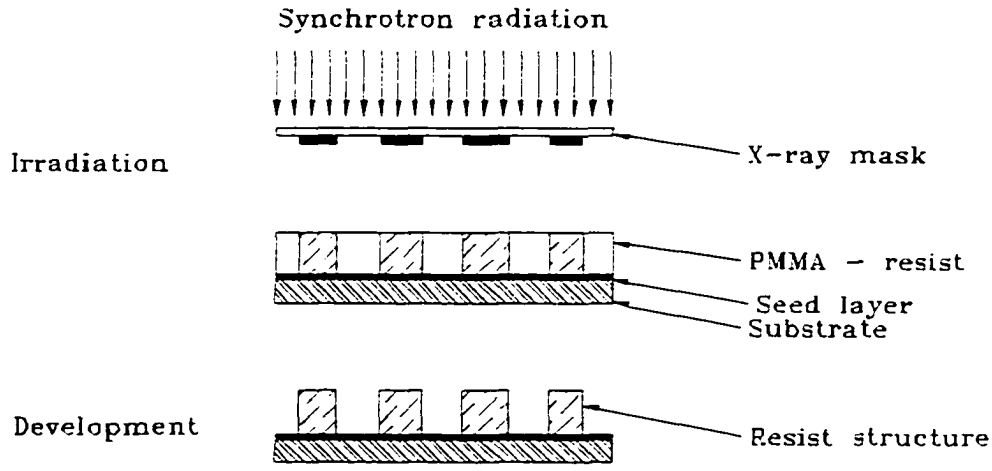

Figure 34. Deep X-ray lithography to pattern resist structure.

5.2 Seed Layer Deposition

The seed layer has to be sputtered before resist bonding because it is a conductive layer placed underneath the resist. A DC magnetron sputtering system, the Unifilm

Technologies PVD300, was used for seed layer deposition. This system has PC control programs to control the motion routine for different size substrates. The desired thickness can be chosen from the menu of the control program. In practice, the deposited thickness is not same as the desired setting thickness. A thickness for sputtering a copper film was set to 2.8 μm, but the result was 1.4 μm thick as shown in Figure 35. The operational parameters are shown in Table 4. The deposition rate for the sputtering machine is not a linear function of deposition time. Obviously, the computer simulation for the film thickness has a difference between theory and reality. We therefore rely on experimental methods to measure the deposited film thickness. In this project, the uniform deposited film for a conductive layer is more important than thickness precision. The bonding structure is shown in Figure 36. PMMA is adhered onto the deposited seed layer film. Chromium, gold, and copper are sputter-deposited on the wafer as the seed layer. The operating parameters and thicknesses of each layer are shown in Table 5.

Table 4. Operating parameters for sputtering copper films.

Parameters	Number
Setting thickness	2.8 μm
Deposition rate	100 nm/min
Deposit time	170 min
Current	0.12 Amp

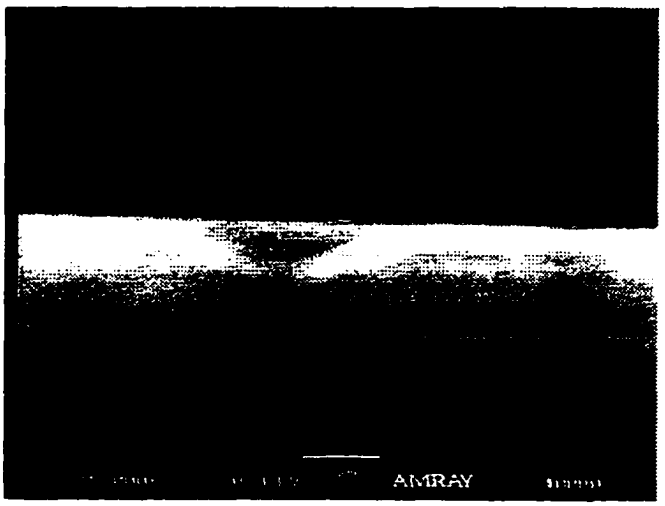

Figure 35. SEM micrograph of a sputtered copper film on a Si wafer, scale bar = 1 μm.

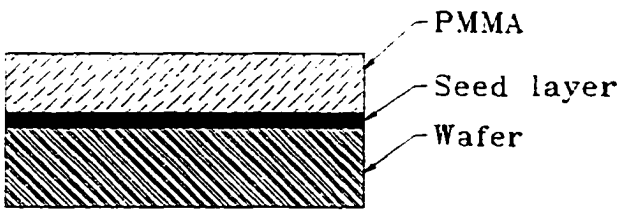

Figure 36. The bonding structure in substrate preparation.

Table 5. The operating parameters for the seed layer in this project.

Mode	Thickness	Rate	Time	Amps	Volts
Cr S4-3-A	20 Å	65 Å/min	1.92 min	0.05 A	162 V
Au S4-3-A	250Å	600 Å/min	2.24 min	0.05 A	182 V
Cu S4-3-A	2500Å	1000 Å/min	15.24 min	0.075 A	198 V

5.3 Resist Preparation

5.3.1 Resist bonding

The ferrule mold thickness required is 1 mm; therefore, 1 mm thick resist has to be deposited onto the substrate. Three typical methods used to deposit different thick films as shown in Table 6 are spin coating, casting, and adhesive bonding. Thin films (thickness less than 100 μm) are deposited by spin coating. Thickness can be controlled by spin speed, time, and resist solvent concentration. Thicker films require the casting method which can achieve resist thicknesses of several hundred microns. The bonding method employs commercially available thick PMMA film (e. g. 500 μm and 1.0 mm). A 3-4% PMMA solution is first spun on the surface of the substrate to get a thin film layer of 0.5-0.7 μm. The next step is to cure the spun-on PMMA at 110 °C on a hot plate for 30 minutes. MMA (methyl methacrylate) is then applied as an adhesive between the PMMA sheet and the substrate, followed by a weight to press them. The PMMA sheet is bonded on the top of the substrate, and the substrate is sputtered a seed layer. The bonded resist structure is shown in Figure 37.

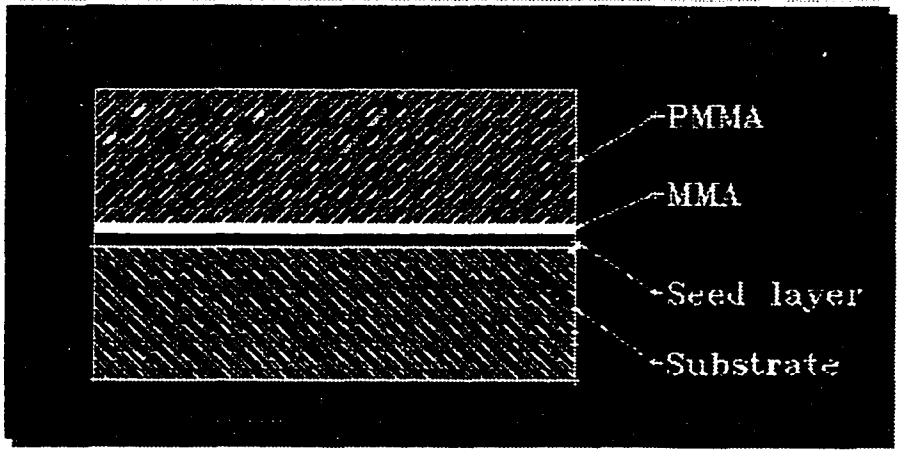

Figure 37. The bonded resist structure.

Table 6. Resist film application methods.

Film thickness (μm)	Application method
< 100	Spin coating
100 – 500	Casting or sheet bonding followed by diamond turning
>500	Adhesive bonding

5.3.2 Diamond turning

PMMA sheets from the commercial supplier are either 500 or 1,000 μm. The Optimum Ultra-Precision Machining System from PRECITECH Inc. was used to cut bonded PMMA to different thickness. The work-holding spindle is mounted on the X axis stage, perpendicular to the cutting tool on the Z axis stage as shown in Figure 38. Both X and Z slides are fully constrained, hydrostatic oil bearing designed, and driven by precision preload ball screws as well as integral brush type DC servo motored tachometer combination.

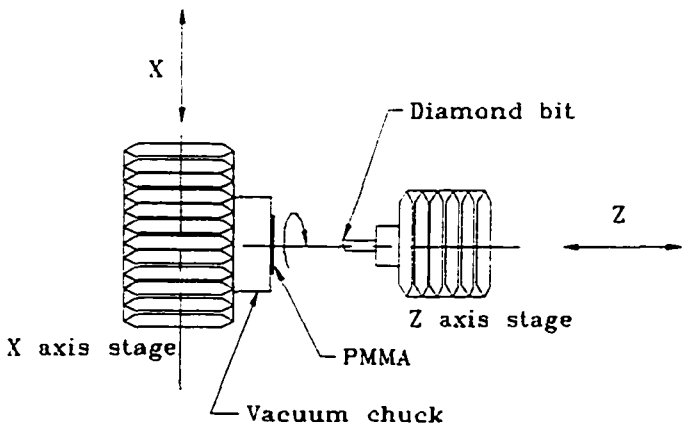

Figure 38. A schematic of the diamond turning mechanism.

The diamond turning machine can cut PMMA with thickness accuracy +/- 5 μm. The 1 mm thick PMMA sheet was bonded on the substrate; then it was cut to the desired thickness. The cutting thickness range was from 100 to 900 μm. The cutting parameters used in the diamond machining of the PMMA sheets are

- Initial cuts -- 1750 rpm, 100 um depth of cut, 37.5 mm/min
- Finishing cut -- 2500 rpm, 2 um depth of cut, 5 mm/min

Also, the surface roughness of the PMMA measured by the RST machine is Rt = 0.924 μm.

5.4 X-ray Source

The synchrotron radiation is continuous, intense, highly collimated, and bright light covering the spectrum from infrared through X-rays. CAMD operates at two major electron energies (1.3 and 1.5 GeV) with a maximum ring current after injection of 220 and 150 mA respectively. Figure 39 shows a simple schematic of the IfM beam line setup at CAMD. The X-ray beam starts at the bending magnet and travels to the exposure chamber through a vacuum. It then enters the exposure chamber with scanner through an X-ray transparent Be window. The angular divergence of synchrotron radiation is 0.1 mrad/mm horizontal, ±0.5 mrad vertical over the entire field. The beam line is about 10 m long from source to scanner.

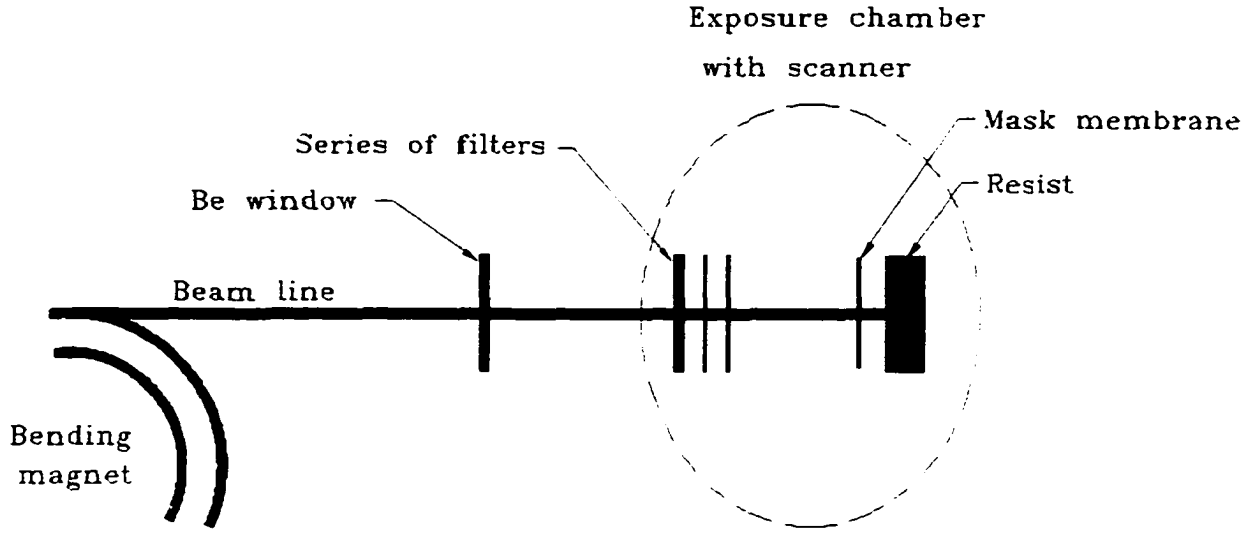

Figure 39. Schematic of the beam line setup.

The exposure chamber with scanner was designed by the JENOPTIK Technologies GmbH, Germany. It is equipped with a microstepper-driven multi-axis scanning mechanism to provide desired orientation of a sample during exposure. A vertical linear positioner with 1.5 μm resolution is used to perform scanning a sample through the X-ray beam. Computer-controlled user interface allows coordinated velocity and motion profiles of all axes. Uniform exposure in the field is accomplished by vertical motion of the mask with resist carrier fixture relative to the stationary X-ray beam. The workstage speed can be set to any value from 1 to 50 mm/sec. The orthogonality accuracy to the synchrotron beam center is within 0.1 mrad.

5.5 Absorbed Radiation Dose Requirements

PMMA typically has an average molecular weight of 600,000. The radiation dose acts to reduce the molecular weight of PMMA to about 20,000[29]. Figure 40(a) presents a typical molecular weight distribution of PMMA before the irradiation. The developer can dissolve the PMMA up to a molecular weight of about 20,000 as shown the hatched area. At a radiation dose of 4 kJ/cm^3, an average molecular weight 5,700 is achieved with the distribution shown in Figure 40(b). It can be assumed from the figure that the irradiated PMMA is dissolved in the developer at this dose. At a radiation dose below 4 kJ/cm^3 , the molecular weight cannot be reduced sufficiently. The irradiated areas are not dissolved completely, exposed PMMA partially remains in the structures. Thus, 4 kJ/cm^3 is the lower limit of the dose.

The distribution of 20 kJ/cm3 radiation dose is shown in Figure 40(c). The average molecular weight is about 2,800. The entire exposed PMMA is dissolved relatively quickly in the developer. However, this result does not mean that higher dose is always good. The PMMA can be damaged by forming blisters that cause defect in structures. Thus, 20 kJ/cm3 corresponds to the upper limit of dose for PMMA. Table 7 is a summary of exposure parameters for PMMA.

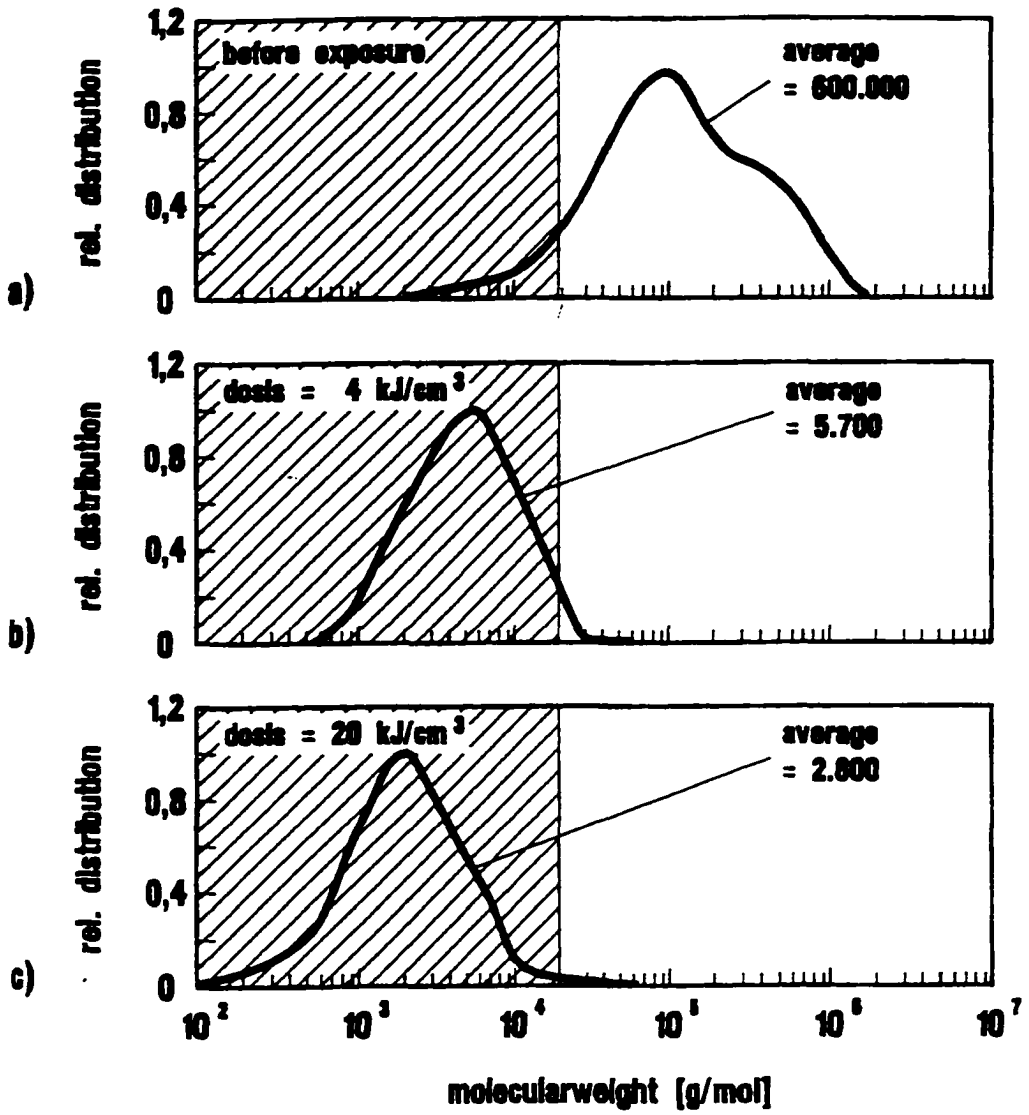

Figure 40. PMMA molecular weight with its relative distribution when exposed to synchrotron radiation[29].

Table 7. Parameters for DXRL exposure in PMMA resist, using the GG developer at 36°C.

Parameter	Value	Remark
Dt (Dose deposited at the top of the PMMA layer)	≤20 kJ/cm^3	Higher dose deposition causes blisters on microstructures
Db (Dose deposited at the bottom of the resist layer)	≥ 4 kJ/cm^3	This value has to be adapted to the resist thickness; for thin resist layer (e.g. 20~30 μm) 3 kJ/cm^3 may be sufficient while thicker layer (above 500 μm) may require a higher value.
Dt/Db (Ratio of top to bottom dose)	≤5	For thin resist layer, this value may be higher while for thick layers it may become smaller (increasing Db and decrease Dt)
Dc (Critical dose, maximum dose allowed at the top of the resist underneath the absorber structures.	≤100 J/cm^3	This value is relevant if high quality microstructures are demanded; also depending of the development conditions, this value can be extended to 150 J/cm^3.

5.6 Exposure Simulation

The synchrotron radiation at CAMD is used to transfer the connector patterns from the working mask into a PMMA layer. Since the resist layer with 1.0 mm thick is to be exposed, the optimum critical wavelength of the synchrotron radiation source is approximately 0.2 nm, requiring exposure on the white light beam line. The exposure time is calculated by the TRANSMIT software which is an Excel-based program designed especially for DXRL.The emitted power I_o (λ) of the synchrotron source at the wavelength, λ, is attenuated by various elements inserted in the beam line. The attenuation is in a series relation as shown in Figure 39. The attenuation can be calculated from Lambert Beer's law[30] taking into account the material interaction with the radiation described by the absorption coefficient:

$$I_1(\lambda) = I_O(\lambda) \cdot e^{-\mu_i(\lambda) d_j} \tag{5.1}$$

$I_i(\lambda)$ is the transmitted intensity at wavelength λ.

$I_o(\lambda)$ is the emitted intensity of source at wavelength λ.

$\mu_i(\lambda)$ is the linear absorption coefficient of i-th absorber.

d_j is the thickness of i-th absorber.

The absorption of energy in the resist is also defined by the absorption coefficient. The absorption of the resist itself cannot be neglected in calculating the absorbed dose in a depth Z of the resist layer especially for thick resist layers. Therefore, exposing a resist characterized by its absorption coefficient $\mu_{resist}(\lambda)$ with a light source emitting a power (P) on the resist area (A) underneath an absorber of thickness (d_j) in a time (t), the absorbed dose in the depth (z) is given by Equation (5.2) according to Goettert[30].

$$D(z, d_i) = \mu_{resist}(\lambda) \cdot e^{-\mu resist(\lambda) \cdot z} \cdot e^{-\mu di} \cdot P/A \cdot t \tag{5.2}$$

The absorption of all components being inserted in front of the resist has to be considered. Doing so the absorbed dose D(z) in the resist can be calculated by the Equation (5.3).

$$D(z)[J/cm^3] = 1.421 \cdot 10^{-16} \cdot (\frac{E}{Eo})^7 r_o^{-2}[m] \cdot R^{-1}[m] \cdot \frac{DA[As]}{H[mm]} \cdot \int_{\lambda min}^{\lambda max} G_3 \ (\frac{\lambda_c}{\lambda}) \cdot \mu_{resist}(\lambda) \cdot e^{-\mu resist(\lambda) \cdot z} \cdot e^{-\sum_i \mu_i(\lambda) di} \cdot \lambda[nm] \tag{5.3}$$

D(z) is the absorbed dose [J/cm^3] in depth z.

E is the electron energy [GeV].

$E_o = 0.511 * 10^{-3}$ [GeV]

$r_o = 2.928$ [m] radius of curvature at CAMD.

R = 10 [m] distance source to scanner.

DA is the dose amount I [A] * t [s] = product of electron current at CAMD * exposure time.

H is the vertical scanning height [default 1 cm].

G_3 is the universal spectral distribution function (defined by modified Bessel functions).

λc is the characteristic wavelength of the source.

$\mu i(\lambda)$ [1/cm] is the linear absorption of i-th absorber material.

Di is the thickness of i-th absorber.

The integral over the wavelength takes into account the source properties while the material parameters of all elements inserted in the beam line are represented by their linear absorption coefficients. The resist coefficient is calculated from the individual mass absorption coefficient of each atom forming the resist taking into account the number of atoms per unit cell as well as the resist density. Equation (5.4) shows the absorption coefficient calculation[30].

$$\mu_{resist}(\lambda)[1/cm] = \frac{\sum_k g_k \cdot \mu_k(\lambda)[cm^2/g]}{\sum_k g_k} \rho_{resist}[g/cm^3] \qquad (5.4)$$

where $g_k = n_k * A_k$

n_k is the number of k-th atom species of the monomer unit.

A_k is the atomic weight of k-th atom.

$\mu_k(\lambda)$ [cm^2/g] is mass absorption coefficient of i-th absorber material.

According the equations above, a simulation program (TRANSMIT) is available for user to easy calculate the exposure parameters. TRANSMIT is an EXCEL-based program designed for DXRL, developed at the University of Wisconsin at Madison. The following procedure describes each step to simulate exposure parameters. The simulation result can be seen in Appendix I.

1st step: Input the source parameters

Source parameters include electron energy, 1.3 GeV, with the ring current 100 mA, radius of curvature 2.928 m, beam horizontal acceptance angle 1 mrad, minimum photon energy 100 eV, maximum photon energy 16,100 eV, and number of calculation steps. The emitted white light from a bending magnet at CAMD has a characteristic wavelength of 7.45 Å at 1.3 GeV. The corresponding characteristic wavelength can be calculated using Equation (5.5).

$$\lambda_c[A] = 5.59 \cdot \frac{R[m]}{E^3[GeV]} \tag{5.5}$$

2nd step: Insert filters

The input parameters include filter material, element density, and material thickness. Add filters in a series as the beam line is set up, e.g. Be window, aluminum filter, mask membrane, and resist. Dose calculations are based on the filter layout.

3rd step: Input the minimum dose and scanning distance

The amount of dose on both top and bottom is in terms of mA-min. The ratio of bottom to top can be found from the final result. As mentioned on the requirement of absorbed radiation, the ratio should be kept below 5. If the ratio is above 5, repeat the 2nd step to adjust source and filters to meet the required ratio.

5.7 Exposure Results

Latent images of exposed samples are shown in Figure 41. A good exposed sample is illustrated in Figure 41(a). The area inside the circle is unexposed area, and the area outside the circle is exposed area. There is no obvious difference between exposed and unexposed area. The surface of the field is homogenous and clean (the spot on the photograph are dust particles on the Nikon microscope lens). The ratio of top to bottom dose is 4.19, which meets the exposure requirements. Figure 41(b) is an illustration of blisters formed due to a high ratio (6.7) of top to bottom dose.

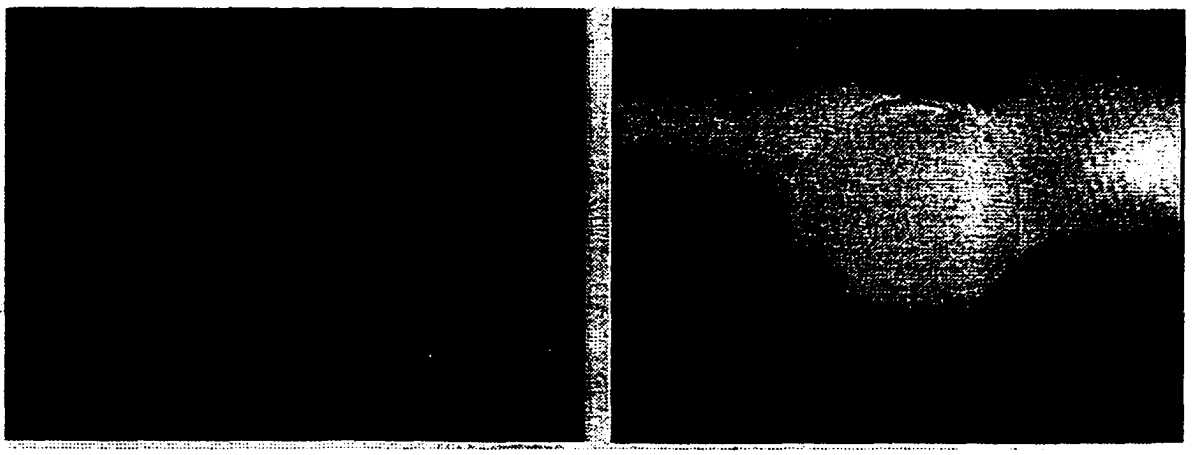

(a) (b)

Figure 41. Comparison of exposure results at two different dose ratios of top to bottom; (a) is at ratio 4.19 which is a good exposure and (b) is at ratio 6.7 which has blisters as shown the dark portion.

5.8 Development

The irradiated resist is dissolved in a solvent (developer) resulting in the resist structure which exhibits the negative form of the mask pattern. The developer (known as G.G. solution) for PMMA is 60 vol.% 2-(2-butoxyethoxy)ethanol, 20 vol.% tetrahydro-1, 4-oxazin (morpholine), 5 vol.% 2-aminoethanol, 15 vol.% water. Typically, it is operated at 36°C in a recirculating developing system[29]. Figure 42 is a schematic of the developer setup. The sample is sitting horizontally on a wafer rack and face down in the developer. In the early work, nonuniform development of the resist was found with vertical placement. The temperature probe on the hot plate can control the bath temperature with the accuracy with +/- 2 °C.

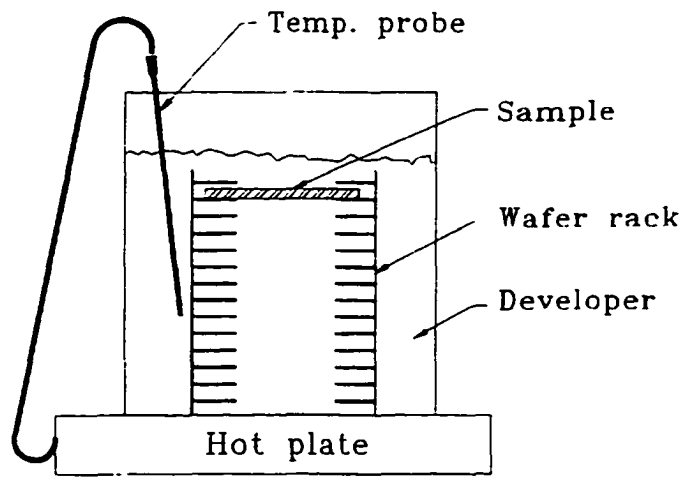

Figure 42. A schematic of the developer setup.

A flowchart to illustrate the development of exposed PMMA is shown in Figure 44. The exposed sample is first immersed into the B.D.G. solution (60 vol.% 2-(2-butoxyethoxy) ethanol and 40 vol.% DI water) for 20 minutes at a temperature setting of 30 °C. Then, the sample is immersed into the G.G. solution after B.D.G. solution until the substrate shows clearing; then it is re-immersed the sample into the B.D.G. solution rinse for 20 minutes to stabilize resist structures. Finally, a DI water rinse is used for 3 minutes to wash residuals. Vacuum drying removed the water from the surface of the sample. Heat drying was not used to prevent thermal distortion of the PMMA structure, nor nitrogen blasting used to avoid the possibility of losing the resist posts. No circulation is needed for this project. The circular flow could cause the isolated resist posts to peel off the substrate during the development. No post on the substrate means that there is no channel on the ferrule mold after electroforming. First rinse in B.D.G. solution is used to prevent resist posts from peeling away from the substrate; this is different from the standard developing procedure.

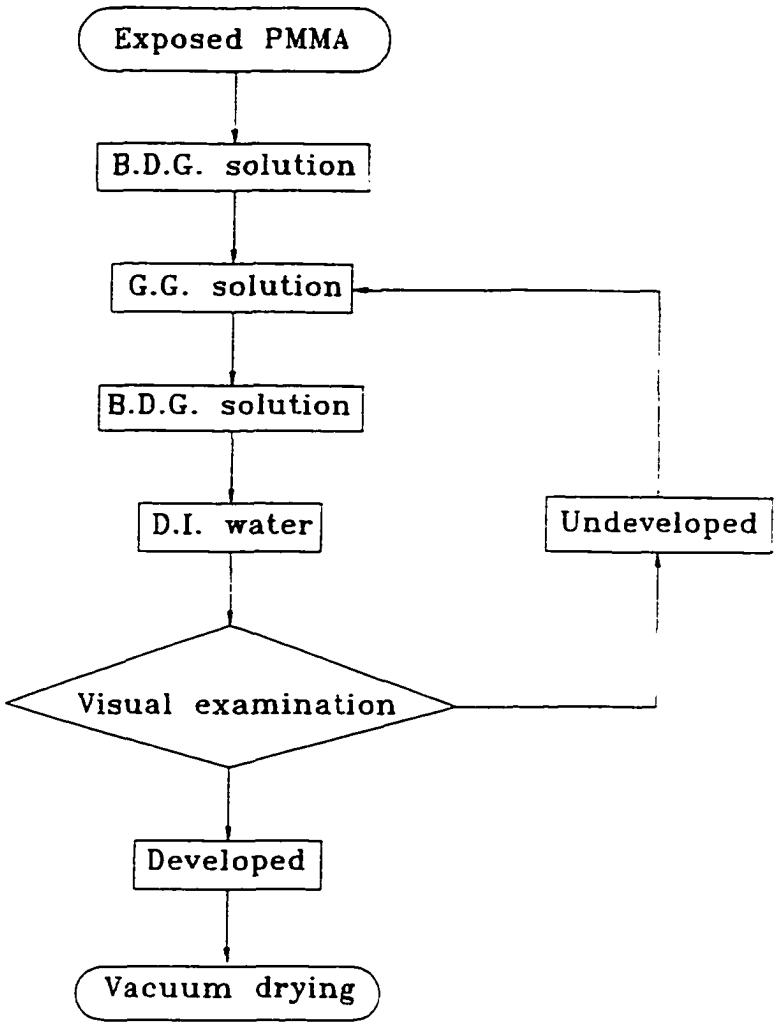

Figure 43. The developing procedure for exposed PMMA

The developing time depends on irradiated resist thickness and developer temperature when the samples have the required exposure radiation dose. The developing temperature is an important factor. Developing PMMA (300 μm thick) at different temperatures resulted in different developing times as shown in Figure 44: the higher

temperature has a shorter developing time. Exposed PMMA developed at room temperature has residues on the substrate, and long developing time (more than 3 hours) still does not clear the residues and causes the loss of resist posts on the ferrule pattern.

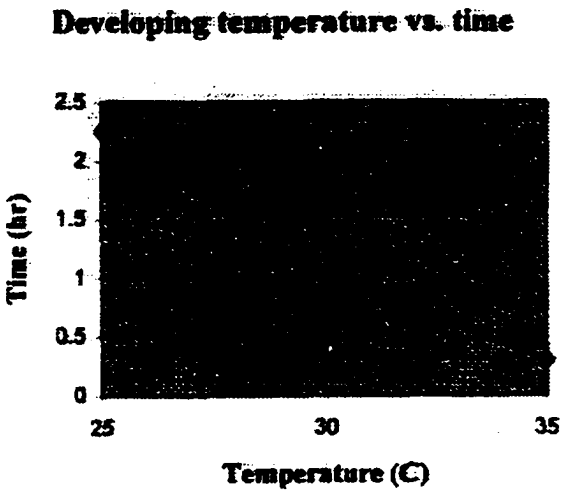

Figure 44. The relationship of developing temperature versus developing time for 300 μm thick resist.

The developing time as a function of the resist thickness at 36°C was described by Liu[31] in his thesis which provides the general idea for developing times. In practice, visual examination is required during the development of resist. If the exposed area is not well developed, then the procedure is repeated until the sample is developed. The exposed area can be seen gradually emerging from the substrate, since the surface color gets brighter and residuals are dissolving. A smooth surface can be seen on the exposed area. The exposed results are illustrated in Figure 45. Figure 45(a) is the resist post photo pictured from a Nikon microscope after development. A clear contrast is shown on edge of the post. Figure 45(b) is the resist mold for making a nickel post: it is exposed

from the intermediate mask. The inside circle is empty after development. The edge is in a round profile as same as the drawing circle. Again, those spots on both photographs are dust particles on the Nikon microscope lens. Samples do not have spots on their surfaces in reality.

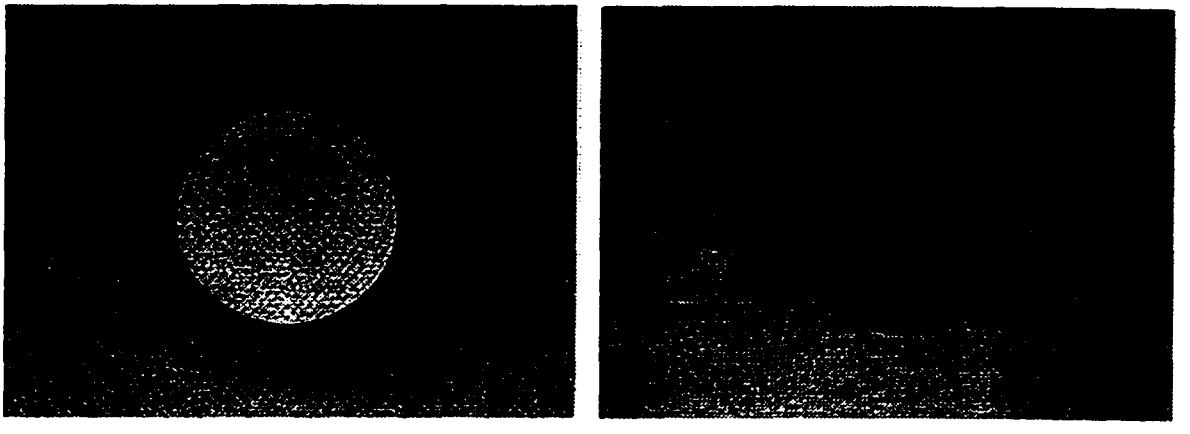

(a) (b)

Figure 45. Micrographs of resist patterns: (a) a resist mold exposed from the intermediate mask and (b) a resist post exposed from the working mask.

CHAPTER 6

NICKEL ELECTROFORMING

6.1 Conventional Nickel Electroplating

6.1.1 Fundamentals of nickel electroplating

Nickel electroplating is used to deposit a layer of nickel onto a substrate. The process involves the dissolution of one electrode (the anode) and the deposition of metallic nickel on the other electrode (the cathode)[20]. A current is applied between the anode (positive) and the cathode(negative) through an aqueous solution of nickel salts (electrolyte).

Nickel electrolyte contains positive charged ions (Ni^{2+}) which come from dissolving nickel salts. During the electroplating process, the anode replenishes the nickel ions into the electrolyte. Thus, the nickel electroplating process can be operated continuously for a long period of time. The electrochemical reaction is shown in the following chemical form:

$$Ni^{2+} + 2e^{-} \Leftrightarrow Ni^{0} \qquad (6.1)$$

When current flows, divalent nickel ions (Ni^{2+}) react with two electrons ($2e^{-}$) and form metallic nickel (Ni^{0}) on the cathode. At the same time, the reverse occurs at the anode where metallic nickel dissolves and discharges divalent ions into the solution.

A simplified electroplating system is illustrated in Figure 46. The power source

provides the required electrical energy for the electrochemical reaction between the anode and cathode. The current can be direct current (DC), pulse-DC, or pulsed periodic reverse (PPR) current. Different current densities will effect on the properties of the deposition metals, such as hardness, grain size, and surface morphology [32].

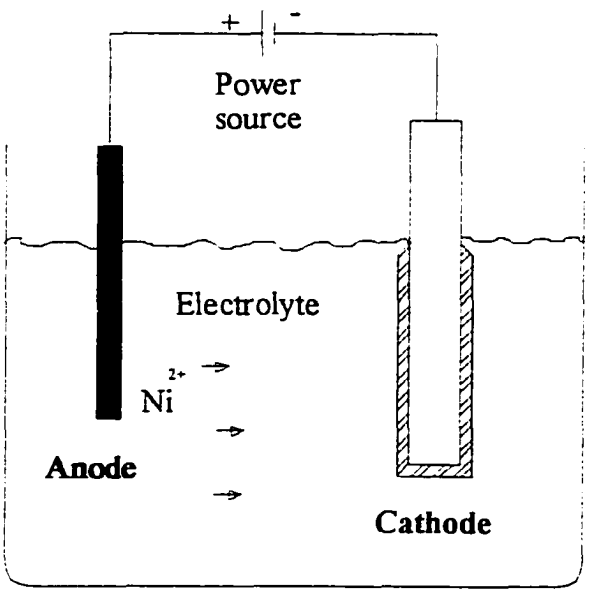

Figure 46. Schematic of a simplified electroplating system.

6.1.2 Deposition theory

The deposition process involves localized electrochemical deposition. An ion must reach the electrode/solution interface, receive electrons to become an atom, and then join other atoms to form a crystal. A potential difference must be applied between the anode and cathode. In a plating operation, four processes operate to supply metal ions to the depleted solution at the cathode, and to transfer them from the enriched electrolyte at the anode.

First, electron transfer is considered as the direct factor. At equilibrium, a balance between chemical and electrical potential occurs at the electrode/solution interface

manifesting itself as an ~1 to 30 nm thick charged region known as the double layer[32]. The electrochemical reactions are field-dependent heterogeneous processes, an important factor determining their rates will be the local concentration of reacting and other particles at the charge surface. The simplest model of the distribution of ions at interfaces was proposed by Helmoltz, who regarded the behavior of the "double-layer" of charges on the surface[33]. To effect an electron transfer, an activation energy is required for an ion or molecule to rid itself of solvating molecules, travel through the double layer, and adjust its hydration sphere for electron transfer. The surface is regarded as one of the plates of a condenser. At the electrical potential used in electroplating, electron transfer rates generally dominate other factors nearby electrode surface region.

Second, diffusion causes ions to move from the unchanged bulk of the electrolyte to the impoverished region at the cathode according to the Fick's first law of diffusion[34] (Equation 6.2). The metal ion concentration in the double layer is different than the bulk solution as shown in Figure 47. There are concentration gradients existing on both cathode and anode surface.

$$\frac{dQ}{dt} = D\frac{Cb - Cs}{\delta} \tag{6.2}$$

where, dQ/dt is the diffusion rate (mole.m^{-2}.s^{-1})

D is the diffusivity constant (m^2.s^{-1})

δ is the thickness of the double layer (m)

Cb is the metal concentration at the bulk solution (mole.m^{-3})

Cs is the metal ion concentration at the electrode surface (mole.m^{-3})

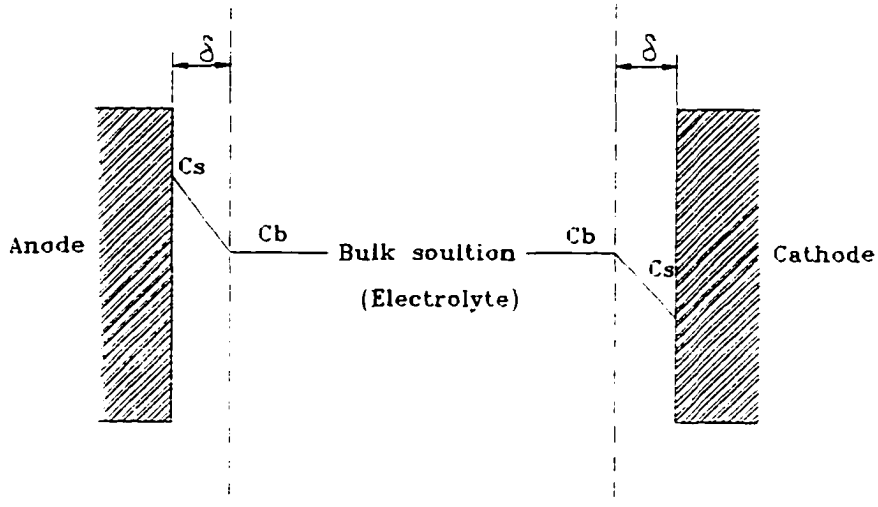

Figure 47. Metal ion concentration in the electrolyte.

Third, electrical migration of cations is superimposed on diffusion (the motion is reversed with an anionic complex). The current, j, due to the migration of charged ions in solution is proportional to the electric field, E, by Ohm's law[32], Equation 6.3.

$$j = \sigma \cdot E \tag{6.3}$$

with

$$\sigma = zuCF \tag{6.4}$$

where σ is the conductivity of electrolyte, z is the ionic charge, u is the ion mobility, C is the ion concentration, and F is one Faraday (9.6485×10^4 C.mole^{-1})

Migration generally plays a secondary role in mass transport to the depleted region because much of the current is carried by ions of species that do not react in deposition.

Fourth, convection currents tend to move the depleted solution away from the cathode and replace it with fresh solution from the unaltered bath. Agitation is often used to force convection, leading to the flow of bulk solution into the depleted layer and increasing deposition rates. In spite of agitation, deposition remains diffusion limited because viscous forces near the electrode surface impede the influx of fluid.

6.2 Nickel Electroforming Setup

Nickel electroforming is used to deposit the nickel into the free space of the resist mold. Nickel sulfamate electrolyte is commonly used for thick electrodeposition due to its high deposition rate and low internal stress of the plated nickel. An electroforming station in the IfM is shown in Figure 48. A 4-liter Pyrex glass beaker is used as an electroforming tank which allows a 4-in substrate inside. The plating bath is heated by a hot plate/stirrer placed beneath the beaker. Agitation is provided by a magnetic stirring bar placed in the beaker and actuated by the hot plate/stirrer. A glass temperature probe from the hot plate/stirrer is placed in the electrolyte to control the bath temperature within ± 1°C. The electrolyte acidity is measured by a portable digital pH meter with resolution 0.1 value. An in-tank circular filtration including filter tube and carbon treatment is used. Polypropylene filter tubes are recommended for the nickel sulfamate electrolyte which has a working pH range 0-14. The filter used in this work has 5-micron pores, which is the finest density tube available from the commercial. To avoid impurity deposits on microstructures, high purity is required in the electroforming process. The carbon-filter tube has 0.5 micron rating (#5) to insure all organic impurities are filtered. The circular flow rate is controlled by the adjust valve at 20 tank volume turnovers per hour. The amount of electrolyte for this electroforming station is 4.0 liters.

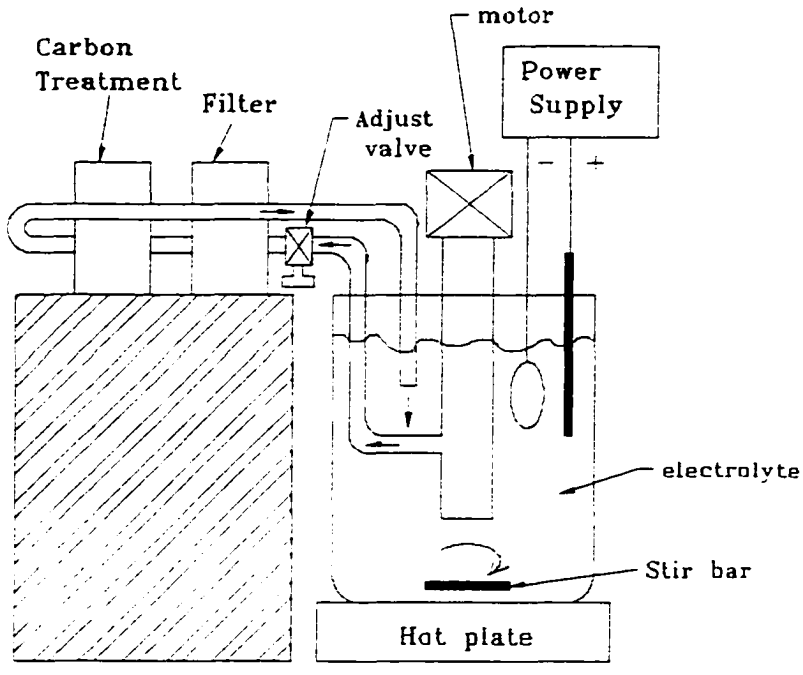

Figure 48. A schematic of the electroforming station.

6.3 Bath Preparation and Operating Conditions

The electrolyte is prepared from concentrated nickel sulfamate purchased from M&T Chemicals Inc. It is diluted with deioned (DI) water using a 1:1 ratio (500 ml per liter). Boric acid is used to buffer the bath pH value within 3.8 ~ 4.2 range. Nickel chloride is added to supplement the depleted nickel ions. Agent Besplate 228 is used to increase hardness, reduce tensile strength, and increase tensile strength of the deposited nickel. AP-M nickel wetter is used to control pits growth on the deposit surface. The electrolyte contents and operating conditions are shown in Table 8 and 9.

Table 8. An operational nickel sulfamate electrolyte.

Chemical	Concentration
Nickel sulfamate concentrate	500 mL/L
Nickel content	90 g/L
Boric acid	30 g/L
Nickel chloride	15 g/L
Stress controller (Besplate 228)	1.0 vol.%
Wetting agent (AP-M nickel wetter)	1.0 vol.%

Table 9. Nickel electroplating operating conditions.

Parameters	Conditions
pH (Acidity)	3.8 ~ 4.2
Temperature	45 °C
Agitation (magnetic bar)	250 RPM
Current density range	0.1 to 90 mA/cm^2

6.4 Growth Rate Calculation

The deposit quantities of electroplated materials were generated from Faraday's law[35]. The mass of electrodeposit is proportional to the quantity of coulombs used as shown in Equation (6.5).

$$\textit{Mass of electrodeposit} \propto \textit{number of coulombs used} \tag{6.5}$$

It can be expressed mathematically as the Equation (6.6).

$$M = \frac{j * T * A}{z * F} \tag{6.6}$$

where M is the mass of electrodeposit, j is the input current, T is the plating time, A is the atomic weight, z is the valence number, and F is one Faraday (9.65×10^4 coulomb per mole)

Rewriting Equation (6.6) as Equation (6.7).

$$M = K * j * T \tag{6.7}$$

The constant K is called the electrochemical equivalent, the unit is *g per A*hr*. The mass of deposition is shown in Equation (6.8).

$$M = \rho * a * t \tag{6.8}$$

Mass is equal to the metal density (ρ) multiple the plating area (a) and thickness (t). Subsitute Equation (6.7) into (6.8) and rewrite as Equation (6.9).

$$\frac{t}{T} = \frac{K\frac{j}{a}}{\rho} \tag{6.9}$$

Rewrite Equation (6.9), the growth rate equation is expressed as Equation (6.10).

$$\eta = \frac{\Theta * K}{\rho} \tag{6.10}$$

where η is the growth rate and Θ is the area current density.

For the nickel plating, $K = 1.095$ *g per A*hr* and $\rho = 8.9$ *g per* cm^3 according to Gramham[36]. To easily to calculate the growth rate, Equation (6.10) can be written as Equation (6.11).

$$\eta = 0.0205 * \Theta \tag{6.11}$$

where η is the rate of deposition in *μm per min*, Θ is the area current density deposition in *mA per* cm^2, and 0.0205 is the conversion constant.

6.5 Electroforming Procedure

Three main control parameters in the electroforming are the electroform thickness, plating current density, and plating time. The relation can be calculated from the Equation (6.11). The deposition thickness is controlled by the plating time and applied current density. The PMMA mold thickness is usually known before electroforming and the deposition thickness is based on this value to decide the electroforming parameters. First, the applied plating current density should be chosen. The plating current density strongly affects the growth rate and deposit properties. The plating current density is directly proportional to the growth rate from Equation (6.9). Second, the plating thickness is based on the current density to calculate the growth rate and plating time.

In practice, electroforming a 500 μm thick nickel mold needs a plating current density of 40 mA/cm^2 for 625 min. (10 hours and 25 min.). Assuming the cathode efficiency is 100%, the growth rate is 0.8 μm/min ($\eta = 0.02 \times 40\ mA/cm^2$). If the plating area is 4.0 cm^2, a plating current 160 mA (40 $mA/cm^2 \times 4.0\ cm^2$) is needed.

6.6 Metal Distribution and Growth Rate

The deposited metal distribution is a concave shape over the whole area of the plating base. The edge thickness of the plating area is usually twice as high as the center of the plating area. Figure 49 is an experimental electrodeposition profile onto the copper base. The sample was 40 mm wide on the plating base and plated at current density 80 mA/cm^2 for 8 hours. The middle location between two sides is the lowest point over the profile as shown in the figure. The plated thickness ratio of practice to theory is approximately 0.6 at the center location.

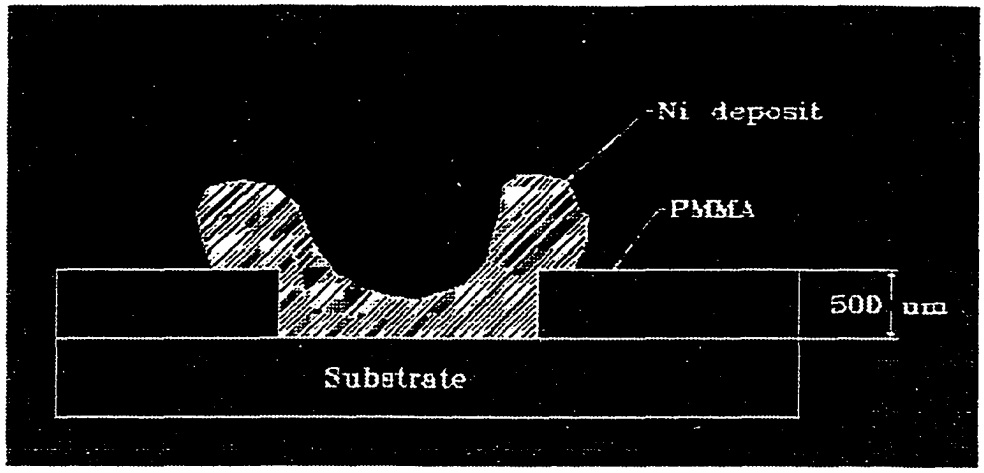

Figure 49. An experimental result showing the deposition profile.

An optical fiber ferrule mold after nickel electroforming is shown in Figure 50. A nonuniform metal distribution was measured. The left side thickness is higher than the right side by about 100 μm. The apparent resist column diameter increases from the left to right side on the micrograph. The apparent small resist column means it is overplated. Figure 51 is a detailed illustration of electroforming around the resist columns as expressed in Figure 50. Figure 51(a) shows the second resist post from the left side which shows the overplated nickel higher than the resist post; that is, it is shaped like a volcano in a close view. Figure 51 (b) shows the first post from right side of Figure 50; the deposited nickel is right on the top of the resist post.

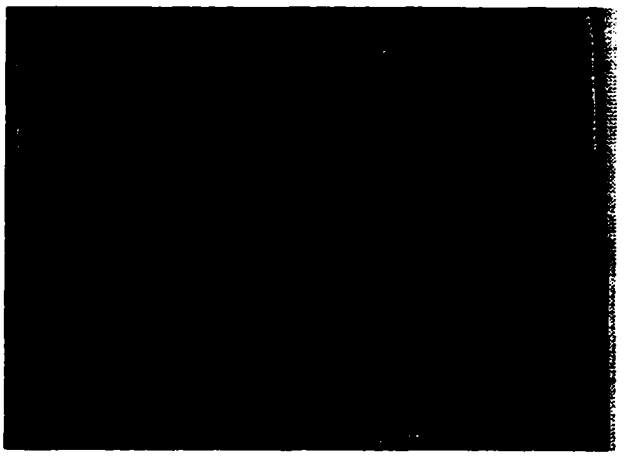

Figure 50. An overview of nonuniform deposit over the ferrule mold.

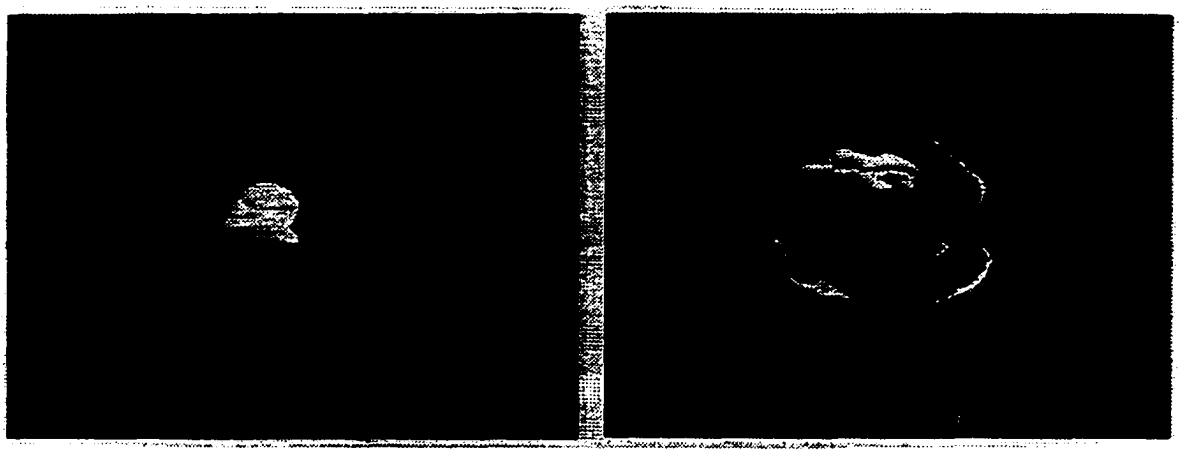

(a) (b)

Figure 51. An illustration of electroforming resist columns: (a) shows a close view of an overplated resist column and (b) shows the nickel deposit just on top of the resist post.

The plating current density dominates the growth rate as shown in Figure 52. The theoretical growth rate is between the edge and center growth rate. In practice, the growth rate should be estimated by using the center growth rate. Otherwise, the final product could have a "lake" or depression inside the sample. The overplated portion at the boundaries of the plated object must be mechanically planarized to yield a uniform thickness.

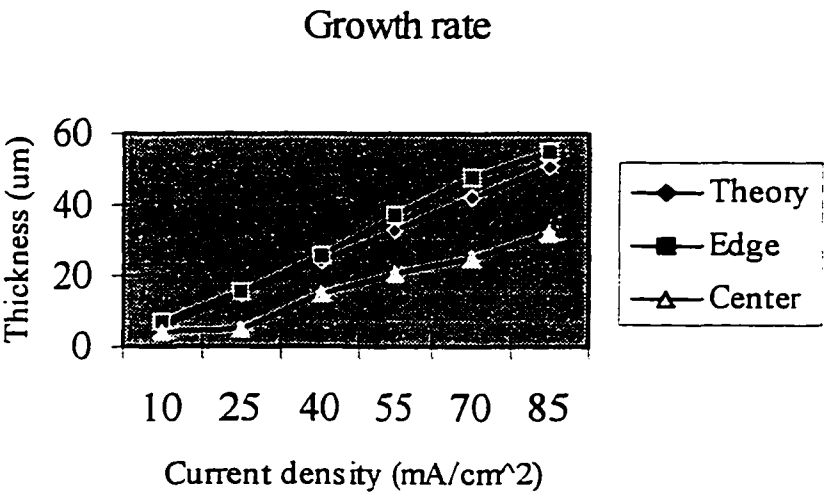

Figure 52. Nickel electroforming growth rate based on the current density for plating 30 min.

6.7 Thickness Uniformity in Electroforming

Nonuniform thickness of electroformed objects was consistently observed. The highest growth rate is on the edges of the plating area which leads to overplating (mushrooming) of the boundaries as illustrated in Figure 53. The electrodeposit thickness ratio of the edge to the center location was more than two.

Figure 53. The nonuniform thickness after electroforming.

To enhance the thickness uniformity of electroforming, several parameters were changed. First, an attempt was made to improve the thickness uniformity by changing the anode geometry was tried. According to the electric field distribution, the same size anode and cathode should have a uniform distribution of plating current. However, the experimental results showed that anode geometry had no effect on the improvement of thickness uniformity. Second, the spacing between anode and cathode was investigated. Two electrodes were placed at 2, 4, 6, 8, and 10 cm, spacing to test the uniformity effect. No sample showed thickness uniformity improvement by variations of the electrode spacing. Third, different current waveforms were tried to improve thickness uniformity. The current waveforms used were pulse-DC, periodical (partial) reverse, periodical reverse, and DC. The experimental results showed that DC plating had the smallest thickness ratio of edge to center location of plating area. As all results showed the highest growth rate on the edges of the plating area, the thickness uniformity can be improved if it is possible to reduce the growth rate on edges.

The apparatus to improve the electroform uniformity is shown in Figure 54. A secondary cathode is added to the electroforming station. The secondary cathode is a frame shaped like the plating area and has a shape which will locally reduce the growth rate of the primary cathode. Figure 55 illustrates an electroformed nickel sample with its secondary cathode. No mushrooming existed on the boundaries of the sample even it was overplated, the thickness uniformity was improved as compared with Figure 53.

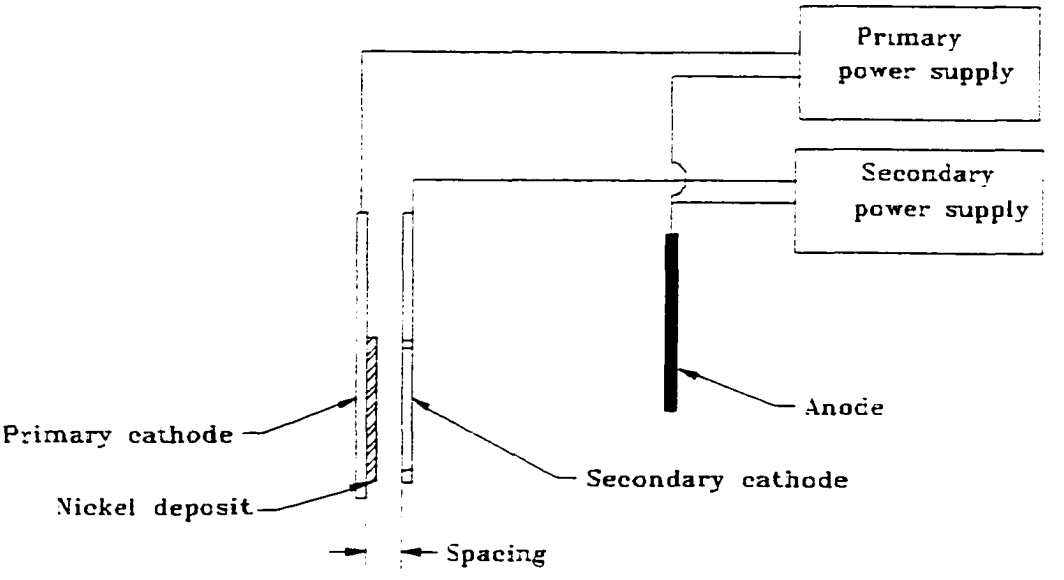

Figure 54. The apparatus for unifrom electroforming.

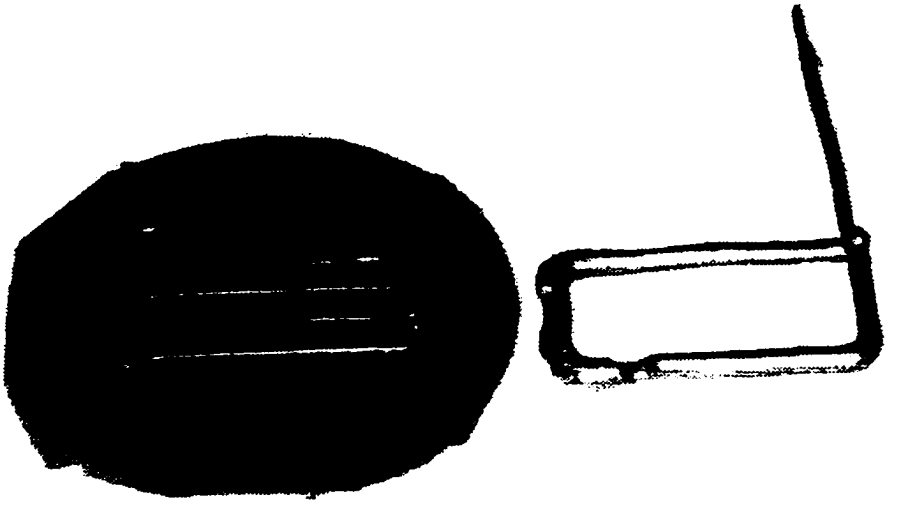

Figure 55. The electroformed nickel mold and its secondary plating cathode.

The secondary cathode is placed at a specific distance away from the primary cathode when electroforming. This spacing is limited to less than 2.5 mm; larger spacings will not have any effect. Two power supplies are used; one is for the primary electrodes

and another is for the secondary electrode. Both electroforming cathodes use the same anode. The current density for the secondary cathode is same as the primary electrode. The objective of the secondary electrode is to reduce local ion concentration of the "double layer" surface plating area, thus reducing the growth rate on the edges of the nickel deposit. The thickness ratio of edge to center of 500 μm sample decreased from 2.5 to 1.4. The thickness uniformity improvement is achieved without a loss in plating rate in the center of the features.

CHAPTER 7

SURFACE PLANARIZATION

7.1 Prelude

The fabrication of nickel structures is usually done by overplating the PMMA resist molds and then is finished by mechanical treatment such as polishing. The surface non-uniformity can be higher than 1.5 mm on the edges of the sample when plating a 1 mm thick PMMA mold if the secondary cathode is used. If the secondary cathode is not used, the thickness on the edges of the sample can be higher than 2 or 3 mm.

Uniform thickness and surface smoothness are required for the final products. The polishing process used different grit sizes of sandpaper and crocus cloth to get a surface roughness less than Ra 0.2 μm for an electrodeposited nickel surface.

7.2 Polishing Procedure

The metallurgical polishing machine is shown in Figure 56. The polishing machine has a rotating disk with two control speeds: 800 and 2000 RPM. The sandpaper or crocus cloth is fixed on the polishing disk. The substrate with nickel and resist structure is held by a vacuum chuck as shown in Figure 57. There is a filter to collect grit from entering the vacuum pump. The vacuum chuck holding the substrate faces the rotating polishing disk.

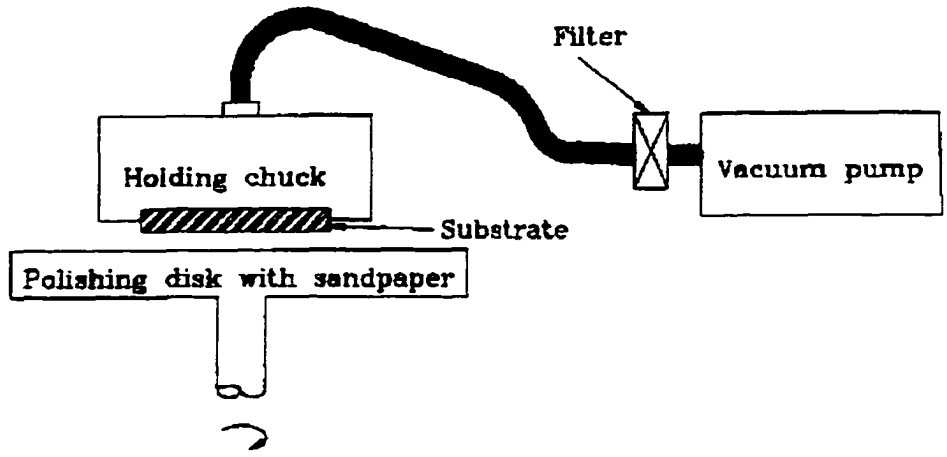

Figure 56. Layout of the polishing apparatus.

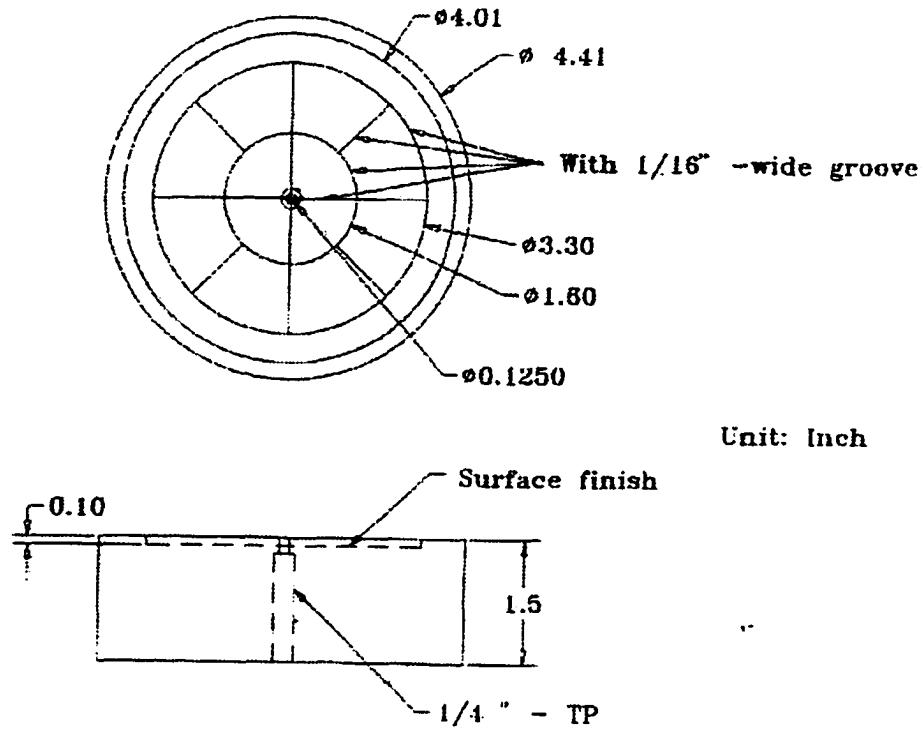

Figure 57. Schematic of the vacuum chuck design.

A flowchart to describe the polishing procedure is illustrated in Figure 58. 400 grit sandpaper was first used to remove uneven portion of electroformed nickel in a dry polish step. Wet polishing resulted in rapid breaking of the 400 grit sandpapers. The removal rate is about 50 μm/min with 400 grit sandpaper at 2000 RPM. When the uneven portion is removed, smaller grit sandpaper was used to remove overplated portion. The second polishing stage was done with wet 600 grit sandpaper at 2000 RPM. 600 grit sandpaper is water resistant and did not break in wet polishing. The polishing rate was about 6 μm/min. A sheet of 600 grit sandpaper wears within 5 minutes when polishing nickel deposit. The second polishing stage was stopped when the boundary of the nickel and the PMMA appeared as in Figure 59. The irregular shape is due to the overplated nickel still remaining on the resist post. The resist post should be a circle after complete planarization as shown in Figure 60. The final polish used crocus cloth and polishing compound to finish the surface roughness less than Ra 0.2 μm.

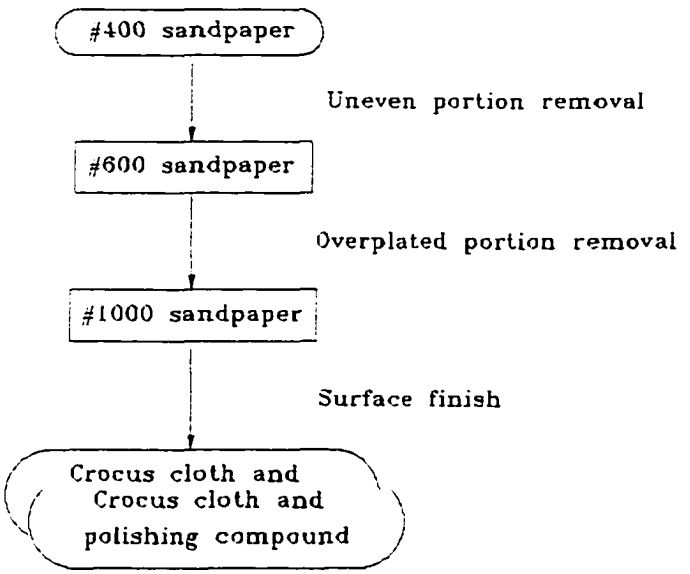

Figure 58. A flowchart of the polishing procedure.

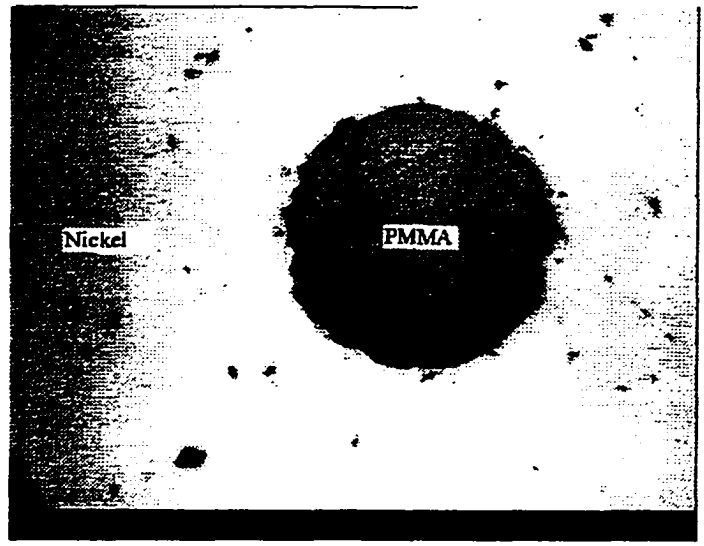

Figure 59. Incomplete planarization resulting in irregular edges.

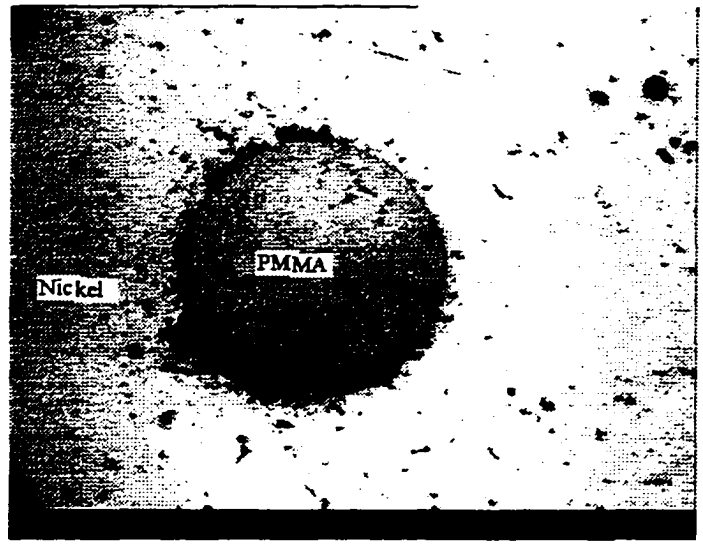

Figure 60. Complete planarization resulting in a circle between nickel and PMMA.

7.3 Polishing Results

The surface roughness of the nickel deposit after the final polish is like a mirror face. The local surface roughness in a 116 x 156 μm region is about Ra=0.02 μm as measured by the RST system. Some scratches are caused by the crocus cloth during

the polishing process, and the roughness of these scratches are less than Rt=0.2 μm as shown in Figure 61. A line across from the top left to lower right is a very shallow scratch which will not effect the optical fiber ferrule structure.

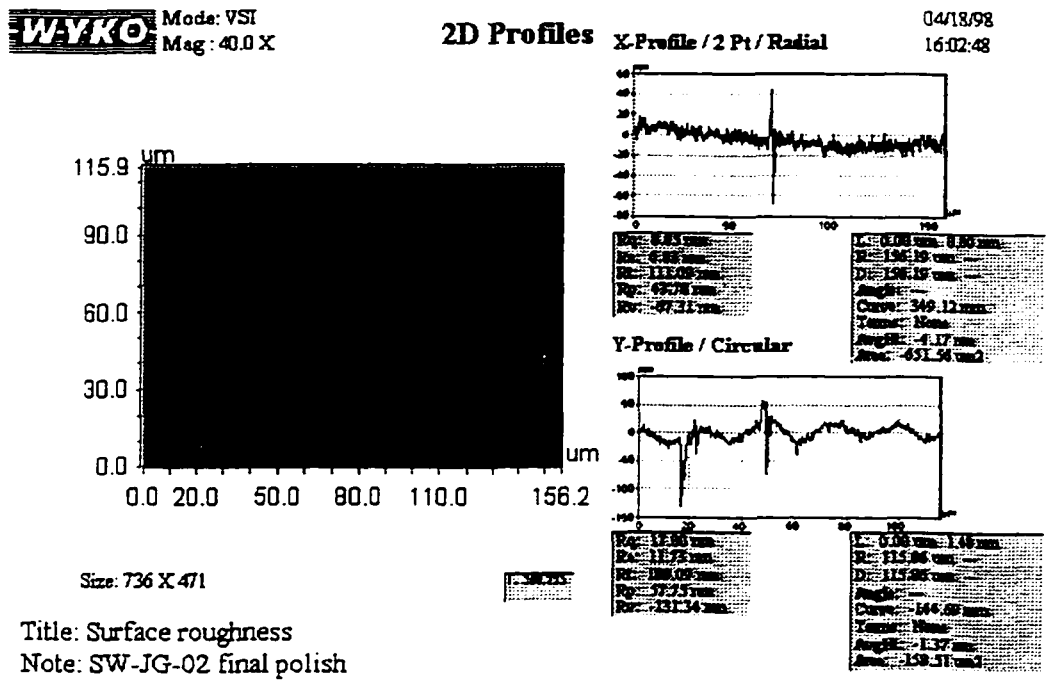

Figure 61. The roughness measurement of a scratch over the nickel deposit surface.

7.4 Flatness Measurements

PMMA is a soft material, compared with nickel. Since two adjacent materials were polished by the same mechanism, the flatness after polishing must be investigated. The interface flatness between nickel and PMMA after polishing measured by the RST system is shown in Figure 62. The rectangular box is the nickel deposit and outside area is the PMMA mold. The flatness difference between nickel and PMMA at a 160 x 118 μm region is about 1 um after polished. It shows that PMMA wears faster than nickel at the adjacent region during the polishing work.

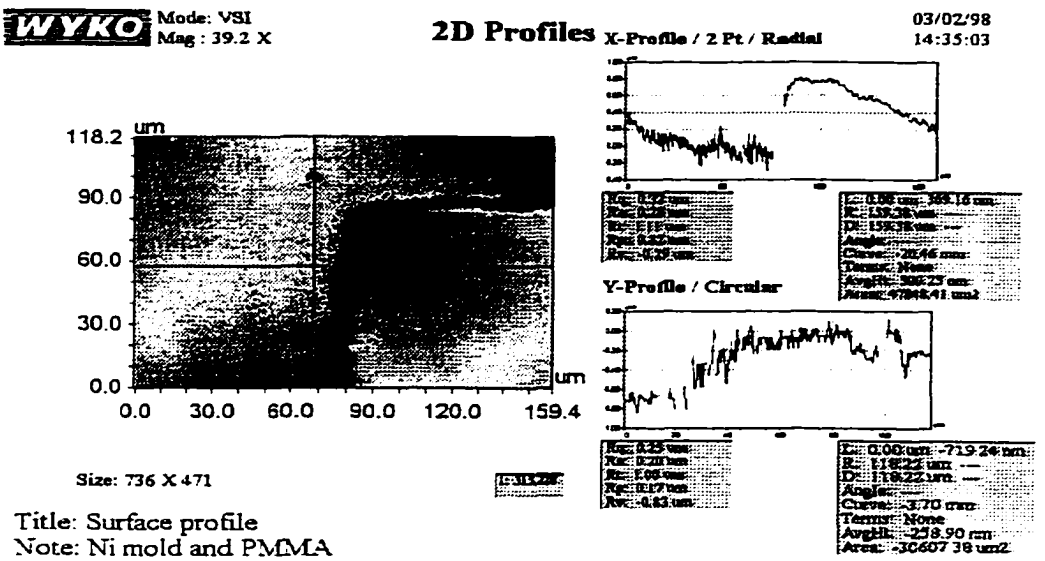

Figure 62. The surface profile between the nickel deposit and the PMMA mold.

The surface flatness horizontally across an optical fiber ferrule measured by the Tencor surface profiler is shown in Figure 63. The thickness variation is less than 20 μm across a 3.4 mm width, as indicated between two vertical lines. The apex of the thickness is located about in the middle of the pattern.

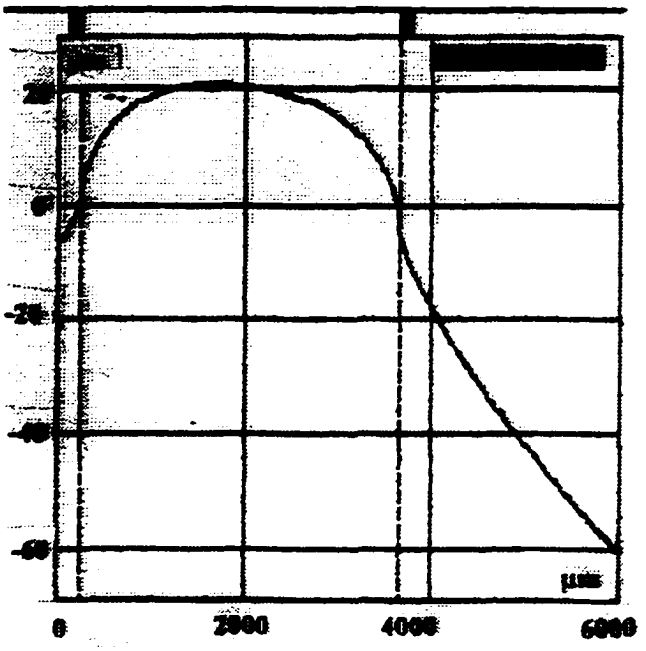

Figure 63. The surface flatness of a ferrule structure obtained from the Tencore surface profiler.

There is about a 100 μm thickness difference between the PMMA and the nickel structure after polishing as shown in Figure 63. The vertical axis is a 10 μm scale, and the horizontal axis is a 1 μm scale with 6000 μm long. This long range in flatness measurement is different from the RST measurement which covers only a small region. Figure 64 provides a good view on the overall surface profile after polishing.

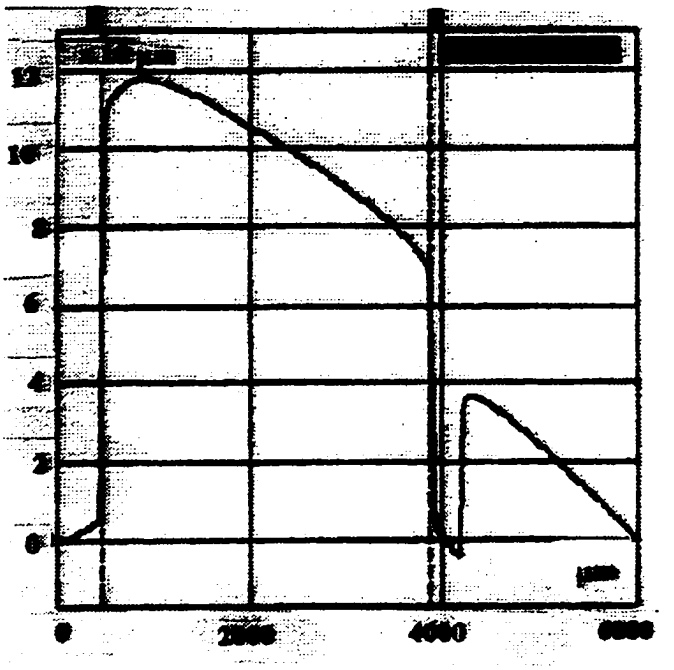

Figure 64. Thickness difference between PMMA and nickel structures after polishing.

7.5 Thickness Measurements

A linear variable differential transducer (LVDT) was used to measure the thickness of the nickel structure as shown in Figure 65. The LVDT has a resolution of 0.1 μm and measuring accuracy +/- 10 μm. The probe of the LVDT directly contacts on nickel surface to measure heights. The probe was held by a pneumatic control (air pressure is less than 20 psi) to be flexible and sensitive to the vertical displacement. The measuring sample was placed on a flat granite table; LVDT readings of the flatness variation were +/- 5 μm over a 10 cm length of the table.

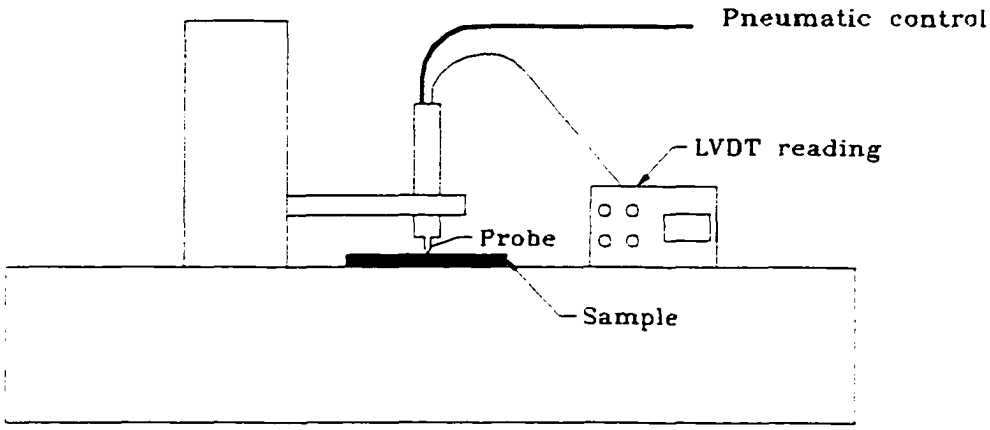

Figure 65. The LVDT setting for flatness measurements.

Nickel structures were measured by the LVDT after polishing. Table 10 shows the thickness results. Maximum thickness variation is the difference between the highest to the lowest location. To sum up, a single optical fiber ferrule nickel structure can be polished to 15% flatness by the polishing procedure used in this study.

Table 10. The results of thickness measurements by LVDT.

Sample	Maximum thickness variation (μm)	A single ferrule variation (μm)	A single ferrule variation ratio (%)
SI-WY-001 (150 μm)	25	17	11.3
SW-JG-002 (300 μm)	50	50	16.6
SI-WY-007 (500 μm)	80	60	12

CHAPTER 8

METROLOGY

8.1 The Optical Imaging System

8.1.1 Apparatus settings

Critical dimensions of the fiber ferrule molds are pitch distance and channel diameter. The Optical Imaging System (Optimas), is used to measure channels diameter and pitch distance. Figure 66 is an illustration to describe the setup of the Optical System.

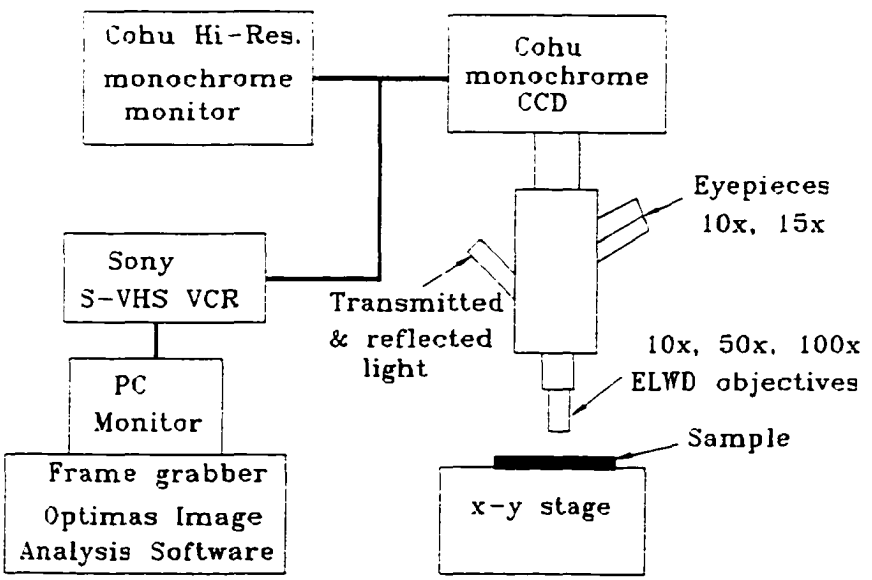

Figure 66. The setup of the IfM Optical Imaging System.

The Optimas consists of a Nikon Optiphoto microscope, a Cohu monochrome CCD camera, a monochrome monitor, a PC, an Oculus TCX frame grabber, and Optimas

5.1 Image Analysis Software. The optical image from the microscope is picked up by the CCD camera; then it is fed into the monochrome monitor, VCR as well as the frame grabber. The frame grabber digitizes the image, and it is displayed on the PC monitor. The digitized live image can be viewed either using the software for the frame grabber or the Image Analysis Software (Optimas).

8.1.2 Calibration

The prototype SRM 2090 scanning electron microscope magnification calibration standard from National Institute of Standards and Technology (NIST) was used to calibrate the Optimas. The SRM 2090 is an electron beam written and lithographically produced sample. It can be used to calibrate objects from 3 mm to 0.2 μm. The Optimas was calibrated by the pitch 100 μm for D50X objective lens as shown in Figure 67. The accuracy is about +/- 0.5 μm after 5 times calibrations.

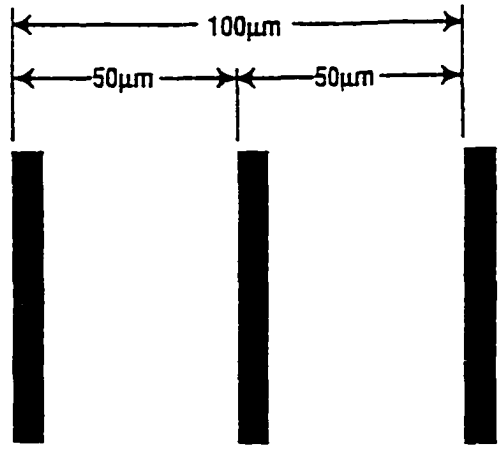

Figure 67. The measuring method for calibration.

The illuminated light intensity affects the measurement result of the Optimas as illustrated in Figure 68 and 69. The experiment used the MCNC Cr mask as a measuring

object. A designed size (126 μm) was used to calibrate the light intensity. Figure 68 is the result of measurements on a hole (nominal 126 μm in diameter) of the Cr mask at different light intensity. Figure 69 is the result of measurement on a Cr absorber (nominal 126 μm in diameter) of the Cr mask.

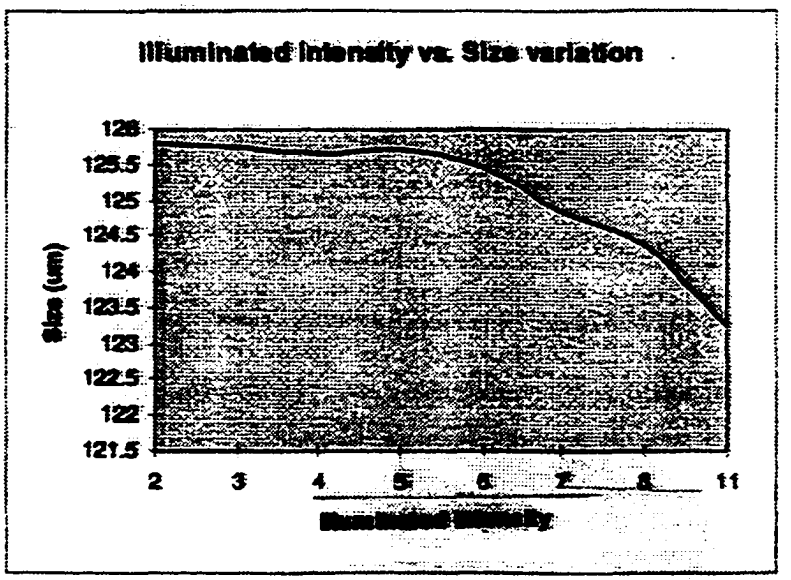

Figure 68. The measurement of a hole diameter as a function of illumination intensity.

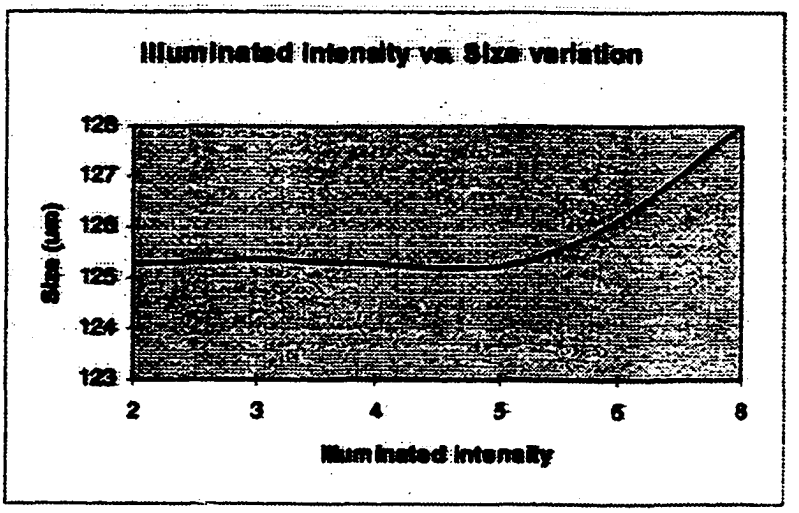

Figure 69. The measurement of a Cr absorber as a function of illumination intensity.

All measurements are assumed at the right focus depth. Both figures shows that high light intensity resulted in strong backscattering from the Cr surface. This backscattering caused an interference on the edges of the hole and the Cr absorber. High intensity shrunk the image of the hole and expanded the image of the Cr absorber. From both figures, the reliable light intensity is between scale 1 to 5. In practice, the light intensity should be as low as possible to minimize the backscattering effect on the dimensional measurement.

8.2 Measuring Procedures

Dimensional measurement in this project include hole diameter and pitch distances for the optical fiber ferrule. Measurement included the masks, the resist molds, and the nickel structures. This series of measurements is needed to determine the dimensional bias in the manufacturing process. There are 192 holes in Field 2 of the working mask. The first step is to denote each hole before starting measurements. Figure 70 is the indication of each hole in Field 2 of the working mask. Letters from A to J represent 10 patterns on the working mask Number from 1 to 12 represent left to right on each pattern.

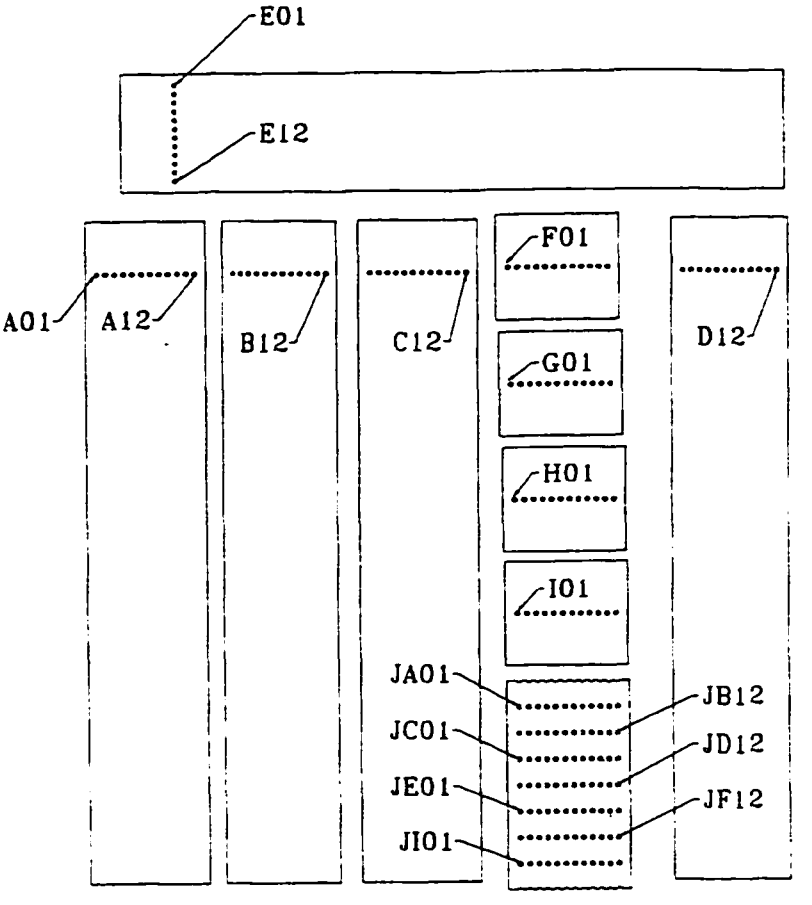

Figure 70. The indication of each hole in Field 2 on the working mask.

The second step of the measuring procedure is to determine the measuring method for hole diameter. There are many selections for diameter calculations in the Optimas routines. The two methods chosen were determination of the major axis from points on the circumference and diameters determined from point to point on the circumference across the center of the hole. These deteminations were based on the consideration to insert optical fibers (the inside diameter of channels is the most critical for insertion). The major axis diameter method can be used only for good contrast images as illustrated in

Figure 71. The frame profile can be autotracked to calculate the hole diameter from the Optimas routines, and it is more accurate than a visual determination of the point-to-point diameter. Visual determination of the point-to-point diameter may have one pixel variation, which is a +/- 0.47 μm error.

Figure 71. Clear contrast for hole measurement on a tungsten mask (25 μm thick).

Optical microscopy-related instruments have also been used to measure the diameters, but they have natural limitations of resolution approximately equal to 0.6 μm. The accuracy of the Optimas system at 25x objective lens is limited to 0.5 μm due to pixel size (0.47μm per pixel).

Pitch distance between the holes can be measured by the following method: the center coordinate and diameter of the channel can be calculated according to the circle

equation (Equation (8.1)). Pitch distance is then calculated by the distance of the center coordinates of two channels as shown in Equation (8.2).

$$(x-a)^2+(y-b)^2=r^2 \tag{8.1}$$

Where (x,y) is the x and y coordinate of a point on the circumference, (a, b) is the x and y coordinate of the center of the hole, and r is the radius.

$$Pd=\sqrt{(x_2-x_1)^2+(y_2-y_1)^2} \tag{8.2}$$

Where Pd is the pitch distance, (x_1,y_1) are the center coordinate of hole 1, and (x_2,y_2) are the center coordinate of hole 2.

8.3 Results

8.3.1 Hole diameter measurements

Hole diameter accuracy of the optical fiber ferrule in the fabrication process from Cr mask to Ni structure were measured within 0.5 μm. Table 11 lists the results for design size 126 μm diameter and the standard deviation. Each value represents the mean of 10 samples, i.e., 10 measurements on each sample.

Table 11. Measurement data to determine dimensional bias of hole diameters, 126 μm sample.

Sample	Measurement	Standard deviation	Difference
Cr mask	126.01	.25	0.01
PMMA	126.26	.08	0.26
Ni structure	126.25	.15	0.25

8.3.2 Pitch distance measurements

Pitch distance measurement from Cr mask to Ni structure from a nominal design pattern (Pd = 251 μm) is listed in Table 12. Each value represents the mean of 11 pitch distances on a designed pattern, i.e., 3 measurements on each pitch distance. The Optimas's resolution at 10X objective lens is 0.98 μm per pixel. This standard means that the measuring accuracy of the pitch distance is limited to 1 μm. Therefore, the pitch distance measurement to meet the stringent specification (+/- 0.25 μm) for the optical fiber ferrule mold is within the uncertainty by the Optimas method.

Table 12. Measurement data on pitch distances of a nominal designed pattern with pitch distance 251 μm.

Sample	Measurement	Standard deviation	Difference
Cr mask	250.57	0.59	0.57
PMMA	251.25	0.92	0.25
Ni structure	250.93	0.89	0.93

8.3.4 Channel divergence measurements

A test sample (300 μm thick) with semicircles in nickel (pattern J) and standard design pattern (pattern E) were used to measure the divergence of channels. The results of divergence measurement on different channels are listed in Table 13. Measured lengths were determined by point to point of edges on the channel in the measurement of pattern J. Measurements were performed at the top and bottom of the test sample (pattern J) from side view. The measuring method on pattern E was same as hole measurements by using points on the circumference at the top and bottom of holes. The divergence is

determined by the dimension difference between the top and bottom. Each value represents the means of 5 measurements.

Table 13. Divergence measurements on a test sample (300 μm thick).

Samples	Top	Standard deviation	Bottom	Standard deviation	Divergence (μm)
Channel J01	128.41	0.23	128.78	0.19	+ 0.37
Channel J02	133.04	0.26	133.56	0.33	+0.52
Hole E01	126.21	0.48	126.59	0.54	+0.38
Hole E12	125.96	0.42	126.39	0.47	+0.43

CHAPTER 9

CONCLUSIONS AND RECOMMENDATIONS

9.1 Conclusions

The fabrication process of optical fiber ferrules in nickel material for insert with twelve channels was established in this study. The optical fiber ferrule mold with 500 μm thickness electroplated nickel was fabricated with the required accuracy in the hole diameters. Three mask-making methods were used to make deep X-ray masks to expose optical fiber ferrule patterns. Mechanically machined mask-making provides a direct and fast way to complete a mask, but it cannot achieve the specifications of the optical fiber ferrule. Micro-EDM mask-making has the potential to achieve the dimensional accuracy required for deep X-ray masks. The E-beam written mask was successful to realize the requirement of dimensional accuracy for optical fiber ferrules. The dimensional accuracy requirements of channel diameters for optical fiber ferrules were satisfied, the required tolerance was within 0.5 μm.

The deep X-ray mask made by using the E-beam written method was exposed to synchrotron radiation with energy 1.3 GeV in Baton Rouge. The developing process was performed at the IfM. A modified developing procedure from the standard procedure of other researchers was used to prevent losing resist posts from the substrate.

A nickel electroforming station to deposit nickel structures into resist molds is established at the IfM. To improve the deposit thickness uniformity, a secondary plating electrode was added. The results showed that the thickness ratio of edge to center on a plating area has been decreased from 2.5 to 1.4, proving that it is feasible to reduce local growth rate on edges of plating samples.

9.2 Recommendation for Further Research

Two directions are recommended for further research: one is the fundamental analysis of the LIGA micromanufacturing process, and the other is the invention of industrial products using similar techniques.

The fundamental analysis of micromaufacturing process includes mask fabrication, deep X-ray lithography exposure, resist development after exposure, nickel electroforming, structure planarization, and metrology. Three mask fabrication methods were illustrated in this project. Although only the E-beam writing method achieved the requirements of the project sponsor, the other two methods may be applied to other applications. They may not have the high accuracy that E-beam writing has, but their simple working process and economy can bring convenience and low cost to the manufacturing process when dimensional requirements are not as stringent as the Siecor project.

Deep X-ray lithography exposure has the goal to achieve thicker structures in the future. Energy limitation was one of the reasons we were unable to expose 1 mm thick PMMA. New research projects may need structures greater than 1 mm thick as products. High energy of deep X-ray lithography is needed to expose thicker structures.

After exposure, development is a critical step in the success of the overall process. Since there was a problem in keeping resist posts on the substrate in this work, the essentials of development should be studied in new projects, especially in high aspect ratio structures with isolated resist features.

A conductive layer for the substrate is necessary for the electroforming process. This layer is associated with the resist bonding and the resist adhesion after development. The conductive materials used in this project were Cr, Au, and Cu. Three materials were layered, Cr was at the bottom, Au was in the middle, and Cu was at the top. Their thicknesses related to the bonding were not studied. This effort also needs further study.

The nickel electroforming process can be said to be successful for depositing nickel structures. Nickel electroforming does not effect dimensional accuracy in manufacturing process. The properties of deposited nickel for microstructures should be a subject for study. The relationship between growth rate and the properties of deposited nickel can also be further studied. A series of test patterns for the properties of deposited nickel have been designed on the working mask (Field 2). A study of electroformed nickel properties will help the fundamentals of this micromanufacturing process. This study will be useful to design microstructures with the required mechanical properties, such as Young's modulus, hardness, and tensile strength.

The technique to improve thickness uniformity of nickel electroforming was introduced in this project. However, better methods for planarization and surface finish are still needed to improve the product quality. The vacuum chuck to hold the substrate was controlled manually, a system was not consistent with precise control. The chuck can

be improved by mounting on it a mechanical fixture with a good feed control, which will improve the surface flatness and finish.

This study was limited by insufficient measuring instruments. The high accuracy requirement of measuring channel diameter with 0.5 μm tolerance could just be achieved by optical microscopy. A similar difficulty also existed in measuring the pitch distance between two channels and in this case we do not have sufficient resolution with measuring device. Either a direct contact measuring instrument or image measuring instruments have to be explored to achieve high resolution (at least 0.1 μm) and accuracy in submicron range.

The LIGA process used in this study provided high-accuracy product replication from the mask, and the possibility of mass production in industrial products exists. A successful manufacturing process to realize the products from invention is needed. The fabrication of optical fiber ferrules in nickel is the first realization of product from the LIGA process at the IfM.

APPENDIX I

SIMULATION OF EXPOSURES

APPENDIX - I THE SIMULATION OF EXPOSURE PARAMETERS FOR 500 μM THICK PMMA.

Ei(400pts)	P(Ei) [watt/ev]	Lables	Fi
100	0.0003	SI-WY-004	7.5E-120
140.10	0.00040		0
180.20	0.00042		0
16059.8	1.44958E-07		0.997006
16100	1.41796E-07		0.99703

Input Parameters		Input Parameters	
Beam E (GeV)	1.3	Type : Mirror/Filter	Filter
Radius (m)	2.928	Element's Material	BE
Current (A)	0.1	Density (g/cm^3)	1.845
Haccept (mrad)	1	Angle(deg)/Thickness(microns)	200
Emin	100	Input column	2
Emax	16100	Mirror's roughness	
num of points	400	needs updating	YES

Source Characteristics		Integrals and Averages	
Critical wave length (A)	7.44	Average Energy	
Critical Energy (eV)	1664.61	Peak Energy	
Power/amp (Kwatts/amp)	86.32	Median Energy	
Total Power (Kwatts)	8.63	Standard deviation	
Total Power/mrad (watts/mrad)	1.37	1.5% Energy	
Power accepted (watts)	1.37	98.5% Energy	

Iout	Fi	Iout	Fi	Iout	Iout	Fi	
2.8E-123		2.3E-128		6.4E-251	3.03E-260	2E-260	0
0		3.7E-127		0	4.31E-22	0	0	1.8401E-275
0		1.08E-95		0	1.38E-18	0	0	4.9392E-159
1.45E-07		0.983918		1.42E-07	0.996386	1.42E-07	1.42E-07	0.97776124 6
1.41E-07		0.984039		1.39E-07	0.996413	1.39E-07	1.39E-07	0.97793729 5

	Filter Al	Filter Si	Filter c5 h8 o2
	2.73	2.32	1.18
	10	2	300
	5	7	9
	YES	YES	YES

Iout	D_top	D_bottom
0	8.6E-256	0
0	0	0
0	0	0
1.39E-07	1.06E-07	1.04E-07
1.36E-07	1.03E-07	1.01E-07

Input Parameters	
dose(J/cm^3)	4000
Scan (cm)	1
Top surface mA-min	1564.236
Bottom surface mA-min	5849.652
Ratio of bottom to top mA-min	3.73

APPENDIX II

HOLE DIAMETER MEASUREMENTS

APPENDIX IIA - HOLE DIAMETERS OF SAMPLE SI-WY-01 (150 μM THICK NI STRUCTURES). EACH INDICATION OF HOLES IS SHOWN IN CHAPTER 8. THE MEASURING METHOD FOR HOLE DIAMETERS OF NICKEL STRUCUTRES WAS THE LENGTH OF POINT-TO-POINT ON THE CIRCUMFERENCE OF THE HOLE.

Hole	mean	stdev	Hole	mean	stdev
A01	126.9	0.39	JA01	128.37	0.24
A06	126.8	0.37	JA06	127.87	0.63
A12	126.79	0.65	JA12	127.51	0.8
mean	126.83		mean	127.917	
Design	126		Design	127.5	
Diff	0.83		Diff	0.41667	
B01	126.82	0.69	JB01	127.55	0.22
B06	126.2	0.78	JB06	127.4	0.51
B12	126.62	0.66	JB12	127.04	0.73
mean	126.547		mean	127.33	
Design	126.5		Design	127	
Diff	0.04667		Diff	0.33	
C01	125.34	0.83	JC01	127.07	0.34
C06	125.88	0.73	JC06	127.05	0.62
C12	125.21	0.53	JC12	126.63	0.59
mean	125.477		mean	126.917	
Design	125.5		Design	126.5	
Diff	-0.0233		Diff	0.41667	
D01	126.84		JD01	125.88	0.43
D06	126.64		JD06	125.93	0.41
D12	124.24		JD12	125.9	0.9
mean	125.907		mean	125.903	
Design	126		Design	125.5	
Diff	-0.0933		Diff	0.40333	

Hole	mean	stdev
E01	126.77	
E06	127.3	
E12	126.25	
mean	126.773	
Design	126	
Diff	0.77333	
F01	127.75	0.43
F06	127.74	0.59
F12	127.24	0.89
mean	127.577	
Design	127	
Diff	0.57667	
G01	125.3	0.33
G06	125.1	0.32
G12	125.6	0.21
mean	125.333	
Design	125	
Diff	0.33333	
H01	126.13	0.53
H06	125.97	1.07
H12	126.28	0.57
mean	126.127	
Design	126	
Diff	0.12667	
I01	126.55	0.58
I06	126.78	0.76
I12	126.09	0.68
mean	126.473	
Design	126	
Diff	0.47333	

Hole	mean	stdev
JE01	125.45	0.53
JE06	125.79	0.62
JE12	124.43	0.81
mean	125.223	
Design	125	
Diff	0.22333	
JF01	124.96	0.52
JF06	124.97	0.6
JF12	124.21	0.63
mean	124.713	
Design	124.5	
Diff	0.21333	
JI01	123.97	0.56
JI06	124.21	0.49
JI12	123.45	0.99
mean	123.877	
Design	124	
Diff	-0.1233	

APPENDIX IIB - HOLE DIAMETERS OF SAMPLE SW-JG-02 (300 μM THICK NI STRUCTURES). EACH INDICATION OF HOLES IS SHOWN IN CHAPTER 8. THE MEASURING METHOD FOR HOLE DIAMETERS OF NICKEL STRUCUTRES WAS THE LENGTH OF POINT-TO-POINT ON THE CIRCUMFERENCE OF THE HOLE.

Hole	mean	stdev	Hole	mean	stdev
A01	126.55	0.15	F01	127.43	0.56
A06	126.34	0.54	F06	128.05	0.23
A12	126.92	0.33	F12	127.57	0.41
mean	126.603		mean	127.683	
Design	126		Design	127	
Diff	0.60333		Diff	0.68333	
B01	127.14	0.65	G01	125.35	0.35
B06	127.17	0.48	G06	125.54	0.36
B12	127.75	0.46	G12	125.12	0.33
mean	127.353		mean	125.337	
Design	126.5		Design	125	
Diff	0.85333		Diff	0.33667	
C01	126.14	0.46	H01	125.84	0.48
C06	126.2	0.5	H06	126.43	0.58
C12	125.68	0.37	H12	125.9	0.76
mean	126.007		mean	126.057	
Design	125.5		Design	126	
Diff	0.50667		Diff	0.05667	
D01	125.85	0.45	E01	127.13	0.77
D06	126.6	0.56	E06	126.81	0.48
D12	126.32	0.58	E12	126.58	0.49
mean	126.257		mean	126.84	
Design	126		Design	126	
Diff	0.25667		Diff	0.84	

APPENDIX IIC - HOLE DIAMETERS OF SAMPLE SI-WY-07 (500 μM THICK NI STRUCTURES). EACH INDICATION OF HOLES IS SHOWN IN CHAPTER 8. THE MEASURING METHOD FOR HOLE DIAMETERS OF NICKEL STRUCUTRES WAS THE LENGTH OF POINT-TO-POINT ON THE CIRCUMFERENCE OF THE HOLE.

Hole	mean	stdev	Hole	mean	stdev
A04	126.9	0.48	E01	126	0.5
A06	126.8	0.37	E06	126.68	0.71
A12	126.42	0.44	E12	126.52	0.58
mean	126.707		mean	126.4	
Design	126		Design	126	
Diff	0.70667		Diff	0.4	
B04	126.53	0.49			
B06	126.8	0.51			
B08	126.61	0.57			
mean	126.647				
Design	126.5				
Diff	0.14667				
C02	125.97	0.61			
C03	125.29	0.5			
mean	125.63				
Design	125.5				
Diff	0.13				
D01	126.39	0.32			
D06	126.06	0.55			
D12	126.01	0.2			
mean	126.153				
Design	126				
Diff	0.15333				

NOMENCLATURE

A	Atomic weight
a	Plating area
C	Ion concentration
Cb	Metal concentration at the bulk solution
Cs	Metal ion concentration at the electrode surface
D	Diffusivity constant
F	Faraday constant
j	Electrical current
K	Electrochemical equivalent
M	Mass of electrodeposited metal
n	Index of refraction
R	Radius of the circle
t	Plating thickness
u	Ion mobility
z	Ionic charge

Greek Letters

Ω	Electrical resistance
η	Electroforming growth rate
λc	Characteristic wavelength

θ Angel of the arc

ρ Metal density

σ Conductivity of electrolyte

Θ Area current density

BIBLIOGRAPHY

1. Speippel, R.G. Fiber Optics, Reston Publishing Company Inc., Reston, Virginia, 1983, pp. 44-49.

2. Unger, S., & Nelson, J.C.C., Fiber Optics, Chapter 1, John Wiley & Sons, New York, 1990.

3. Becker, E. W., Ehrfeld, W., Hagmann, P., Maner, A., and Muenchmeyer, D., "Fabrication of Microstructures with high aspect ratio and great structural heights by synchrotron radiation lithography, galvanoforming, and plastic moulding (LIGA processes)," Microelectronic Engineering, vol. 4, pp. 35-56, 1986.

4. Guckel, H., Skrobis, K.J., Christenson, T.R., Klein, J., Han, S., Choi, B., Lovell, E.G., "Fabrication of Assembled Micromechanical Components via Deep X-ray Lithography," IEEE MEMS 91 Workshop, pp. 74-79, Japan, 1991.

5. Burbaum, C., Mohr, J., and Bley, P., "Fabrication of Capacitive Acceleration Sensors by the LIGA Technique," Sensors and Actuators A, 25-27, PP.559-563, 1991.

6. Schomburg, W.K., Baving, H.J., Bley, P., "Ti- and Be- X-ray Masks with Alignment Windows for the LIGA Process," Microelectronic Engineering, vol. 13, pp.323-326, 1991.

7. Lochel, B., Schliwinski, H.J., Huber, H.L., Trube, J., Schafer, L., Klages, C.P., Lithje, H., "Diamond Membranes for X-ray Masks," Micocircuit Engineering, Sept. 17-19, 1991.

8. Lochel, B., Chlebek, J.,Grimm, J., Huber, H.L., and Maciobek, A.M., "Silicon Membrane Mask Blanks for X-ray and Ion Projection Lithography," Japanese Journal of Applied Physics, vol.29, no.11, Nov., pp.2605-2609, 1990.

9. Guckel, H., Burns, D.W., Christenson, T.R., Tilmans, H.A.C., "Polysilicon X-ray Masks," Microelectronic Engineering, vol.9, pp.159-161, 1989.

10. Visser, C.C.G., Uglow, J.E., Burns, D.W., Wells, G., Redaelli, R., Cerrina, F., Guckel, H., "A New Silicon Nitride Mask Technology for Synchrotron Radiation X-ray Lithography: First Result," Microelectronic Engineering, vol.6, pp.299-304, 1987.

11. Ehrfeld, W., Glashauser, W., Munchmeyer, D.,Schelb, W., "Mask Making for Synchrotron Radiation Lithography," Microelectronic Engineering, vol.5, pp.463-470, 1986.

12. Pfeiffer, H.C., and Groves, T.R., "Progress in E-beam Mask Making for Optical and X-ray Lithography," Microelectronic Engineering, vol.13, pp.141-149, 1991.

13. Schmidt, M., Feiertag, H., Lehr, H., and Schmidt, A., "Mask Technology: Requirement," Course LIGA Technique, IMM, Gmbh, Mainz, Germany, 1994.

14. Schenk, R., "X-Ray Resist and Developing Process," Course LIGA Technique, IMM, Gmbh, Mainz, Germany, 1994.

15. Graham, A.K., Electroplating Engineering Handbook, 3rd, ed., Van Norstrand Reinhold Company, New York, 1971.

16. Lowenheim, F.A., Modern Electroplating, 2nd., ed., Jphn Wiley & Sons, Inc., New York, 1963.

17. Menz, W., Bacher, M., Harmening, M., and Michel, A., "The LIGA Technique - A Novel Concept for Microstructures and the Combination with Si-Technologies by Injection Molding," Proceedings of the 1991 IEEE Micro Electro Mechanical Systems Conference, Nara, Japan, Jan. 1991, pp.69-73.

18. Choi, B., Lovell, E.G., Guckel, H. Christenson, T.R., Skrobris, K.J., Kang, J.W., "Development of Pressure Transducers Utilizing Deep X-ray Lithography," Proceedings of the 6th International Conference on Solid -State Sensors and Actuators, San Francisco, CA, 1991, PP.393-396.

19. Guckel, H., Skrobis, K.J., Christenson, T.R., Klein, J., Han, S., Choi, B., and Lovell, E.G., "Fabrication of Assembled Micromechanical Components Via Deep X-ray Lithography," Proceedings of the 1991 IEEE Micro Electro Mechanical Systems Conference.,, Nara, Japan, Jan. 1991, pp.74-79.

20. Di Bari, G.A., "Nickel Plating," Metal Finishing Guidebook and Directory Issue, vol.92, no1A, 1994, pp.249-251.

21. DeVries, W.R., Analysis of Material Removal Process, Springer-Verlag Publishing, 1991.

22. Weber, L., "Construction and Realization of a Fiber Ribbon Ferrule," LIGA technique, IMM Institute of Microtechnology, Gmbh, Mainz, Germany, 1994.

23. Nagasawa, S., Sankawa, I., Satake, T., & Kashima, N., "Small-Size Push-on Type Optical Fiber Connector," The Transactions of the IEICE, vol. E70. No. 5, May 1987.

24. Zetterer, T., "Mask Technology: Fabrication," UETP-MEMS: Training in Microsystems-LIGA Technique, IMM, GMBH, Mainz, Germany, 1994.

25 Groves, T.R. et al, "Electron Beam Lithography for Manufacture of X-ray Masks," IBM J. RES. DEVELOP. Vol. 37 no. 3 May 1993.

26. Masuzawa, T., Fujino, M., Kobayashi, K., and Suzuki, T., "Study on Micro-Hole Drilling by EDM - Automatic Electrode Forming with Tracelling wire-", Bull. Japan Soc. Of Prec. Engr., Vol. 20, no. 2, June, 1986.

27. Kalapakjian, Serope, Manufacturing Processes for Engineering Materials, pp. 614, Addison-Wesley Publishing Company, 1991.

28. Chen, S.T. Developement of Vertical Micro CNC Electrical Discharge Machining Center and Research of Micro 3D Parts Machining, Master thesis, National Yunlin Science & Technology University, Taiwan, June 1997.

29. Menz, W., Microsystem Technology for Engineers Intensive Course, Nuclear Research Center Karlsruhe Institute for Microstructure Technology, Germany, September, 1994.

30. Geottert, J. "Experimental Report on Fundamentals of Deep Etch X-ray Lithography," La Tech University, 1997.

31. Liu, H., Master Thesis, Prescott Library of Louisiana Tech Univeristy, August, 1997.

32. Sun, Tai-Ping, Wan, C.C., & Shy, Y.M., "Plating with Pulsed and Periodic-Reverse Current," Metal Finishing, May, 1979.

33. Atkins, P.W., Physical Chenistry, 4th ed., New York: Freeman, 1990.

34. Lowenheim, F.A., Modern Electroplating, 2nd., John Wiley & Sons, Inc., New York, 1963.

35. Brockris, J. O'M., and Drazie, D.M., Electro-Chemical Science, Taylor &Francis Ltd., London, 1972.

36. Graham, A.K., Electroplating Engineering Handbook, 3rd., Van Nostrand Reihold Co., New York., 1971.

37. Blum, W., and Hagaboom, G.B., Principles of Electroplating and Electroforming, McGraw-Hill Book Co., New York, 1949.

VITA

Hsiharng William Yang was born on December 17, 1967, in Chuanghua, Taiwan, Republic of China. In 1988, he graduated from National Yunlin Institute of Technology in Mechanical Manufacturing Engineering. After graduation, he had a two-year military service in the Military Police. He studied Mechanical Engineering at Louisiana Tech University from 1991 to 1993 for his B.S. degree. He continued his graduate school at Tech and gained his M.S. degree in 1995. In September 1995, he was admitted to the Doctor of Engineering degree program at IfM of Louisiana Tech University.

IMAGE EVALUATION TEST TARGET (QA-3)

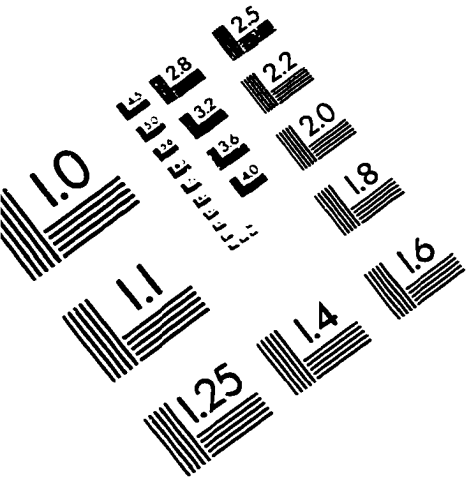

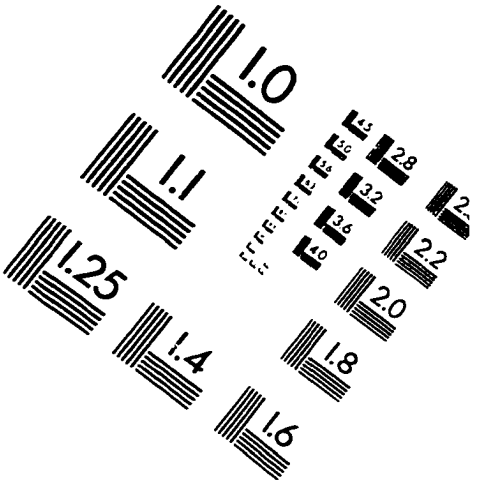

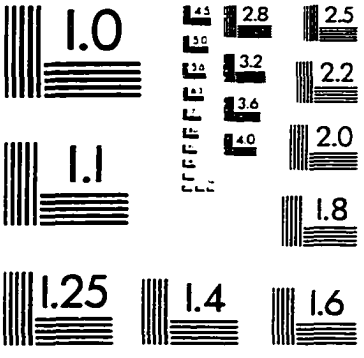

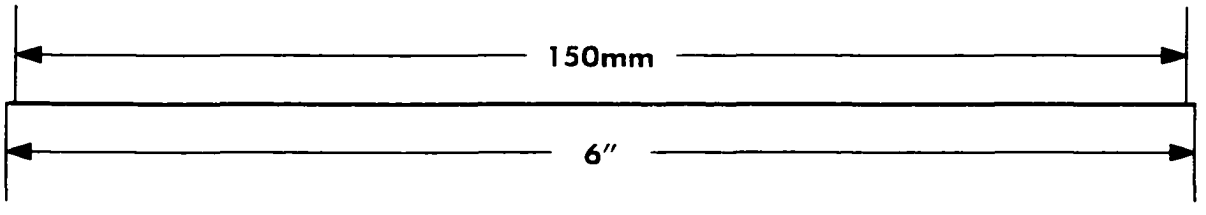

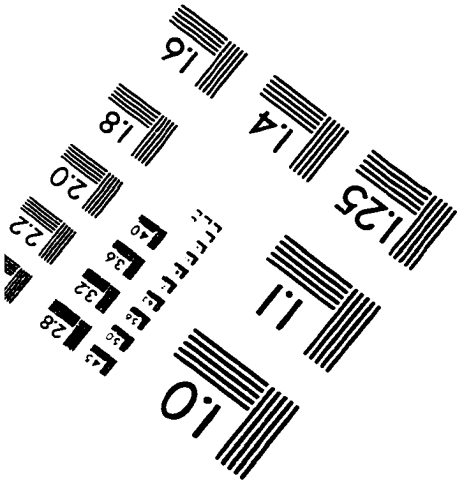

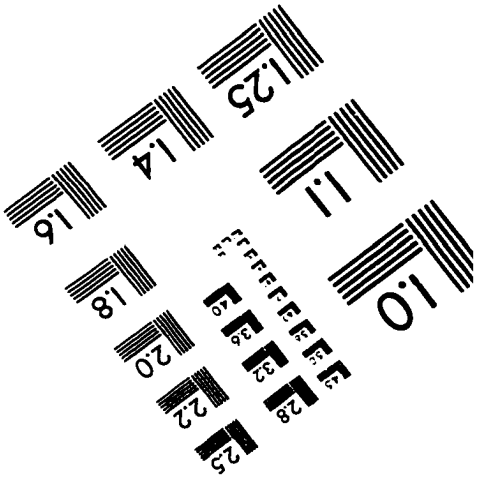

APPLIED IMAGE, Inc
1653 East Main Street
Rochester, NY 14609 USA
Phone: 716/482-0300
Fax: 716/288-5989